DOCTORAL THESIS DISSERTATION

Levitodynamics toward force nano-sensors in vacuum

Francesco Ricci

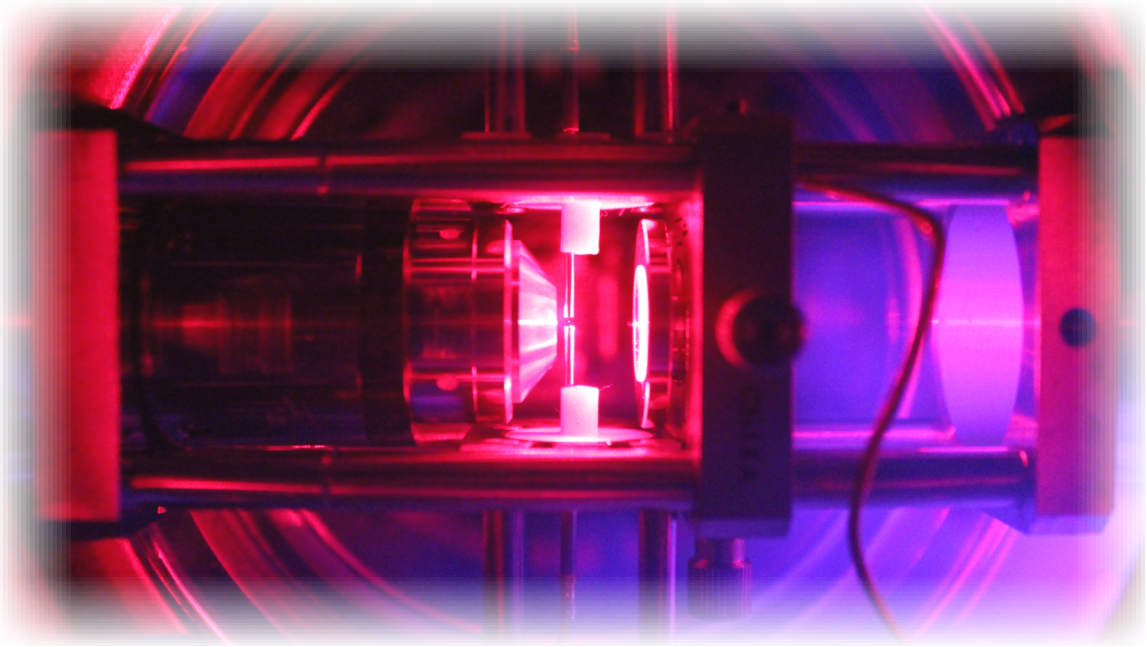

Advisor: Prof. Romain Quidant
Coadvisor: Dr. Raúl A. Rica

Barcelona, 2019

a Manolo

come promesso, "dedicherò a te ogni successo ed ogni sconfitta ..."

Abstract

Levitodynamics addresses the levitation and manipulation of micro- and nanoresonators with the purpose of studying their dynamics. This emerging field has attracted much attention over the last few years owing to unprecedented performances in terms of mechanical quality factors, cooling rates at room temperature, and ultra-high force sensitivities.
In this thesis, I establish the use of an optically levitated and electrically driven charged silica nanoparticle as a promising and reliable force sensor in vacuum.

The first two experiments discussed in this work seek a deeper knowledge and a higher control of the levitated system. Firstly, I suggest and demonstrate a novel protocol to measure the mass of the particle up to 2% accuracy using its electrically driven motion. This method improves by more than one order of magnitude the state-of-the-art mass measurements in standard optical tweezers schemes. Then, leveraging on these results, a second experiment is performed to address important open issues regarding the morphology of the nanoparticles used, with particular interest in their surface chemistry and in the understanding of mass-losses due to water desorption from the silica spheres. Finally, backed up by extensive theoretical background in nonlinear mechanical oscillators, I investigate the stochastic bistable dynamics of a parametrically driven nanoresonator in the nonlinear regime, discussing the potential of noise-activated stochastic switching and stochastic resonance as unconventional force detection schemes.

Contents

1 Introduction

1.1 Micro- and nano-mechanics

Understanding, controlling and manipulating matter at the nanoscale is probably a well suited definition of nanotechnology: a science that has undoubtedly revolutionized lives and economies of the modern world. Its conceptual origins date back to 1959, when Richard Feynman envisioned the potentiality of this field claiming: "*There's plenty of room at the bottom*" [27]. In fact, manipulating the building blocks of matter at the atomic and molecular scale has enabled groundbreaking technologies. From the very first nanotechnological device, namely the scanning tunnelling microscope [14], and passing by atomic force microscopy (AFM) [13] and nano-lithography, science has been able to fit more and more complex machines into ever smaller scales, an extraordinary example being today's computer processors. Nanoelectronics is indeed the science that probably most has benefited from the progress of nanotechnology, but certainly not the only one. Micro- and nano-electromechanical systems (MEMS and NEMS), for instance, are another example of technology that has widespread presence in everyday's life. Typically, they comprise a mechanical resonator that can be of the most diverse form: from ordinary AFM cantilevers and doubly clamped beams [83], to more complex fashions such as suspended trampolines [87], graphene membranes [113] and carbon nanotubes [74], just to name but a few. This family of systems serves a broad range of appli-

cations in both fundamental science and state-of-the-art technologies, one of their main functions being providing sensing operations, for examples in gyroscopes, accelerometers and pressure sensors, that can be easily integrated in any portable device.

Along the race for reaching better performances, significant achievements have been accomplished. Among others, extraordinary sensitivity to external forces [19], single electron spin detection [94], yoctogram mass sensitivity [17] and single-molecule spectroscopy [39] have been reported.

Furthermore their increasingly smaller sizes are nowadays providing a unique view in the exploration of the so called *mesoworld*, where new physics emerges beyond our classic understanding [83]. In fact, NEMS consist of too many atoms to be described by conventional quantum mechanics, and yet they are too small to completely neglect quantum effects. Therefore the arise of questions such as: can a mesoscopic object be put in a quantum superposition?, and how *big* should such a system be to observe the quantum-to-classical transition and what are the responsible effects?. Somehow, these are the very same questions that Erwin Schrödinger was asking himself in 1935 with his famous dead-or-alive cat *gedanken* experiment [96].

A positive answer to the first question was disclosed in 2010 by O'Connell and colleagues, who cryogenically refrigerated the mechanical mode of a drum resonator and were able to perform for the first time quantum-limited measurements at the single phonon level [79] on a macroscopic system. The door to the quantum mesoworld was finally open. Since then, several other groups have been able to access the quantum ground state of mechanical motion [106] This was also possible thanks to the development of ultra-sensitive optical techniques that, backing up NEMS, initiated a novel branch of nanomechanics called optomechanics, where the mutual interaction between the mechanical resonator and the electromagnetic field allows for the realization of unprecedented non-classical states. Besides their ability to access the quantum regime, such optomechanical systems hold great promise for the realization of quantum interfaces between solid state quantum bits and photons [90], therefore attracting lot of interest for quantum computation and quantum information processing [103].

Nowadays, the potential of optomechanics in the future of quantum technologies (referred as the *second quantum revolution* [21]) is becoming unquestionable. Nevertheless, what might be questionable is the possibility to operate quantum-optomechanical systems at room temperature [77], where thermal dissipation imposes severe limitations to the quantum coherence of the oscillator modes. Modern nano-optomechanics has come a long way toward

solutions to the dissipation challenge, but clamping and material losses still limit its performances.

Novel approaches are therefore desirable. *Levitation* was introduced as a promising alternative to overcome the limits of dissipation and was indeed able to achieve outstanding $Q \times f$ factors (figure of merit for the coherence of an oscillating mechanical system) as high as 10^{13}. Similar values were only recently reached with trampoline resonators [77, 87]. Despite being bound by the photon recoil limit, optical levitodynamics enabled unprecedented levels of phonon occupancy at room temperature [50], letting foresee potential for advancing the state-of-the-art in quantum control at room temperature and, more importantly for the scope of this thesis, toward a novel family of ultra-sensitive nano-sensors.

1.2 The emerging field of *Levitodynamics*

In 1970 Artur Ashkin[1] from the Bell Laboratories realized that it was possible to exploit laser radiation pressure to manipulate matter at the microscale. His pioneering experiments, at first performed in liquid and air, demonstrated for the first time optical trapping of dielectric spheres in a focused laser beam [7]. It was the very beginning of a new and promising technology - later on named 'optical tweezers' - that opened up a plethora of applications in several different fields [71]. The scientific revolution that optical tweezers enabled in biology and biophysics [63, 105], with experiments essentially carried out in liquid, diverted the attention from levitation in vacuum, back in the times uniquely explored by Ashkin and Dziedzic [8]. Only many years later, in 2010, Li et al. [60] explored the potential of optical trapping in rarified gases and exploited the technique to measure the instantaneous velocity of a brownian particle, a task that A. Einstein in 1907 deemed impossible [26]. This result led one year later to the realization of an active feedback scheme to cool down the center of mass motion of a micron-sized particle in the millikelvin regime [61]. The technique was further developed by Gieseler et al. who proposed a non-linear parametric feedback scheme to levitate and cool a silica nanoparticle in high vacuum with a single beam [35] (as opposed to the six counterpropagating beams of Li et al.). It was, again, a technological progress that paved the way for a field that has recently been referred as Levitodynam-

[1] "For the optical tweezers and their application to biological systems", Arthur Ashkin was very recently awarded the 2018 Nobel prize in physics.

ics [2].

The potential of levitodynamics resulted clear since its very early stages. Unprecedented mechanical Q-factors as high as 10^8 at room temperature let foresee the possibility to achieve quantum ground state of mechanical motion in non-cryogenic environments. Jain et al. [50] proposed a slightly different feedback scheme and demonstrated a direct measurement of photon recoil from a levitated nanoparticle. With an occupation number of few tens of phonons, their results are currently the state-of-the-art towards the quantum ground state. However, it is essential mentioning that active feedback is not the only approach to perform cooling on a levitated nanoparticle. There are currently several groups implementing passive cooling schemes through optical cavities in the resolved sideband regime [6,54]. Making use of quadrupole ion (Paul) traps [18,20,70] instead of optical tweezers can facilitate this task since heating rates are typically lower in this implementation [15]. Also, different trap geometries have been recently proposed and implemented, for example in front of a parabolic mirror [47,111], in optical standing waves [85] or based on magnetic levitation [48,84].

It is clear from the list above (incomplete for obvious reasons), that the increasing number of research groups joining the levitodynamics community and the related *quantum race* is a tangible indication of significant scientific interest in levitated systems. It is paramount, though, to ask ourselves in which sense this could be different, or complementary, to what has been already achieved with other optomechanical systems (see § 1.1). The answer is clearly not unique, but in this context it is important to stress that one of the very peculiar features of levitated spheres cooled to the ground state is the exceptional possibility of performing free falling experiments [45] in a matter-wave interferometer scheme, therefore exploring wavefunction collapse models and achieve a better understanding of the decoherence effects of gravity [52].

Besides the high interest in performing quantum experiments with levitated nanoparticles, I believe "*there's (still) plenty of room in the classic world*". This personal and adapted version of Feynmann's quote intends to stress that the quite unique features of levitated nanoparticles (such as isolation from the environment, small masses and tunability of several system parameters) allow for cutting-edge fundamental research not only in the quantum regime,

[2] The name was recently conceived in October 2018, during informal brainstorming discussions between the groups of Lukas Novotny, Romain Quidant, Oriol Romero-Isaart, Christoph Dellago and Tracy Northup

but also in classical fields like stochastic thermodynamics [97] and statistical physics, among others. For instance, transient fluctuations of the relative entropy change in a relaxation process were observed due to the non-negligibility of thermal fluctuations at the particle's (nano) scale [37]. Likewise, the experimental measurement [93] of predicted (but yet unobserved) phenomena such as Kramers' turnover [40, 57] are likely to become textbook material in the future.

From a more application-oriented perspective in the classic regime, levitodynamics in vacuum is undoubtly a promising candidate for the realization of ultra-sensitive nano-sensors that operate at room temperature. The unprecedented decoupling of the levitated oscillator from its environment has already enabled the observation of thermal nonlinearities, with prediction [36] and demonstration [86] of force sensitivities in the $\mathrm{zN}/\sqrt{\mathrm{Hz}}$ (zeptonewton) range. Such outstanding sensitivities, combined with relatively high mass densities, are being used for the exploration of short-range interactions in regimes unaccessible for ions and cold atoms, for example in the search for non-Newtonian gravity-like forces. Moreover, the possibility to control and preserve the net charge of the particle [29] is a unique feature of a levitated system that is pivotal to electrically couple the particle to external electric fields [47, 73]. Doing so in a controlled manner could turn levitated nanoparticles into precise electric field sensors. Finally, modern nanotechnology rises high interest in inertial sensing for navigation, and levitated micro-particles (micro- not nano- because acceleration sensitivity scales linearly with the mass) were recently implemented as accelerometers and demonstrated nano-g sensitivity [72].

1.3 Motivation and objectives

At the onset if this doctoral work, levitated nanoparticles in vacuum were amongst the most promising nanomechanical systems able to reach unprecedented force sensitivities at room temperature. Yet, proposals of possible applications did not take into account important issues such as a reliable calibration of the particle's displacement and a precise measurement protocol of its mass (essential for quantitative estimation of the detected forces). Also, the levitodynamics community was coping with an unexpected particle loss mechanism at moderate vacuum conditions. Several groups, independently of the specific set-up, had observed instabilities of the system that were supposed to be related with the particle's bulk temperature [85]. Although the problem was later technically solved and particle loss avoided, a comprehensive understanding of the involved phenomena was missing. Different in-

terpretations (or perhaps speculations) let to inconsistent assumptions on the particle's morphology after the instability regime.
In such a context, one must realize that a deep knowledge of a system is paramount (and mandatory) in order to achieve full control and convert it into a reliable sensor.

This thesis has been devoted to solve some of these open issues, with interest was in the calibration and mass measurement problem. Moreover, the observation and explanation of pressure-dependent mass losses and their relation with the above mentioned instabilities ended up in an in-depth understanding of the behavior of silica while it is brought into high vacuum. Finally, the implementation of an electrical driving scheme with individual elementary charge detection, and the exploration of an unconventional sensing scheme based on the non-linear phenomenon of stochastic resonance gave us unprecedented control over the dynamics of the trapped nanoparticles. The next section provides a more detailed outline of the present work.

1.4 Outline

The thesis comprises four different parts, respectively presenting the theoretical background (Chapter 2), the experimental apparatus (Chapter 3), the three main experiments performed (Chapters 4-6) and the final conclusions (Chapter 7):

◇ **Chapter 2: Theory of optically levitated nano-resonators**. In § 2.1 the essential background on optical levitation is presented. We will provide a detailed derivation of the trapping forces on dielectric spheres, and of the far-field scattered intensity that enables interferometric detection of the particle's position. § 2.2, reviews the basics of mechanical resonators, with particular interest in the nonlinear dynamics of Duffing resonators subject to both direct and parametric driving.

◇ **Chapter 3: Experimental set-up**. We provide a description of the whole experimental apparatus, focusing on modifications and improvements of its original state [34], including the implementation of a novel electric driving scheme.

◇ **Chapter 4: Precise measurement of the particle's mass.** This chapter starts with a review of the two main methods used in the community to

estimate the particle's mass. In § 4.3 a novel protocol to perform this task is suggested and experimentally demonstrated. The chapter is concluded with a careful estimation of the associated measurement errors, showing an accuracy that outperforms the existing methods by more than an order of magnitude.

◇ **Chapter 5: Particle instabilities through moderate vacuum.** Here, an in-depth description of the particle's morphology is provided. The chapter contains two main parts, separated by a more technical one on charge measurement. The first, § 5.2, is an observational section where unexpected pressure-dependent behaviors are identified, while § 5.4 present a plausible interpretation of the experimental results provided. In this last section we dig into the surface chemistry of silica, and eventually propose a model that convincingly explains the formerly unclear behavior.

◇ **Chapter 6: A model system for stochastic bistable dynamics.** In this chapter the stochastic nonlinear dynamics of a parametrically driven particle is investigated in different regimes. The first part, § 6.3 characterizes the particle's response at the first instability tongue and under externally injected noise. Then, stochastic switching of the oscillator motion is studied. Finally, levereaging on the control achieved and on the precise modelling of the bistable dynamics, we implement stochastic resonance (SR) with the levitated nanoparticle. The potential of this phenomenon as a signal amplification scheme is investigated and the chapter concludes discussing its sensing capabilities.

◇ **Chapter 7: Conclusions and future perspectives.** A general outlook of the work, presenting both technical improvements and experimental results, is followed by our vision on possible future applications in levitodynamics.

2

Theory of optically levitated nano-resonators

Contents

In 1970 Arthur Ashkin proposed and demonstrated a novel technique to trap and accelerate microparticles by exploiting the radiation pressure of a focused laser beam. This pioneering work gave birth to a groundbreaking field, later on named optical tweezers, that revolutionized the way to manipulate matter in a controlled manner. For his contributions, Ashkin was awarded the 2018 Nobel prize in Physics.

In § 2.1 we provide the basic concepts of optical levitation. When this takes place in vacuum, however, optically trapped objects behave as three-

dimensional oscillators and a complete description of their dynamics therefore relies in the basic concepts of mechanical resonators. These will be reviewed in § 2.2, both in their linear (§ 2.2.1) and nonlinear (§ 2.2.3-2.2.4) regime of oscillations.

2.1 Optical tweezers

An object immersed in an electric field scatters part of the incident radiation. The physics of this scattering phenomenon depends on the size of the object itself. In the case of a spherical particle, given the characteristic length (e.g. its radius r_p) and the wavelength λ of the impinging radiation, one can parametrize the scattering via the quantity

$$\sigma = \frac{2\pi r_p}{\lambda}. \tag{2.1}$$

Three very different cases emerge:

$$\begin{cases} \sigma \ll 1 \rightarrow \text{Rayleigh scattering} & (2.2) \\ \sigma \simeq 1 \rightarrow \text{Mie theory} & (2.3) \\ \sigma \gg 1 \rightarrow \text{Geometric optics} & (2.4) \end{cases}$$

In the experimental condition encountered all along this thesis, condition 2.2 is always fulfilled and we can restrict ourselves to study the case of Rayleigh scattering: $\sigma \ll 1$. Consider now a monochromatic electromagnetic wave of angular frequency ω, represented by the fields:

$$\begin{aligned} \mathbf{E}(\mathbf{r},t) &= \mathrm{Re}[\mathbf{E}(\mathbf{r})e^{-i\omega t}] \\ \mathbf{B}(\mathbf{r},t) &= \mathrm{Re}[\mathbf{B}(\mathbf{r})e^{-i\omega t}] \end{aligned} \tag{2.5}$$

When such fields impinge on a subwavelength particle at position $\mathbf{r}_0$ the internal charges gets displaced, therefore inducing a dipole moment $\mathbf{p}$ proportional to the electric field:

$$\mathbf{p} = \alpha(\omega)\mathbf{E}(\mathbf{r}_0). \tag{2.6}$$

Here the constant α is referred as the polarizability of the particle, and is given by

$$\alpha(\omega) = 4\pi\varepsilon_0 r_p^3 \frac{\varepsilon_p(\omega) - \varepsilon_s(\omega)}{\varepsilon_p(\omega) + 2\varepsilon_s(\omega)}, \tag{2.7}$$

with $\varepsilon_{0,p,s}$ being the dielectric constants of vacuum, particle and surrounding medium respectively. The force acting on the polarized particle can now be expressed as:

$$\mathbf{F} = (\mathbf{p}\cdot\nabla)\mathbf{E} + \dot{\mathbf{p}}\times\mathbf{B} + \dot{\mathbf{r}}\times(\mathbf{p}\cdot\nabla)\mathbf{B}. \tag{2.8}$$

Neglecting third term due to non-relativistic speeds involved, and considering the time-averaged force over one cycle of oscillation of the electromagnetic field ($T = 2\pi/\omega$), equation (2.8) takes the more familiar form:

$$\langle \mathbf{F} \rangle = \frac{\alpha'}{2} \sum_{i=x,y,z} \mathrm{Re}[E_i^* \nabla E_i] + \frac{\alpha''}{2} \sum_{i=x,y,z} \mathrm{Im}[E_i^* \nabla E_i] \tag{2.9}$$

$$= \mathbf{F}_{\mathrm{grad}}(\mathbf{r}) + \mathbf{F}_{\mathrm{scatt}}(\mathbf{r}), \tag{2.10}$$

where we have used $\alpha = \alpha' + i\alpha''$. The first term in (2.9) is a conservative *gradient force*, proportional to the dispersive part of the complex polarizability, that can be rewritten as

$$\mathbf{F}_{\mathrm{grad}}(\mathbf{r}) = \frac{\alpha'}{4} \nabla [\mathbf{E}^* \cdot \mathbf{E}] = \frac{\alpha'}{2c\varepsilon_0} \nabla I(\mathbf{r}), \tag{2.11}$$

with $I(\mathbf{r}) = c\varepsilon_0 |\mathbf{E}(\mathbf{r})|^2/2$ being the intensity of the field. Provided $\alpha' > 0$ this force always points towards the the maximum of the intensity and is the one that enables trapping with a single tightly focused light beams. The second term in (2.9), often referred as *scattering force* instead, is a non conservative force proportional to the dissipative part of the complex polarizability. It is responsible for "pushing" the particle along the propagation axis of the beam by transferring momentum to it. Again, we can relate $\mathbf{F}_{\mathrm{scatt}}$ to the field's intensity I_0 and phase ϕ at the center of the trap:

$$\mathbf{F}_{\mathrm{scatt}}(\mathbf{r}) = \frac{\alpha''}{2} I(\mathbf{r}) \nabla \phi(\mathbf{r}). \tag{2.12}$$

Important considerations need to be done regarding the complex polarizability $\alpha(\omega)$. In the case of a dielectric sphere of volume V levitated in vacuum (i.e. $\varepsilon_s = 1$), we can rewrite (2.7) as $\alpha_0 = 3V\varepsilon_0(\varepsilon_p - 1)/(\varepsilon_p + 2)$. The response of the particle to the external oscillating field depends on the external field, obviously, but also on the field scattered by the particle itself. In order to ensure energy conservation this mutual interaction with the self-scattered field leads to a corrections of α_0 and to the introduction of an effective polarizability [78]:

$$\alpha(\omega) \approx \alpha_0(\omega) \left[1 - i \frac{k^3}{6\pi\varepsilon_0} \alpha_0 \right]. \tag{2.13}$$

2.1.1 Optical forces in the Gaussian approximation

As already mentioned, a small particle ($r_p \leq \lambda/2\pi$) can be trapped in a tightly focused optical beam as as long as the gradient force F_{grad} overcomes the scattering force F_{scatt} (see eq. 2.10). To compute those forces we need information

over the intensity and phase profiles in the focus, $I(\mathbf{r})$ and $\phi(\mathbf{r}) = \mathbf{k}\cdot\mathbf{r}$ respectively, $\mathbf{k}$ being the local wave vector. A first approach is to assume a zero order Gaussian optical mode, which is fully described by its complex amplitude:

$$\mathbf{E}(\mathbf{r}) = E_0 \frac{w_0}{w(z)} \exp\left[-\frac{\rho^2}{w^2(z)}\right] e^{-i\phi(\rho,z)} \hat{\mathbf{e}}_x, \tag{2.14}$$

where we have defined:

$$w(z) = w_0\sqrt{1+\left(\frac{z}{z_0}\right)^2} \qquad \text{Beamwidth} \tag{2.15}$$

$$\phi(\rho,z) = kz + \frac{\rho^2}{2R(z)} - \zeta(z) \qquad \text{Phase} \tag{2.16}$$

$$R(z) = z\left[1+\left(\frac{z_0}{z}\right)^2\right] \qquad \text{Curvature radius} \tag{2.17}$$

$$\zeta(z) = \arctan\left(\frac{z}{z_0}\right) \qquad \text{Gouy phase shift} \tag{2.18}$$

The beam propagates along the $\hat{\mathbf{e}}_z$ direction, while $\hat{\mathbf{e}}_x$ is the unit vector along the polarization axis. E_0 is the absolute value of the field at the focus, related to the the total optical power P_0 by $E_0^2 = 4P_0/c\varepsilon_0\pi w_0^2$, w_0 is the so called beam waist, and $z_0 = \pi w_0^2/\lambda$ is the Rayleigh length.

Using the paraxial approximation to assume $w_0 = \lambda/\pi NA$ (NA being the numerical aperture of the focusing optical element), and by expanding the Gaussian beam up to the fourth order (valid for small displacement $|\mathbf{r}| << \lambda$), one can show [51] that the the total gradient force takes the vectorial form:

$$\mathbf{F}_{\text{grad}} \approx -\begin{pmatrix} k^{(x)}x \\ k^{(y)}y \\ k^{(z)}z \end{pmatrix}, \tag{2.19}$$

being

$$k^{(x,y)} = \frac{4\alpha' P_0}{\pi\varepsilon_0 c w_0^4} = \frac{4\alpha'}{\pi\varepsilon_0 c}\left(\frac{\pi NA}{\lambda}\right)^4 P_0 \tag{2.20}$$

$$k^{(z)} = \frac{8\alpha' P_0}{\pi\varepsilon_0 c z_0^2 w_0^2} = \frac{8\alpha'}{\pi\varepsilon_0 c}\left(\frac{\pi NA}{\lambda}\right)^4 NA^2 P_0 \tag{2.21}$$

This expression establishes that gradient restoring forces in optical traps are linear in first order of position and consequently they obey *Hook's law* $F_{\text{grad}}^{(i=x,y,z)} = -k^{(i)}x_i$. For this reason the constants $k^{(i)}$ are often referred as optical spring constant, proportional to the optical power. Figure 2.1a shows the

intensity map of a Gaussian beam at its focus for $\lambda = 1064$ nm, $w_0 = 635$ nm and $P_0 = 70$ mW. White crosscuts correspond to the field intensity along the (x, y)-plane and (x, z)-plane. The resulting gradient forces for a silica nanoparticle, $d_p = 143$ nm in diameter are shown in Fig. 2.1b together with the linear restoring force approximation (2.19). It is clear from the plots that this approximation only applies for small displacements of the resonator. We will study in more depth the consequences of larger displacements in § 2.2.2.

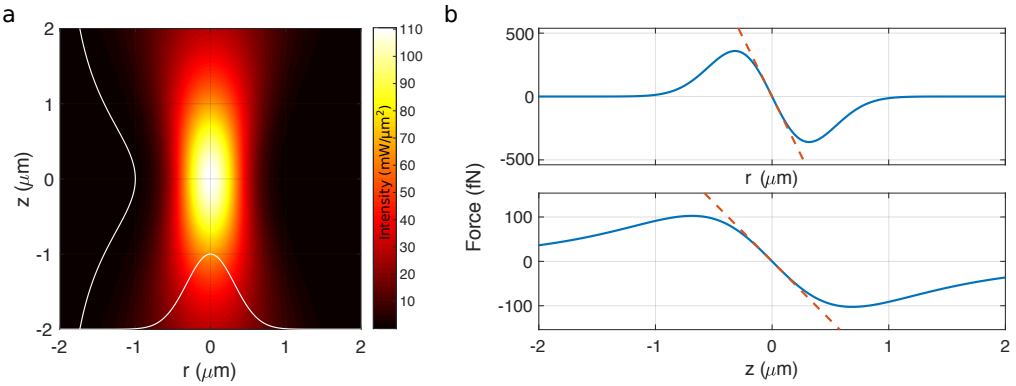

Figure 2.1: **Optical field and gradient forces in an optical tweezer**. (a) Intensity map of Gaussian beam focused down to $w_0 = 635$ nm. Power and wavelength are respectively $P_0 = 70$ mW and $\lambda = 1064$ nm. (b) Gradient forces for a dielectric particle $d_p = 143$ nm in diameter, immersed in the optical field shown in (a). Note that the waist w_0 here considered does not correspond to the the one predicted by the paraxial approximation with a $NA = 0.8$. In fact, due to the poor validity of such approximation, the parameter w_0 needs to be rescaled by a factor ~ 1.5 in order to match experimental observations.

Similarly, for the scattering force one obtains [49]:

$$\mathbf{F}_{\text{scatt}} \approx \frac{\alpha'' E_0^2 k}{2 z_0^2} \begin{pmatrix} xz \\ yz \\ \gamma + \gamma_x x^2 + \gamma_y y^2 + \gamma_z z^2 \end{pmatrix}, \tag{2.22}$$

where the z-component coefficients are defined as:

$$\gamma = z_0^2 \left(1 - \frac{1}{z_0 k}\right) \tag{2.23}$$

$$\gamma_x = \gamma_y = \frac{1}{2} - \frac{2 z_0}{k w_0^2} + \frac{2 z_0^2}{w_0^2} \tag{2.24}$$

$$\gamma_z = \frac{1}{z_0} \left(\frac{2}{k} - z_0\right) . \tag{2.25}$$

$$\tag{2.26}$$

Most of the times, however, the need for high gradient forces that are able to overcome the scattering ones lead to the use of high *NA* optical elements to tightly focus the beam. This restricts the validity of the paraxial approximation and requires a more general treatment of the problem. For instance one could follow the theory established by Richards and Wolf [78,89] and describe the field at the focus as an infinite superposition of plane waves that travel from the optical element's surface (assumed to be spherical) towards the focus. The corresponding integral can be expressed in the angular spectrum representation [78] as:

$$\mathbf{E}(\rho,\varphi,z) = \frac{ikfe^{-ikf}}{2\pi}\int_0^{\theta_{\max}}\int_0^{2\pi}\mathbf{E}_\infty(\theta,\phi)e^{ikz\cos\theta}e^{ik\rho\sin\theta\cos(\phi-\varphi)}\sin\theta\,\mathrm{d}\phi\,\mathrm{d}\theta\,, \tag{2.27}$$

with $\mathbf{E}_\infty(\theta,\phi)$ being the incoming field distribution at the optical element of focal length f, k the wave vector, and $\theta_{\max}$ the maximum angle under which rays are entering in the lens (ultimately depending on the numerical aperture *NA*). Although being exact, this approach is most of the times a very complicated task, and the integral in (2.27) can be analytically solved in very limited cases. An easier approach is then to reconsider the Gaussian approximation, this time including some corrections due to the high *NA* of the focusing. In fact, the plane waves associated with high angles generate new polarizations in the focus, the symmetry of the light beam is broken, and the light distribution becomes elongated along the polarization axis of the impinging beam. In this case the focal distribution would be described by an asymmetric Gaussian beam of the form:

$$\mathbf{E}(\mathbf{r}) = E_0\frac{1}{1+\left({}^{z}/_{z_0}\right)^2}\exp\left[-\frac{x^2}{w_x^2(z)}-\frac{y^2}{w_y^2(z)}\right]e^{-i\phi(\rho,z)}\hat{\mathbf{e}}_x\,. \tag{2.28}$$

$$k_x = \frac{4\alpha' P_0}{\pi\varepsilon_0 c w_{0x} w_{0y}}\frac{1}{w_{0x}^2} \tag{2.29}$$

$$k_y = \frac{4\alpha' P_0}{\pi\varepsilon_0 c w_{0x} w_{0y}}\frac{1}{w_{0y}^2} \tag{2.30}$$

$$k_z = \frac{16\alpha' P_0}{\pi\varepsilon_0 c w_{0x} w_{0y}}\frac{1}{w_{0z}^2} \tag{2.31}$$

where we have defined $w_{0z} = \sqrt{2}z_0$.

Note that due to the radiation pressure the the equilibrium position of the trapped particle along the beam axis does not coincide with the focus, but gets forward displaced by z_p. This value can be obtained from setting the condition

$F^{(z)}_{\text{grad}} = F^{(z)}_{\text{scatt}}$, which leads to:

$$z_p = \frac{1}{4}\frac{\alpha''}{\alpha'} k\gamma \ . \tag{2.32}$$

2.1.2 Trapping potential

The optical forces computed in §2.1.1 can now be converted into an optical potential. This will be useful to introduce and model the anharmonicities that arise in the particle's dynamics.

The trapping potential can only be defined for the conservative components, i.e. the gradient force, and we will therefore neglect the non-conservative scattering force. By Integrating (2.11), we obtain:

$$U_{\text{opt}}(\mathbf{r}) = -\frac{\alpha'}{2c\varepsilon_0} I(\mathbf{r}). \tag{2.33}$$

The optical potential corresponds to the (inverted) Gaussian intensity distribution $I(\mathbf{r})$. For an analytical approach, it is convenient to expand this potential up to the fourth order. Notice that due to the the symmetry of the problem only even terms play a role:

$$\begin{aligned} U_{\text{opt}}(\mathbf{r}) \approx U_0 \Big[-1 &+ \frac{2}{w_{0x}^2}x^2 + \frac{2}{w_{0y}^2}y^2 + \frac{2}{w_{0z}^2}z^2 + \\ &- \frac{2}{w_{0x}^4}x^4 - \frac{2}{w_{0y}^4}y^4 - \frac{4}{w_{0z}^4}z^4 + \\ &- \frac{4}{w_{0x}^2 w_{0y}^2}x^2y^2 - \frac{8}{w_{0x}^2 w_{0z}^2}x^2z^2 - \frac{8}{w_{0y}^2 w_{0z}^2}y^2z^2 \Big], \end{aligned} \tag{2.34}$$

where $U_0 = \alpha' P_0/(\pi\varepsilon_0 c w_{0x} w_{0y})$. The first term corresponds to the depth of the potential at the center of the trap, while the quadratic terms with prefactors proportionals to the trap stiffness $k_{x,y,z}$ respectively, represent the harmonic part of the potential that leads to the linear restoring force $F^{(i=x,y,z)}_{\text{grad}} = -k^{(i)}x_i$. Finally, the quartic terms represents deviations from the harmonic case, due to the Gaussian shape of the potential. More precisely, the three terms of the second row represent nonlinearities of the decoupled modes (i.e. of one dimensional oscillators), while the last three terms correspond to cross-coupling between the different modes of oscillation.

2.1.3 Scattered Field

At the beginning of the chapter we have introduced the dipole approximation, according to which the small particle ($r \ll \lambda$) trapped in the focus scatters a

certain amount of the impinging light. The phase of this scattered light depends on the particle position. Consequently, the interference pattern produced by the sum of the transmitted (reference) field and the scattered field also depends on the particle's position, and this relations can be exploited for detecting the motion of the particle in the trap with high precision.

Following the derivation given in [78], one can show that the field scattered by the dipole $\mathbf{p} = \alpha\mathbf{E}$, at the position $\mathbf{r}_\mathrm{p} = (x_\mathrm{p}, y_\mathrm{p}, z_\mathrm{p})$ is:

$$\mathbf{E}_\mathrm{dp}(\mathbf{r}) = \frac{\alpha E_0 \omega^2 \mu_0}{4\pi|\mathbf{r}|}\frac{w_0}{w(z_\mathrm{p})} e^{-\left(\frac{x_\mathrm{p}^2}{w_{ox}} + \frac{y_\mathrm{p}^2}{w_{oy}}\right)} \exp\left[i\left(k|\mathbf{r}| - k\frac{\mathbf{r}\cdot\mathbf{r}_\mathrm{p}}{|\mathbf{r}|}\right)\right]\hat{\mathbf{e}}_x \tag{2.35}$$

$$= E_\mathrm{dp}(\mathbf{r}, \mathbf{r}_\mathrm{p}) \exp\{i[kf + \phi_\mathrm{dp}(\mathbf{r}, \mathbf{r}_\mathrm{p})]\}\hat{\mathbf{e}}_x \,, \tag{2.36}$$

where we have assumed that the incident field is polarized along the $\hat{\mathbf{e}}_x$ axis. For small displacements of the particle ($|\mathbf{r_p}| \ll w_{0x}, w_{0y}, z_0$), the amplitude $E_\mathrm{dp}(\mathbf{r}, \mathbf{r}_\mathrm{p})$ depends weakly on the dipole position, and can therefore be rewritten as $E_\mathrm{dp}(\mathbf{r}) \approx \alpha E_0 \omega^2 \mu_0/(4\pi|\mathbf{r}|)$. If the scattered light is collected with a lens of focal length f_cl, the spherical wavefronts emitted by the dipole are transformed into plane waves. The far-field at longitudinal position z' behind the lens will therefore be given by the dipole field at the surface of the so called reference sphere $\mathbf{r}_\mathrm{cl} = (x, y, z_\mathrm{cl})$ of radius f_cl, combined with the propagation terms of an ideal lens: $\exp(-ikf_\mathrm{cl})\exp(ikz')$. The collimated scattered field at a position $\mathbf{r}' = (x, y, z')$ behind the collection lens will therefore have amplitude and phase given respectively by:

$$E_\mathrm{dp}^{FF}(\mathbf{r}') = E_\mathrm{dp}(f_\mathrm{cl}) = \frac{\alpha E_0 \omega^2 \mu_0}{4\pi f_\mathrm{cl}} \tag{2.37}$$

$$\phi_\mathrm{dp}^{FF}(\mathbf{r}, \mathbf{r}_p) = \mathbf{k}'\mathbf{r}' - ikz_p\left(1 - \frac{\rho^2}{2f_\mathrm{cl}^2}\right) \tag{2.38}$$

where in (2.38) we have defined $\mathbf{k}' = (-kx_\mathrm{p}/f_\mathrm{cl}, -ky_\mathrm{p}/f_\mathrm{cl}, k)$, $\rho = x^2 + y^2$ and expanded $z_\mathrm{cl} \approx f_\mathrm{cl} - \frac{\rho^2}{2f_\mathrm{cl}}$. See Fig. 2.2 for a detailed geometry of the system considered.

The transmitted field, i.e. the one not scattered by the particle, can be assumed to be the simple forward propagation of the Gaussian field to the reference sphere. Being $f_\mathrm{cl} \gg z_0$, the transmitted Gaussian displays spherical wavefronts that are converted into plane waves by the collection lens:

$$\mathbf{E}_\mathrm{ref}(\mathbf{r}') \approx \frac{E_0 z_0}{f_\mathrm{cl}} \exp\left[i\left(kz' - \frac{\pi}{2}\right)\right] \,. \tag{2.39}$$

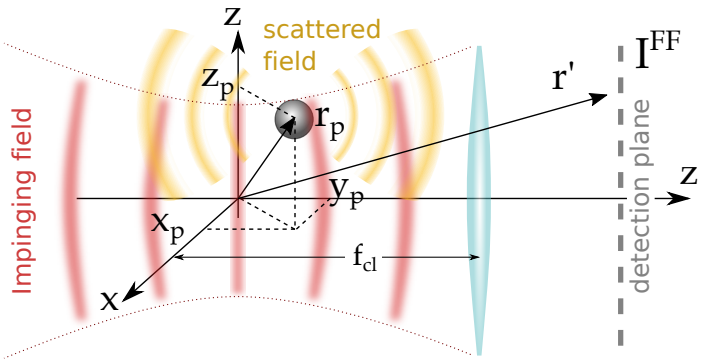

Figure 2.2: **Optical field scattered from the levitated nanoparticle.** A particle levitated at position $\mathbf{r}_p$ scatters a certain amount of the impinging field focused at the origin. The far field intensity pattern behind a collection lens placed at position $z = f_{cl}$ carries information on the particle position due to the interference between the transmitted and the scattered light. Processing the propagated beam allows to retrieve information on the particle's dynamics.

Detecting the superposition of the scattered and transmitted components in the far field, leads to an interference intensity pattern of the two fields:

$$I^{FF}(\mathbf{r}', \mathbf{r}_p) = \frac{c\varepsilon_0}{2}\left|\mathbf{E}_{dp}(\mathbf{r}', \mathbf{r}_p) + \mathbf{E}_{ref}(\mathbf{r}')\right|^2 \tag{2.40}$$

$$\approx \frac{c\varepsilon_0}{2}|\mathbf{E}_{ref}|^2 + c\varepsilon_0 \,\mathrm{Re}\left[\mathbf{E}_{ref}\mathbf{E}^*_{dp}\right] \tag{2.41}$$

$$\approx \frac{c\varepsilon_0}{2}|\mathbf{E}_{ref}|^2 + \frac{\alpha E_0^2 z_0 \omega^2}{4\pi c f_{cl}^2} e^{-ik\left[\frac{x x_p}{f_{cl}} + \frac{y y_p}{f_{cl}} - z_p\left(1 - \frac{\rho^2}{2f_{cl}^2}\right) + \frac{\pi}{2k}\right]} \tag{2.42}$$

where in (2.41) we have dropped the intensity emitted by the dipole being this small compared to the other two, and we have used (2.37),(2.38) and (2.39) to obtain (2.42). This equation explicitly shows that the interference pattern at the detector embeds information on the position $\mathbf{r}_p = (x_p, y_p, z_p)$ of the particle.

2.2 Dynamics of nano-resonators

Inside of the trapping potential, optically levitated dielectric nanoparticles behave as three dimensional nano-resonators. The theoretical background of these systems is provided in this section, starting with the simple description of the harmonic oscillator and its properties. Important definitions such as power spectral density and force sensitivity will provide a preparatory *know-how* for tackling both analytical and experimental analysis of the experiments detailed in the following chapters. The simple harmonic oscillator model will

be then extended to a more realistic context by introducing the nonlinear dynamics of resonators in the case of direct and parametric driving.

2.2.1 Linear regime of oscillations

The harmonic oscillator (HO) is a textbook example of a very common dynamical system and surely the simplest model of a mechanical resonator. It describes the dynamics of any mechanical system subject to a restoring conservative force proportional to the displacement of the system itself.

In the case of the Simple Harmonic Oscillator (SHO) the equation of motion reads:

$$m\ddot{q} = F_{\text{res}} = -kq, \tag{2.43}$$

where m is the mass of the system, $\ddot{q} = \mathrm{d}q/dt^2$ represents the second derivative of position q with respect to time, corresponding to its acceleration, and F_{res} is a restoring elastic force that, according to Hook's law, depends on the stiffness k of the HO (sometimes also called spring constant) and on its displacement. Notice that we have here introduced the variable q to represent a general coordinate of the oscillator. In the case of a leviatated nanoresonator, considered as 3D harmonic oscillator, one would have $q = x, y, z$.

The solution of (2.43) is a harmonic oscillation of the form:

$$q(t) = q_0 \cos(\Omega_0 t + \phi), \tag{2.44}$$

where q_0 and ϕ are respectively amplitude and phase of the oscillation, determined by the initial conditions $\{q(0), \dot{q}(0)\}$, while $\Omega_0 = 2\pi f_0$ is the mechanical oscillation frequency, also called *eigenfrequency*, related to the stiffness by $\Omega_0 = \sqrt{k/m}$.

Under realistic conditions, however, any resonator experiences friction forces due to its interaction with the environment and energy gets dissipated via viscous damping. A more appropriate form of the equation of motion would therefore read

$$m\ddot{q} + \gamma\dot{q} + kq = 0, \tag{2.45}$$

where we have introduced the viscous damping coefficient γ. Again, (2.45) can be easily solved and the dynamics of the system is described by:

$$q(t) = q_0 e^{-\frac{\Gamma}{2}t} \cos\left[\Omega_0 \sqrt{1 - \left(\frac{\Gamma}{2\Omega_0}\right)^2}\, t + \phi\right], \tag{2.46}$$

$\Gamma = \gamma/m$ being the damping rate. The eigenfrequency of the system is now $\Omega_r = \Omega_0\sqrt{1 - (\frac{1}{2Q})}$, where the quality factor $Q = \Omega_0/\Gamma$ is an important

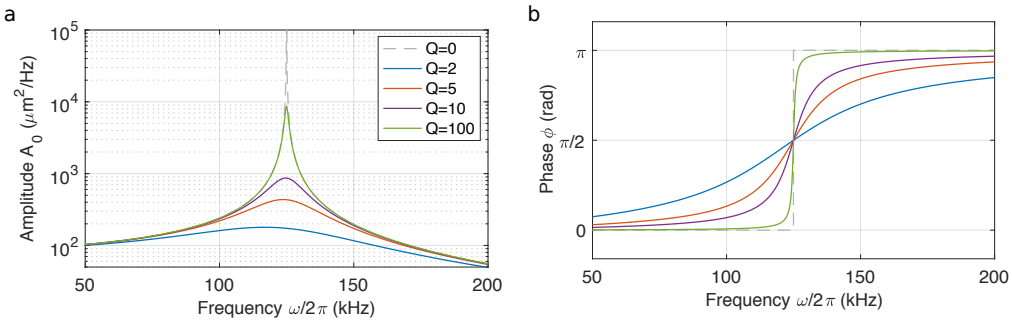

Figure 2.3: **Response of a driven damped harmonic oscillator** (a) Amplitude. (b) Phase

parameter that represents the number of oscillations of the system when its amplitude decays by a factor e. In other words, Q measures the ability of a system to store energy, and its value leads to completely different behaviors of the resonator:

- $Q < 1/2 \rightarrow$ *Overdamped oscillator*: the system does not show oscillatory behaviour and slowly returns to its equilibrium position with exponentially decaying amplitude
- $Q \sim 1/2 \rightarrow$ *Critically damped oscillator*: the system does not show oscillatory behaviour and returns to its equilibrium position as quickly as possible
- $Q > 1/2 \rightarrow$ *Underdamped oscillator*: the system oscillates at frequency Ω_r and returns to its equilibrium position with amplitude gradually decreasing to zero.

The equations of motion (2.43) and (2.45) describe the free harmonic oscillator. However, a more interesting and realistic case takes place when an external force $F(t)$ acts on the system, an the equation of motion takes the form:

$$m\ddot{q} + \gamma\dot{q} + kq = F(t) \tag{2.47}$$

If the force is harmonic $F(t) = F_0 \cos(\omega_{dr} t)$, the solution has an initial transient (dependent on the initial conditions) and a steady state solution of the form:

$$q(t) = \frac{F_0/m}{\sqrt{\left(\omega_{dr}^2 - \Omega_0^2\right)^2 + \Gamma^2\omega_{dr}^2}} \cos\left[\omega_{dr} t + \arctan\left(-\frac{\omega_{dr}\Gamma}{\Omega_0^2 - \omega_{dr}^2}\right)\right] \tag{2.48}$$

The amplitude and the phase of (2.48) are graphically represented in Fig. 2.3 for different values of the damping Γ, parametrized in terms of Q.

Another interesting case of (2.47) is when the damped harmonic oscillator is stochastically driven, which for instance takes place when the external

force $F(t)$ is the thermal noise arising from random collisions between the resonator and the gas molecules of the surrounding media. According to the so-called fluctuation-dissipation theorem, this coupling with the surrounding thermal bath provides both forcing and dissipation in the system. As a result, similarly to what has been done for (2.45), the dynamics of the resonator highly depends on the amount of damping. In the following we will study both the overdamped and underdamped limit cases and extract the relevant quantities that characterize the dynamics of the system. Before doing so, it is useful to provide the following definitions.

We define the Fourier Transform (FT) and its Inverse (IFT) in the ordinary frequency domain as:

$$\tilde{q}(f) = \int_{-\infty}^{\infty} q(t) e^{-i2\pi f t} \mathrm{d}t \qquad \text{FT (ordinary frequency)} \tag{2.49}$$

$$q(t) = \int_{-\infty}^{\infty} \tilde{q}(f) e^{i2\pi f t} \mathrm{d}f \qquad \text{IFT (ordinary frequency)} \tag{2.50}$$

while in the angular frequency space $\omega = 2\pi f$ these takes the form:

$$\tilde{q}(\omega) = \int_{-\infty}^{\infty} q(t) e^{-i\omega t} \mathrm{d}t \qquad \text{FT (angular frequency)} \tag{2.51}$$

$$q(t) = \frac{1}{2\pi} \int_{-\infty}^{\infty} \tilde{q}(\omega) e^{i\omega t} \mathrm{d}\omega \qquad \text{IFT (angular frequency)} \tag{2.52}$$

Note that for derivatives in the time domain the definition given above ensures the validity of:

$$\frac{\mathrm{d}^n q(t)}{\mathrm{d}t^n} = (i\omega)^n \tilde{q}(\omega) \qquad \text{Time derivatives in Fourier space} \tag{2.53}$$

For time-continuous signals (having infinite total energy) it is convenient to define:

$$_{\mathcal{T}}\tilde{q}(\omega) = \frac{1}{\sqrt{\mathcal{T}}} \int_0^{\mathcal{T}} q(t) e^{i\omega t} \mathrm{d}t \qquad \text{Time-limited FT} \tag{2.54}$$

$$S_q(\omega) = \lim_{\mathcal{T}\to\infty} \frac{1}{\mathcal{T}} \left| \int_0^{\mathcal{T}} q(t) e^{i\omega t} \mathrm{d}t \right|^2 \qquad \text{Power Spectral Density (PSD)} \tag{2.55}$$

$$= \lim_{\mathcal{T}\to\infty} |_{\mathcal{T}}\tilde{q}(\omega)|^2 \tag{2.56}$$

$$= \int_{-\infty}^{\infty} \langle\, q(t) x(t+\tau) \rangle\, e^{i\omega\tau} \mathrm{d}\tau \qquad \text{Wiener-Khintchine theorem} \tag{2.57}$$

Finally, energy conservation requirements allow to link the variance of the temporal signal to the Power SPectral Density (PSD) in the frequency domain:

$$\langle q^2(t)\rangle = \frac{1}{2\pi}\int_{-\infty}^{\infty} S_q(\omega)\mathrm{d}\omega \qquad \text{Parseval's theorem} \tag{2.58}$$

Overdamped regime

In overdamped conditions the inertial term $m\ddot{x}(t)$ in (2.47) can be dropped ($m \to 0$), and making use of (2.52) and (2.53), the equation of motion in the frequency domain reads:

$$i\omega\gamma\tilde{q}(\omega) + k\tilde{q}(\omega) = \tilde{F}_{\mathrm{th}}(\omega). \tag{2.59}$$

From the definition (2.55), we obtain:

$$S_q(\omega) = \lim_{\mathcal{T}\to\infty} \frac{|\mathcal{T}\tilde{F}_{\mathrm{th}}(\omega)|^2}{\gamma^2(\omega_c^2+\omega^2)} = \frac{\sigma^2}{\gamma^2(\omega_c^2+\omega^2)}\,, \tag{2.60}$$

where for the second equality we have defined the corner frequency $\omega_c = 2\pi f_c = k/\gamma$ and set $S_{F_{\mathrm{th}}} = \lim_{\mathcal{T}\to\infty}|\mathcal{T}\tilde{F}_{\mathrm{th}}(\omega)|^2 = \sigma^2$ making use of the fact that thermal noise is white (i.e. it has a constant frequency-independent spectrum). To extract information over the physical meaning of σ we can combine eq. (2.55) and the equipartition principle, which states that the average potential energy of a HO takes the form:

$$\langle E_{pot}\rangle = \frac{1}{2}k\langle q^2(t)\rangle = \frac{1}{2}k_BT, \tag{2.61}$$

k_B being the Boltzman's constant and T the bath temperature. In agreement with the fluctuation-dissipation theorem, we obtain $\sigma^2 = 2k_BT\gamma$ and the PSD of an overdamped oscillator can be finally expressed as:

$$S_q(\omega) = \frac{k_BT}{\pi\gamma(\omega_c^2+\omega^2)} \tag{2.62}$$

Underdamped regime

Similarly, we can now apply the same approach for the underdamped case ($Q \ll 1/2$). Starting with a mass-normalized equation of motion

$$\ddot{q} + \Gamma\dot{q} + \Omega_0^2 q = \frac{F_{\mathrm{th}}(t)}{m} \tag{2.63}$$

and again using identity (2.53), we obtain

$$|\tilde{q}(\omega)|^2 = \frac{1}{m^2\left[\left(\omega^2-\Omega_0^2\right)^2+\Gamma^2\omega^2\right]}\cdot|\tilde{F}_{\mathrm{th}}(\omega)|^2\,. \tag{2.64}$$

The PSD of the stochastically driven underdamped HO therefore reads:

$$S_q(\omega) = \frac{2k_B T\Gamma}{m\left[\left(\omega^2 - \Omega_0^2\right)^2 + \Gamma^2\omega^2\right]} \tag{2.65}$$

Multiple driving: Thermal and harmonic forcing

Because thermal noise is basically everywhere and unavoidable, a very common situation is that of a harmonic force acting on a thermally driven harmonic resonator. As a result, the force $F(t)$ in (2.47) is a contribution of two terms:

$$F(t) = F_{\text{th}}(t) + F_{\text{dr}}(t) = \sigma\eta(t) + F_0\cos(\omega_{\text{dr}}t), \tag{2.66}$$

where $\eta(t)$, representing the white noise, has a Gaussian probability distribution that satisfies $\langle\eta(t)\eta(t+t')\rangle = \delta(t')$. Again, the equation of motion in the frequency domain leads to:

$$\tilde{q}(\omega) = \frac{1}{m(\Omega_0^2 - \omega^2 + i\Gamma\omega)}\left[\tilde{F}_{\text{th}}(\omega) + \tilde{F}_{\text{dr}}(\omega)\right] \tag{2.67}$$

$$= \tilde{\chi}(\omega)\cdot\tilde{F}(\omega) \tag{2.68}$$

where this time we have introduced $\tilde{\chi}(\omega) = [m(\Omega_0^2 - \omega^2 + i\Gamma\omega)]^{-1}$ as the fourier transform of the complex susceptibility $\chi(t) = \chi'(t) + i\chi''(t)$, also referred as the response (or transfer) function in linear response theory. This function converts the input signal, i.e. the force $F(t)$ into the output signal, i.e. the displacement $q(t)$, such that:

$$q(t) = \int_{-\infty}^{\infty}\chi(t-t')F(t')\mathrm{d}t' \,. \tag{2.69}$$

Notice that due to the linearity of the system, $\chi(\omega)$ acts independently on the two different forcing terms. As a result, if these are uncorrelated (as it is the case between a periodic signal and a random process), we can write $S_q(\omega) = S_q^{\text{th}}(\omega) + S_q^{\text{dr}}(\omega)$. The first term in this expression has already been calculated in eq. (2.65), while for the second one a few preliminary considerations are necessary. The exact analytical expression of $\tilde{F}_{\text{dr}}(\omega)$ is a Dirac delta peaking at ω_{dr}, which for obvious reasons it is not a physical result to be compared with experiments. In fact, in any realistic condition the force signal $F_{\text{dr}}(t)$ will be observed acting on the system just for a finite time $\mathcal{T}$. We will therefore be allowed to rewrite the definition (2.55) as $S_q = |_{\mathcal{T}}\tilde{q}|^2$, obtaining a driving force

spectral density of the form:

$$S_{F_{\rm dr}} = |\mathcal{T}\tilde{F}_{\rm dr}|^2 = \left|\frac{1}{\sqrt{\mathcal{T}}}\int_0^{\mathcal{T}} F_0\cos(\omega_{\rm dr}t)e^{-i\omega t}{\rm d}t\right|^2 \tag{2.70}$$

$$= \frac{F_0^2\tau}{2}\left|e^{-i\omega_+\tau}{\rm sinc}\left(\omega_+\tau\right) + e^{-i\omega_-\tau}{\rm sinc}\left(\omega_-\tau\right)\right|^2 \tag{2.71}$$

$$= \frac{F_0^2\tau}{2}[2\,{\rm sinc}(\omega_+\tau)\,{\rm sinc}(\omega_-\tau)\cos(2\omega_{\rm dr}\tau) + {\rm sinc}^2(\omega_+\tau) + {\rm sinc}^2(\omega_-\tau)] \tag{2.72}$$

$$\approx \frac{F_0^2\tau}{2}\,{\rm sinc}^2(\omega_-\tau)\;.. \tag{2.73}$$

where we have set $\omega_\pm = \omega \pm \omega_{\rm dr}$ and $\tau = \mathcal{T}/2$. Finally, the overall PSD of a thermally driven mechanical resonator subject to external harmonic force reads:

$$S_q(\omega) = \frac{2k_BT\Gamma}{m\left[\left(\omega^2-\Omega_0^2\right)^2+\Gamma^2\omega^2\right]} + \frac{F_0^2\tau\,{\rm sinc}^2[(\omega-\omega_{\rm dr})\tau]}{2m^2\left[\left(\omega^2-\Omega_0^2\right)^2+\Gamma^2\omega^2\right]} \tag{2.74}$$

Figure 2.4a verifies the approximation made in (2.74), while in Fig. 2.4b we show the separate contributions on a thermally and harmonically driven resonator according to (2.74). As expected the response to the harmonic driving is dominant only in a narrowband region around $\omega_{\rm dr} = 130$ kHz, while the broad thermal spectrum $S_q^{\rm th}$, calculated for $Q = 10$, overcomes $S_q^{\rm dr}$ everywhere else.

Force sensing

The example above presented can be extended to the general case of resonant force sensing, where thermal noise $F_{\rm th}$ and other possible noise sources limit the sensitivity of the system in detecting a resonant external force $F_{\rm ext}(t)$. The overall measured power spectral density can be assumed to take the general form:

$$S_q(\omega) = |\chi(\omega)|^2\cdot[S_{F_{\rm ext}}(\omega) + S_{F_{\rm th}}] + \zeta^2 \tag{2.75}$$

where we have also introduced an additional term ζ^2 representing the white gaussian measurement noise in our system (i.e. independent from the oscillator dynamics). As a result, by inverting eq. (2.75) to estimate $S_{F_{\rm ext}}$, we find:

$$|\chi(\omega)|^{-2}S_q(\omega) = \underbrace{S_{F_{ext}}(\omega)}_{signal} + \underbrace{S_{F_{\rm th}} + |\chi(\omega)|^{-2}\zeta^2}_{noise\ terms}\;, \tag{2.76}$$

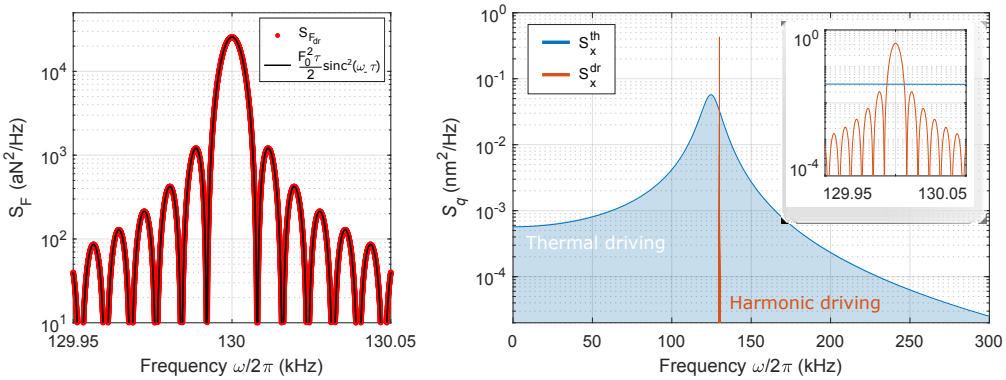

Figure 2.4: **Thermally and harmonically driven resonator** (a) Red dots, representing the exact analytical prediction of a harmonic force spectral density $S_{F_{dr}}$ are well approximated by (2.74). The parameters here used are: $F_0 = 1.6$ fN, $\mathcal{T} = 40$ ms, $\omega_{dr} = 130$ kHz. (b) Power spectral density of a thermally and harmonicaly driven oscillator according to (2.74). For the harmonic contribution the same parameters as in (a) are used, while the thermal one correspond to a resonator with $m = 3$ fg, $Q = 10$, $\Omega_0 = 125$ kHz, $T = 300$ K.

and the signal to noise ratio (SNR) therefore reads:

$$SNR = \sqrt{\frac{S_{F_{ext}}(\omega)}{S_{F_{th}} + |\chi(\omega)|^{-2}\zeta^2}} = \sqrt{\frac{S_{F_{ext}}(\omega)}{\sigma^2 + |\chi(\omega)|^{-2}\zeta^2}} \tag{2.77}$$

where for the second equality we have once more used $S_{F_{th}} = \sigma^2$. Equation (2.77) clearly demonstrates the advantage of using a resonator as a force sensor. In fact, the signal to noise ratio is bounded to the limit $SNR \leq \sqrt{S_{F_{ext}}/\sigma^2}$, and reaches its maximum when the term $|\chi(\omega)|^{-2}\zeta^2$ is minimized. This condition is fulfilled by operating the resonator on resonance, i.e. when $\omega = \Omega_0$. In other words, the resonance allows to enhance the effect of small forces that would be otherwise buried in measurement noise. By setting $SNR|_{\omega=\Omega_0} = 1$ as the condition that defines sensitivity, we eventually find:

$$\sqrt{S_{F_{ext}}} \overset{Q \gg 1}{\simeq} \sqrt{2m\Gamma k_B T + \zeta^2 m^2 \omega_0^2 \Gamma^2} \tag{2.78}$$

The second term is usually much smaller than the first one (at least when measuring close to resonance), so we can ultimately conclude that the sensitivity of a mechanical resonator is given by:

$$\sqrt{S_{F_{ext}}} = \sqrt{2m\Gamma k_B T}\,, \tag{2.79}$$

$$F_{min} = \sqrt{4m\Gamma k_B T b}\,. \tag{2.80}$$

We have here reported also the minimum detectable force (2.80) after integration in a bandwidth $b = 1/\mathcal{T}$ ($\mathcal{T}$ being the measurement time). Although being formally correct, this formula does not take into consideration the stability of the measuring system: one could in principle resolve an infinitely small force just by integrating over longer times (or shorter bandwidth). This is obviously limited by drifts of the resonance peak that would affect the response of the system to the external force. As we will see in § 4.3.4, there is always an optimal measuring time that maximizes the stability and poses a realistic limit to the achievable force detection capability.

2.2.2 Nonlinear regime of oscillations

In the previous section we have described the dynamics of a mechanical resonator in the linear regime of oscillation. This assumption requires the restoring force to be linear in the displacement from its equilibrium position. Consequently the effective potential associated to the conservative force has to be quadratic in the displacement. Although being a good and useful approximation in several cases, we know from §2.1.2 that this does not apply for the trapping potential of an optical tweezer. From eq. (2.34), in fact, we already see that correction to the quadratic assumption are necessary to match the Gaussian intensity profile in the trapping field. Limiting ourselves to study the 1-D problem along the x–mode, and neglecting the mixed terms, one can rewrite (2.34) as:

$$U_{\mathrm{opt}}^{(x)} \approx -U_0 + \frac{2}{w_{0x}^2}x^2 - \frac{2}{w_{0x}^4}x^4 \tag{2.81}$$

and consequently:

$$F_{\mathrm{grad}}^{(x)} = m\Omega_0^2\left(1 + \xi x^2\right)x\ . \tag{2.82}$$

A resonator subject to such a nonlinear restoring force is called a *Duffing* oscillator [56], with the nonlinear part usually referred as the Duffing term.

Together with stiffness nonlinearities, the general problem of a nonlinear resonator usually implicates additional damping terms, also nonlinear, that depend on the oscillation amplitude. This situation is very typical in mechanical resonator such as suspended beams, cantilevers, membranes and others [25, 62, 100], where high oscillation amplitudes introduce mechanical stresses in the material that cause the linear damping term to acquire higher order contributions. In the case of a levitated nanoparticle under parametric feedback cooling, mechanical stresses do not play a role and the (linear) damping is solely related to collision with gas molecules in the environment. However, when feedback cooling schemes [35] are applied in order to confine

the oscillation to lower amplitudes, the corresponding optical forces introduce nonlinear damping terms very much like the ones above described. Therefore, we include this contribution by considering an overall damping force of the form:

$$F_\gamma = (\gamma + m\Omega_0\eta x^2)\dot{x} \tag{2.83}$$

2.2.3 Directly driven Duffing resonator

We can now reconsider the linear equation of motion of a harmonically driven damped mechanical resonator and include the nonlinear terms introduced in § 2.2.2. This reads:

$$\frac{\mathrm{d}^2q}{\mathrm{d}t}(t) + \left[\Gamma + \Omega_0\eta q^2(t)\right]\frac{\mathrm{d}q}{\mathrm{d}t}(t) + \Omega_0^2\left[1 + \xi q^2(t)\right]q(t) = \frac{F_0}{m}\cos(\omega_{\mathrm{dr}}t) \tag{2.84}$$

To simplify the notation[1] we introduce a dimensionless time variable $\tau = \Omega_0 t$ and a dimensionless displacement $x = \sqrt{|\xi|}q$ and divide Eq. (2.84) by a factor $\Omega_0^2/\sqrt{|\xi|}$, obtaining:

$$\boxed{\ddot{x} + \kappa\dot{x} + \tilde{\eta}x^2\dot{x} + x + \mathrm{sgn}(\xi)x^3 = \tilde{F}_0\cos(\tilde{\omega}\tau)} \tag{2.85}$$

where we have introduced $\kappa = Q^{-1}$, $\tilde{\eta} = \frac{\eta}{\xi}$, $\tilde{F}_0 = \frac{F_0\sqrt{\xi}}{m\Omega_0^2}$, $\tilde{\omega} = \frac{\omega_{\mathrm{dr}}}{\Omega_0}$. The sign function $\mathrm{sgn}(\xi)$ allows a general description of both softening ($\xi < 0$) and a hardening ($\xi > 0$) nonlinearities. However, to match our experimental conditions and avoid confusion we will from here on consider $\xi < 0$ and drop the sign function from our notation.

We will now proceed to solve this nonlinear differential equation using secular perturbation theory. This is done in the limit of weak linear damping rate Γ which is used to define the small expansion parameter $Q^{-1} \equiv \kappa \ll 1$. Requiring the Duffing term to be a factor κ smaller than the linear displacement leads to the following ansatz:

$$x^3 \propto \kappa x \rightarrow x \propto \sqrt{\kappa} \qquad \Rightarrow x(t) = \frac{1}{2}\sqrt{\kappa}\left[a(T)e^{i\tau} + c.c.\right] + \mathcal{O}(\kappa^2) \tag{2.86}$$

$$x \propto Q\tilde{F}_0 \rightarrow \tilde{F}_0 = \kappa^{3/2}f \qquad \Rightarrow F(t) = \kappa^{3/2}f\cos[(1 + \kappa\Omega)\tau] \tag{2.87}$$

The explicit form of $x(t)$ in (2.86) relies on the so called *Slow Varying Envelope Approximation* (SVEA) that assumes a fast oscillation of the form $e^{i\tau}$ with a slow complex amplitude $a(T)$ that changes over a timescale $T = \kappa\tau \ll \tau$. The

[1] These theoretical sections § 2.2.3 and § 2.2.4 follow the approach of Lifshitz and Cross [62]

oscillating force $\cos[(1+\kappa\Omega)\tau]$, instead, is only considered sufficiently close to the resonant condition $\tilde{\omega}=1$.

Looking for a perturbative solution, we will now calculate individual terms of the equation of motion (2.85) making use the above ansatz and retain only the terms of the order of $\kappa^{3/2}$ that do not display fast oscillation $\{e^{n\cdot it}, n \in \mathbb{N} \wedge n > 1\}$:

$$\ddot{x} \approx i\kappa^{3/2}\frac{\mathrm{d}a}{\mathrm{d}T}e^{i\tau} + c.c. \tag{2.88a}$$

$$\kappa\dot{x} \approx \frac{1}{2}\kappa^{3/2}ia(T)e^{i\tau} + c.c. \tag{2.88b}$$

$$x^3 \approx \frac{3}{8}\kappa^{3/2}|a|^2ae^{i\tau} + c.c. \tag{2.88c}$$

$$\tilde{\eta}x^2\dot{x} \approx \frac{1}{8}\kappa^{3/2}i\tilde{\eta}|a|^2ae^{i\tau} + c.c. \tag{2.88d}$$

Plugging in Eqs. (2.86) to (2.88) into the equation of motion we obtain a differential equation for the slow varying envelope $a(T)$:

$$\frac{\mathrm{d}a}{\mathrm{d}T} = -\frac{1}{2}a - \frac{\tilde{\eta}-3i}{8}|a|^2a - i\frac{f}{2}e^{i\Omega T}\ . \tag{2.89}$$

An interesting approach is to ignore initial transients and to consider only the steady state of the directly driven Duffing resonator. To do so we look for solutions $a(T) = Ae^{i(\Omega T+\phi)}$, which correspond to an oscillatory behavior at the driving frequency $\omega_0(1+\Omega T)$. For such a steady state, equation (2.89) reads:

$$\left[\left(\frac{3}{4}A^2 - 2\Omega\right) + i\left(1 + \frac{\tilde{\eta}}{4}A^2\right)\right] = f\ , \tag{2.90}$$

leading to the recursive amplitude solution:

$$A^2 = \frac{f^2}{\left(2\Omega - \frac{3}{4}A^2\right)^2 + \left(1+\frac{1}{4}\tilde{\eta}A^2\right)^2} \tag{2.91}$$

$$q_0^2 = \frac{\left(\frac{F_0}{2m\Omega}\right)^2}{\left(\omega - \Omega_0 - \frac{3}{8}\xi\Omega_0 q_0^2\right)^2 + \left(\frac{\Gamma}{2} + \frac{1}{8}\eta\Omega_0 q_0^2\right)^2} \tag{2.92}$$

Where in (2.92) we've converted the solution back to the original physical quantities $q(t) = q_0\cos(\omega t)$. A careful analysis of these equations allows us to draw few important observations. Firstly, we see that in the limit of $\xi, \eta \to 0$ the response is formally identical to that of a linear (harmonic) driven damped oscillator (see eq. 2.48). The presence of such nonlinerar terms converts the

solution into a cubic polynomial in $|a|^2$ and therefore there exist in principle three solutions for $|a|$, one of which is unstable. Secondly, for $f = const.$, the maximum of the curve is reached at the condition: $2\Omega - 3/4A^2 = 0$, which in terms of the physical units reads:

$$\Omega_{NL} = \Omega_0 + \Delta\Omega_{NL} = \Omega_0 + \frac{3}{8}\Omega\xi A^2. \tag{2.93}$$

As a result, the eigenfrequency Ω_{NL} of a nonlinear resonator depends on the mode amplitude itself, and gets downshifted (when $\xi < 0$) for high oscillation amplitudes.The situation can be easily understood imaging the particle oscillating in a realistic Gaussian potential: for small amplitudes the potential is quasi-harmonic and the eigenfrequency is well defined by the quadratic term of the potential. However, when exploring the outer regions of the trap, where the potential becomes broader (shallower) than the quadratic approximation, the particle travels larger displacements and as a consequence its oscillation frequency decreases.

Regarding the solutions of equation (2.90), if the driving amplitude is sufficiently strong the number of solutions changes from one to three and back to one again, therefore determining the presence of two saddle-node bifurcations. These are singular points where the derivative of the solution diverges to infinity. We can investigate this condition by differentiating (2.91):

$$\left[\frac{3}{64}\left(\eta^2+9\right)A^4 + \frac{1}{4}\left(\eta - 6\Omega\right)A^2 + \left(\frac{1}{4}+\Omega^2\right)\right]\mathrm{d}A^2 = \left[\frac{3}{4}A^2 - 2\Omega A^2\right]\mathrm{d}\Omega\,. \tag{2.94}$$

Imposing the singular condition $\mathrm{d}\Omega/\mathrm{d}A^2 = 0$ and solving for Ω we find the position of the two saddle-node bifurcations as:

$$\Omega_{\pm}^{\mathrm{sn}} = \frac{3}{4}A^2 \pm \frac{1}{2}\sqrt{\frac{3}{16}\left(3-\eta^2\right)A^4 - \eta A^2 - 1}\,. \tag{2.95}$$

Figure 2.5a shows the numerical solution (2.91) for $f = 5$ and $\eta = 0.1$, with stable branches in solid color and the unstable one in blue dashed line. The vertical gray dashed lines identify the two saddle-node bifurcations $\Omega_{\pm}^{\mathrm{sn}}$ calculated in (2.95). It is easy to foresee in this representation the hysteretic response that depends on whether the driving signal is swept across the resonance starting from higher or lower frequencies. To extend this into the (Ω, f) parameter space, Fig. 2.5b dispays the same solution (2.91) as a 2D surface.

2.2.4 Parametrically driven Duffing resonator

Another interesting case for the purposes of this thesis is that of a parametrically driven Duffing resonator. Parametric driving is substantially different

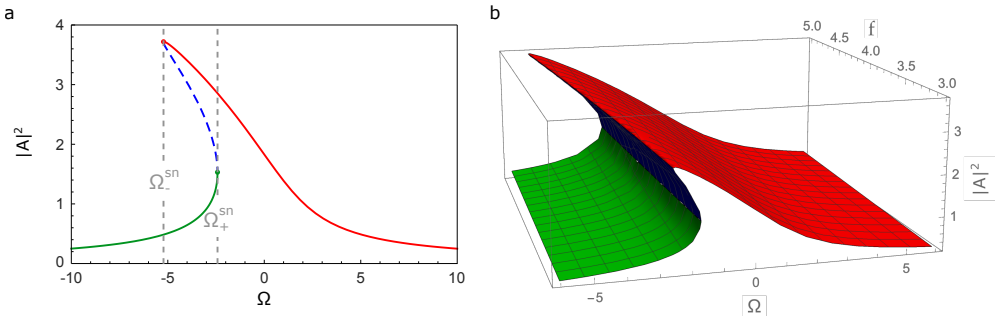

Figure 2.5: **Amplitude response of a directly driven duffing resonator.** (a) Numerical solution of (2.91) for $\eta = 0.1$ and $f = 5$. Linear stability analysis shows that only the upper (red) and lower (green) branches are stable, while the solution within the two saddle-node bifurcations $\Omega_-^s n < \Omega < \Omega_+^s n$ (dashed blue) is unstable. (b) A 3D representation of the solution in the parameters phase space (Ω, f).

from direct driving and consists in a time-dependent modulation of a physical parameter of the resonator. One of the most typical cases of parametric driving encountered in nano-mechanical resonators is that of a resonantly modulated stiffness, that in the specific case of a levitated particle translates into a modulation of the optical spring, i.e. of the laser intensity. The equation of motion, in terms of the physical quantities, can now be written as:

$$\frac{\mathrm{d}^2 q}{\mathrm{d}t}(t) + \left[\Gamma + \Omega_0 \eta q^2(t)\right] \frac{\mathrm{d}q}{\mathrm{d}t}(t) + \Omega_0^2 \left[1 + \xi q^2(t) + \epsilon \cos(\Omega_\mathrm{m} t)\right] q(t) \approx 0 \quad (2.96)$$

where we have defined $(\Omega_\mathrm{m}, \epsilon)$ the modulation frequency and the modulation depth of the parametric driving respectively. Note that we have approximated the right hand side of the equation to zero. A rigorous treatment of the problem should involve the stochastic thermal driving force. However we will assume in the following that the parametric driving term is dominant, and will consider negligible the thermal motion of the resonator. Again, by applying the same normalization of the directly driven case (see eq. 2.84, 2.85) we can rewrite a simplified adimensional equation of motion:

$$\boxed{\ddot{x} + \kappa \dot{x} + \tilde{\eta} x^2 \dot{x} + \left[1 + \epsilon \cos(\tilde{\omega}\tau)\right] x - x^3 \approx 0} \quad (2.97)$$

where this time $\tilde{\omega} = \Omega_\mathrm{m}/\Omega_0$. The most efficient parametric driving takes place when $\Omega_\mathrm{m} \sim 2\Omega_0$, in which case we modulate the stiffness of the spring twice per cycle. However, it is in general possible to drive the system every n^{th} multiple of half a period, therefore obtaining a set of resonances given by the condition: $\{\Omega_\mathrm{m} = \frac{2\Omega_0}{n}, n \in \mathbb{N}^+\}$. Each of these conditions will determine a so-called instability tongue, and in the content of this thesis we will focus

on the first instability tongue, therefore assuming $\Omega_m = \Omega_0(2 + \delta_m)$, with $\delta_m = \Omega_m/\Omega_0 - 2$ defined as the normalized detuning.

To follow the same procedure of the directly driven case (see § 2.2.3), we convert the parametric driving term into the SVEA as:

$$\epsilon \cos(\tilde{\omega}\tau)x = \kappa\tilde{\epsilon}\cos(\tilde{\omega}\tau)x = \frac{1}{4}\kappa^{3/2}\tilde{\epsilon}a^* e^{i(\tilde{\omega}-2)\tau}e^{i\tau} \tag{2.98}$$

and by inserting this in the equation of motion, we obtain the equivalent of eq. (2.89) that reads:

$$\frac{da}{dT} = -\frac{1}{2}a - \frac{\tilde{\eta} - 3i}{8}|a|^2 a + \frac{1}{4}i\tilde{\epsilon}a^* e^{i\tilde{\delta}_m T} \tag{2.99}$$

where $\tilde{\delta}_m = \delta_m/\kappa$ is a rescaled detuning that operates in the slow time domain, such that $\delta_m\tau = \tilde{\delta}_m T$.

First instability tongue

Taking a closer look at eq. (2.99), one can show the presence of an instability in the dynamics of the resonator that sets self sustained oscillations above a certain threshold ϵ_c of the parametric modulation. Intuitively, such an instability arises from a phenomenon similar to a positive feedback loop: higher oscillation amplitudes lead to a higher parametric forcing (because of the proportionality to x), which in turns drives the resonator to higher oscillation amplitudes, and so on. Such an amplification phenomenon reaches a steady state only thanks to nonlinear damping terms that introduce a saturation of the exponential growth of the amplitude. An easy approach to obtain information on the onset of this instability is to start neglecting the nonlinear terms and study the linearized equation of motion:

$$\frac{da}{dT} \simeq -\frac{1}{2}a - i\tilde{\epsilon}a^* e^{i\tilde{\delta}_m T}\,. \tag{2.100}$$

We seek for a solution of the form:

$$a(t) = Ae^{\sigma T}e^{i\tilde{\delta}_m T}\,, \tag{2.101}$$

where σ corresponds to the exponential growth ($\sigma > 0$) or decay ($\sigma < 0$) rate and the other exponential term describes the oscillation at half the pump frequency. Plugging (2.101) into (2.100) and requiring $\sigma > 0$ we obtain the instability condition as:

$$\tilde{\epsilon} > 2\sqrt{1 + \tilde{\delta}_m} \;\rightarrow\; \epsilon > \frac{2}{Q}\sqrt{1 + Q^2\delta_m} \tag{2.102}$$

Amplitude response above threshold

For the purposes of this thesis we're interested in the dynamics of the resonator above the instability threshold, i.e. in the nonlinear regime of oscillation. To study this regime we go back to consider the equation of motion (2.99), and look for a steady state solution of the form:

$$a(t) = Ae^{i\left(\tilde{\delta}_m T/2+\phi\right)} . \tag{2.103}$$

Substituting (2.103) into (2.99), we obtain a quadratic equation for $|A|^2$ that reads:

$$\left(\tilde{\delta}_m - \frac{3}{4}|A|^2\right)^2 + \left(1 + \frac{\tilde{\eta}}{4}|A|^2\right)^2 = \left(\frac{\tilde{\epsilon}}{2}\right)^2 . \tag{2.104}$$

Equation (2.104) can be solved for $|A|^2$ providing the two amplitude solutions:

$$|A|^2_{\pm} = \frac{2\left[6\tilde{\delta}_m - 2\tilde{\eta} \pm \sqrt{\epsilon^2\left(\tilde{\eta}^2+9\right) - 4\left(\tilde{\delta}_m\tilde{\eta}+3\right)}\right]}{\tilde{\eta}^2+9} . \tag{2.105}$$

Note that $A(t) = 0$ is also a trivial solution of (2.99). For completeness and to match theory with experiments, we convert (2.105) back to physiscal quantities:

$$q_0^2 = \frac{1}{\eta\delta_{th}^2}\left[\frac{3\xi}{\eta}\delta_m + \frac{1}{Q} \pm \sqrt{\epsilon^2\delta_{th}^2 - \delta_m^2 + \frac{3\xi}{\eta}\frac{1}{Q^2}\left(2Q\delta_m - \frac{3\xi}{\eta}\right)}\right] \tag{2.106}$$

$$\approx \frac{1}{\eta\delta_{th}^2}\left[3\frac{\xi}{\eta}\delta_m \pm \sqrt{\epsilon^2\delta_{th}^2 - \delta_m^2}\right] \tag{2.107}$$

where $\delta_{th} = \sqrt{9\xi^2+\eta^2}/2\eta$ and q_0 is the physical oscillation amplitude defined as $q_0^2 = 2\langle q^2\rangle$. Notice that the approximation made in (2.107) is valid for $Q \gg 1$.

In Figure 2.6 we show the solutions $|a|^2$ as a function of the detuning $\tilde{\delta}_m$. Red, blue and green curves represent respectively $|a|^2_+$, $|a|^2_-$, and $|a| = 0$, while dashed lines indicates that the mode is unstable. Vertical grey dashed lines represent interesting conditions in the dynamics related with the limits of the instability region (see Eq. (2.102)).

Comparison between direct and parametric driving As final remarks of this chapter, it is interesting to go through a comparison (although mainly qualitative) between the resonator response to direct driving as opposed to parametric driving. As we will see in the next chapter § 3, our setup is provided with both these actuation schemes. Most of the measurements in the nonlinear

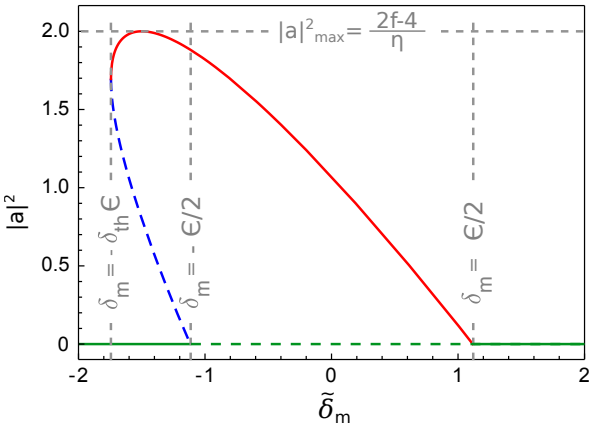

Figure 2.6: **Amplitude response of a parametrically driven duffing resonator.** Analytical solutions (2.105) for $\eta = 1$ and $\epsilon = 3$. Linear stability analysis shows that only the upper (red) and lower (green) branches are stable, while the solution for $\delta_{\text{th}}\epsilon < \delta_{\text{m}} < -\epsilon/2$ (dashed blue) is unstable.

regime have been performed with the parametric control. This turned out to be paramount to observe unique features in the stochastic bistable dynamics of the levitated oscillator.

Figure 2.7a and 2.7b show the bistable regime for both direct and parametric driving. In the former case this corresponds to the difference between the numerical solutions shown as red and green surfaces in Fig. 2.5b, while in the parametric case the bistable regime is identified by the diffrence between eq. (2.105) and the trivial $A = 0$ solution. For graphic reasons, in this latter case the whole instability tongue is displayed and the monostable regime is covered by a shaded area. One of the main differences that emerges in this comparison is the shape of the so-called *iso-amplitude lines*: subsets of the bistable regime that display a constant amplitude gap between the high and the low branch (in these 2D plots represented by the contours of the colormap). While in the parametric case it is possible to scan the whole width of the bistable regime by following an iso-amplitude line, this is not ensured in the direct driving case, where in order to follow a similar path one should considerably extend the explored parameter space towards very high drivings f. As we will see in § 6, this feature of the parametric driving will be of primary importance to achieve full control on the double-well potential associated with the bistable dynamics.

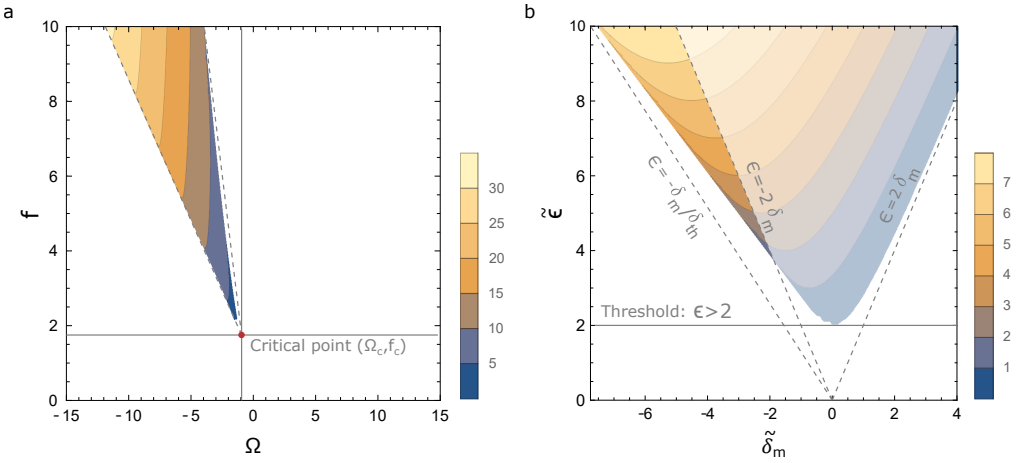

Figure 2.7: **Comparison between different driving schemes.** (a) Directly driven Duffing resonator. (b) Parametrically driven. In both cases we set $\eta = 0.1$

3
Experimental setup

Contents

3.1 Introduction

The experimental setup at the onset of this doctoral work was probably the state-of-the-art in the levitation of nanoparticles with a single tweezer beam [34]. It mainly comprised three parts: the optics, the vacuum setup and the parametric feedback electronics. These are described in §3.2 - 3.4.

While the overall scheme of the apparatus has remained unchanged, a consistent part of the work presented in this dissertation has been dedicated to improve the system in terms of both stability and full control. Moreover, an additional electrical actuation scheme was designed and implemented in the set-up. Section §3.5 provides a detailed description of this new part.

3.2 Optical setup

An overview of the whole experimental apparatus is given in Fig. 3.1. Function-wise, the optical setup can be divided into two sectors: the trapping side, and the detection scheme. In the former both a trapping beam and a detection (or probe) beam are prepared and sent into the vacuum chamber where the actual trapping takes place. In the latter, instead, only the probe beam is retained and processed for efficient detection of the particle's dynamics.

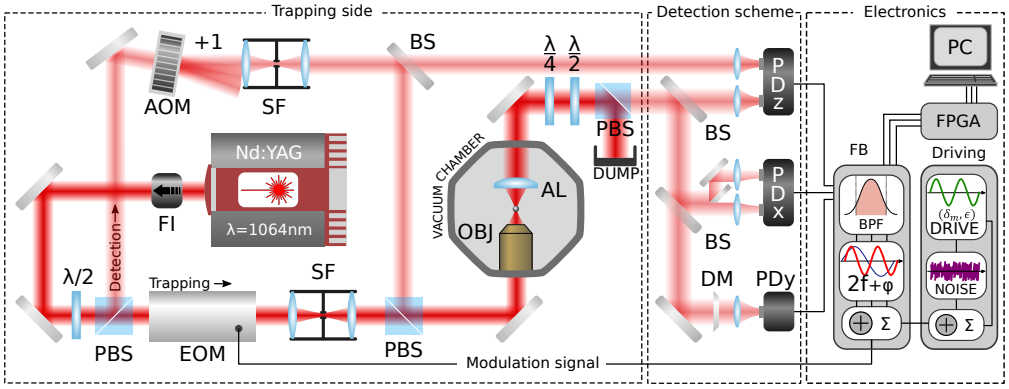

Figure 3.1: **Experimental set-up**. The optical setup comprises two main parts. In the the trapping side, both the trapping and the detection beam are prepared before entering in the vacuum chamber. The former is modulated in intensity by an EOM, the second is shifted in frequency by an AOM. In the detection side, the trapping beam is dumped while the detection beam is analyzed by means of balanced photoreceivers (PD). Finally, the electronics part consist of the feedback unit (FB), the driving signal and an FPGA for processing and recording the data.

Trapping side

The light source is a single frequency continous-wave solid state Nd:YAG laser[1], which is used to both trap the silica nanoparticle and detect its motion. The laser has an optical wavelength of $\lambda = 1064$ nm, a spectral linewidth of $\sim$ 1 kHz and it features extremely low relative intensity noise (RIN), which was characterized to be $RIN \simeq 120$ dB. A plot of the measured RIN spectral density is shown in Fig. 3.2a. As a comparison, the manufacturer noise specifications are provided in Fig. 3.2b. We observe a significant mismatch between the expected performances and our measurements [2]. The source of the measured excess of noise is unclear, but determined no tangible degradation

[1] Coherent Mephisto, 1W

[2] Similar mismatch has been observed also in other experiments [43, 49] using Coherent Mephisto lasers

of the experimental results. The laser beam first passes through a Faraday

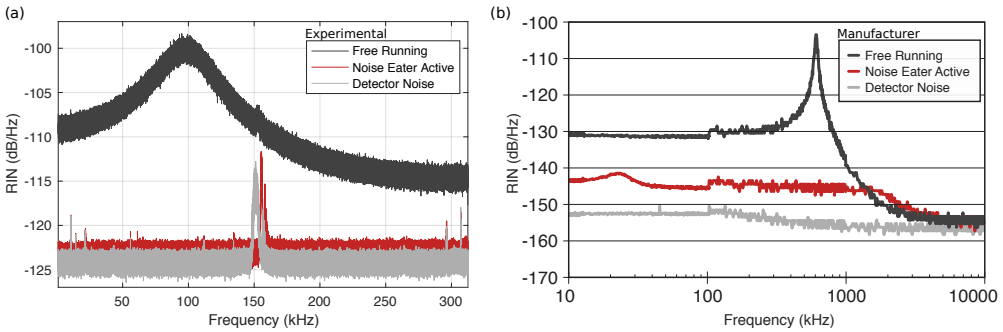

Figure 3.2: **Laser relative intensity noise**. (a) Free running (black) and noise suppressed (red) RIN of the Mephisto laser, compared to the detector noise (grey). The graph shows the ability of the internally built noise eater to reduce the RIN up to ~ 25 dB. Similar behaviour is expected according to the manufacturer specifications (b), although noise suppression should lower the RIN down to ~ -150 dB. Notice that the peak appearing at $f = 150$ kHz is not due to the optical field. It is indeed detected also in the detector noise spectral density, in the absence of a laser beam. Panel b) adapted from [1].

isolator[3], to block possible back reflections, and is then split into a high power branch (trapping beam) and a low power branch (detection or probe beam) by means of a polarizing beam splitter (PBS). We use an intensity ratio of $90 - 10$ which is tuned with a half-wave plate in front of the PBS. To decouple the two branches and to avoid interference in the laser focus we use cross polarized beams and we shift the frequency ($\Delta f \approx 110$ MHz) of the detection beam with an acousto-optic modulator[4] (AOM). The trapping beam passes through an electro-optic modulator[5] (EOM) that allows the parametric control of the particle. Both the AOM and the EOM distort the beams by introducing high spacial frequency components in their intensity distribution. It is therefore desirable to clean both beams by means of convenient spatial filtering (SF), which consists on focusing the beam through a 25 μm pinhole and recollimating it. Another advantage is that after filtering the two beams display the very same intensity distribution and size, which makes it easier to precisely superimpose them avoiding mismatches between the trapping potential and the probe one. After the SF, the two paths are recombined with a second PBS before entering in the vacuum chamber. Here, a high NA microscope objective[6] (OBJ) focuses the beams - creating the optical trap - and an aspheric lens[7] (AL) collects and

[3] Linos
[4] Brimrose 410-472-7070
[5] Conoptics 350-160
[6] Nikon Plan Fluor, 50x, $NA = 0.8$, wd $= 1$ mm
[7] Thorlabs AL1210 - $f = 10$ mm , $NA = 0.55$, C-coated

collimates the light, which is sent out of the chamber. After the vacuum chamber the two beams are again separated: the trapping beam is dumped, while the probe beam is sent towards the detection side. Efficient separation of the beams is paramount to avoid detecting the intensity modulation introduced by the EOM, that would then be fed into the system via the feedback loop. To this aim we place a couple of half- and quarter-wave plates before the PBS. In fact, due to the tight focusing and especially to the mechanical stresses present in the glass windows of the vacuum chamber, mixed polarization states appear in this side of the set-up. The combination of these two elements allows to get rid of most the residual trapping light that has gained the right polarization to leak through the PBS. After dumping the trapping beam and retaining the probe beam, this latter is sent towards the particle's detection set-up.

Detection scheme

In § 2.1.3, eq. (2.42), we provided analytical derivation of the far field interference pattern between the transmitted beam and the light scattered by the particle, showing how this pattern carries information on the position $\mathbf{r}_p = (x_p, y_p, z_p)$ of the particle itself. This feature is exploited to interferometrically detect the particle's dynamics in a homodyne split detection scheme. For the x– and y–mode this consists in half-splitting the beam with a sharp edge D-shaped mirror (DM), respectively vertically and horizontally. The two halves are then focused on the two detectors of a balanced photoreceiver [8]. By doing so it is possible to measure the oscillating component of the intensity pattern perpendicular to the splitting direction. The resulting signal is then proportional to the particle's position while DC and slowly drifting components, being common in both channels, get highly suppressed. For the z–mode, instead the whole beam is sent to the detector and balanced with a reference beam picked up before the vacuum chamber. Figure 3.3 exemplifies the different geometries of the split detection scheme for the different axes. Compared to previous settings [34], recent updates of the set-up have led to an improvement in the detection efficiency. In Fig. 3.4 we report a characterization of the detected signal to noise ratio (SNR) as a function of the optical power of the probe beam P_{det}. This was done at a pressure of $P \sim 6$ mBar by recording the PSD $S_v^{(i=x,y,z)}$ of the three different modes (Fig. 3.4a exemplifies the case for the x–mode). The variable $v(t)$ represents the uncalibrated particle's position given as a digital signal (typically in bits units when the FPGA streams the data do the PC, occasionally in volts when an oscilloscope is used instead). The SNR was then calculated comparing the height of the resonance

[8] Balanced Optical Receiver, 900-1700 nm InGaAs Detector, 80 MHz, Free Space

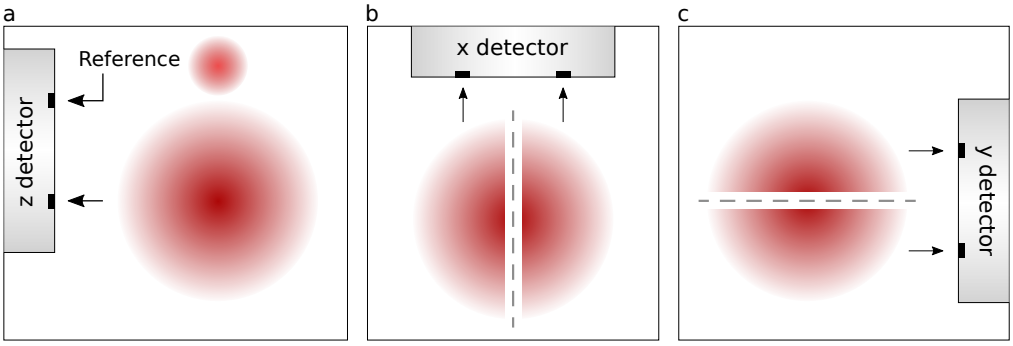

Figure 3.3: **Split detection scheme**. (a) To detect the z–mode the whole beam is focused on one port of the detector and balanced with a reference picked up from the detection beam before the vacuum chamber. For (b) x–mode and (c) y–mode, the beam is split with a D-shaped mirror and the two halves are sent to the two detectors of the respective balanced photoreceivers.

peak $S = S_v(\Omega_0)$ and the measurement noise floor $N = \langle S_v(\omega) \rangle$ estimated in the absence of trapped particle. As expected, the curves shown in Fig. 3.4b-d display an increase of the SNR as a function of P_{det}, reaching a plateau for $P_{\text{det}} \gtrsim 10$ mW. A final power of $P_{\text{det}} = 7.5$ mW was chosen as a convenient default setting for our experiments, with a corresponding signal being more than $40 - 50$ dB above the measurement noise. We stress that although the detection efficiency might to be a crucial parameter at these pressures, when the system is brought to high vacuum and the feedback is activated, the oscillation amplitude is reduced by several orders of magnitudes. In these conditions a higher SNR leads to higher cooling rates and therefore to lower center of mass effective temperatures T_{CM}.

3.3 Parametric feedback

For cooling the particle's Center of Mass (CoM) motion, the setup is provided with an active parametric feedback scheme [35]. The basic concept of the feedback is to introduce a modulation in time of the optical intensity $I(\mathbf{r})$ at the focus. Such a modulation is specifically built up using the information over the particle's position x and velocity $\dot{x}$ in order to create an effective stiffening ($k > k_0$) and softening ($k < k_0$) spring constant at a precise phase relation with respect to the particle's oscillation. Figure 3.5 provides a graphical representation of the working principle. The particle's oscillation is divided in four different sectors:

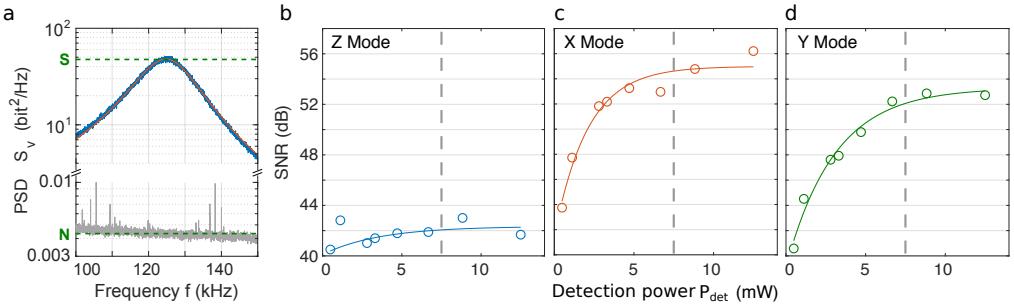

Figure 3.4: **Detection efficiency**. The dectection efficiency is charachterized as a function of the power of the probe beam P_{det}. (a) exemplifies how the SNR in the x–mode is calculated comparing the particle signal S at resonance with the measurement noise N in the absence of trapped particle. (b), (c), (d) represent the growth of SNR as a function of P_{det} for the z–, x– and y– mode respectively. The saturation of the detectors takes place at $P = 15$ mW. In our experiments we used $P_{\text{det}} \sim 7.5$ mW as a reasonable compromise in order to prevent the photoreceiver to saturate due to pointing instabilities in the optical path

I)	$x > 0,\ \dot{x} > 0$	*moving away from* x_{eq}	$(E_{\text{kin}} \rightarrow E_{\text{pot}})$	$\Rightarrow$	$\mathbf{k} > \mathbf{k_0}$
II)	$x > 0,\ \dot{x} < 0$	*falling back to* x_{eq}	$(E_{\text{pot}} \rightarrow E_{\text{kin}})$	$\Rightarrow$	$\mathbf{k} < \mathbf{k_0}$
III)	$x < 0,\ \dot{x} < 0$	*moving away from* x_{eq}	$(E_{\text{kin}} \rightarrow E_{\text{pot}})$	$\Rightarrow$	$\mathbf{k} > \mathbf{k_0}$
IV)	$x < 0,\ \dot{x} > 0$	*falling back to* x_{eq}	$(E_{\text{pot}} \rightarrow E_{\text{kin}})$	$\Rightarrow$	$\mathbf{k} < \mathbf{k_0}$

Intuitively, the table above tells us that the optical spring needs to be stiffened when particle is moving away from the equilibrium position x_0 and kinetic energy is being converted into potential energy. Viceversa, when the particle is falling back to equilibrium potential and potential energy gets converted into kinetic energy, the trap needs to be softened. Note that in the frequency domain this is equivalent to a modulation at twice the frequency of the particle oscillation.
As a result the feedback signal v_{FB} and consequently the parametric force applied to the particle are of the form:

$$v_{\text{FB}} \propto x\dot{x} \qquad , \qquad F_{\text{FB}} = m\Omega_0\eta x^2\dot{x} \ , \tag{3.1}$$

where we have introduced the parameter η, also called nonlinear damping coefficient, to model the feedback gain.

From an experimental point of view, the feedback signal is implemented with a modular electronic unit that consists of :

- Bandpass filter, to suppress low– and high–frequency noise components, respectively due to mechanical vibrations and to the $\Delta f = 110$ MHz beating between probe and trapping beam.

- Frequency doublers (one for each mode and optimized for the specific

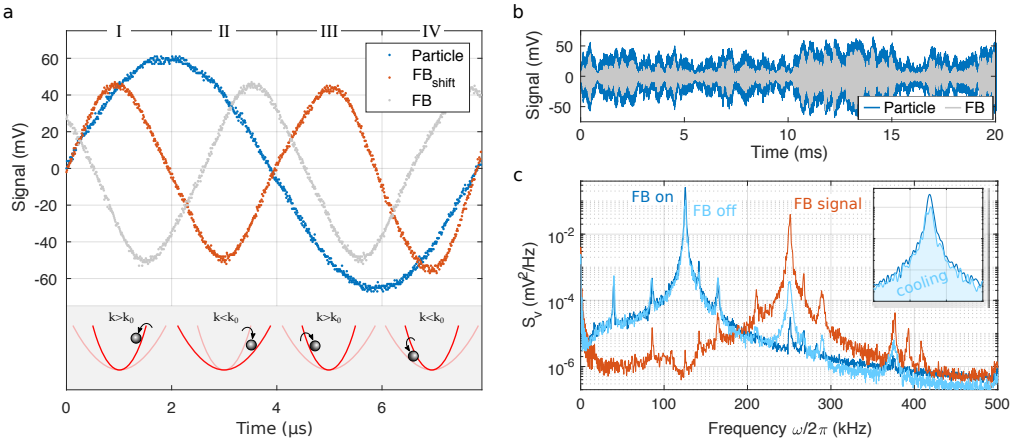

Figure 3.5: **Working principle of parametric feedback cooling**. (a) Real data showing the modulation of the trapping beam at twice the frequency of the particle's motion . A phase shift ϕ_{FB} in the feedback compensates electronics delays and ensures cooling (gray trace). In the orange curve we artificially set $\phi_{FB} = 0$ to exemplify the correct stiffening and softening of the potential. (b) Particle and feedback signal over longer time scales show the proportionality between the two.(c) PSD of the particle displacement along the x–mode (with and without feedback) and feedback signal at twice the particle's frequency. The inset show some minimal cooling (energy damped of a factor ~ 2) at a moderate pressure of $P = 1$ mBar.

frequency), to create the feedback signal v_{FB} at twice the frequency of the particle's oscillation $\Omega_0/2\pi$.

- Phase shifters (one for each mode), to ensure the correct phase of the modulation with respect to the particle's oscillation and consequently an efficient cooling of the CoM motion. We stress the crucial importance of this unit pointing out that a π shift in this phase converts cooling into parametric amplification.

- Adder and attenuator, to sum up the signals from the three channels corresponding to the three oscillation modes and to attenuate the output signal depending on the specific needs (mainly related with the different input signal amplitudes at different pressures). This module is also provided with a fourth input channel to add a parametric driving signal in the laser modulation.

Figure 3.6 shows a schematics of how the feedback modules are arranged. We use a Field Programmable Gate Array[9] (FPGA) as a analog-to-digital converter to process and store the data describing the particle's dynamics. The signal to

[9] National Instrument PCIe-7852R

provide the parametric driving, instead, is created with a waveform generator[10] (FG) and sent to the fourth input channel of the adder module. To ensure

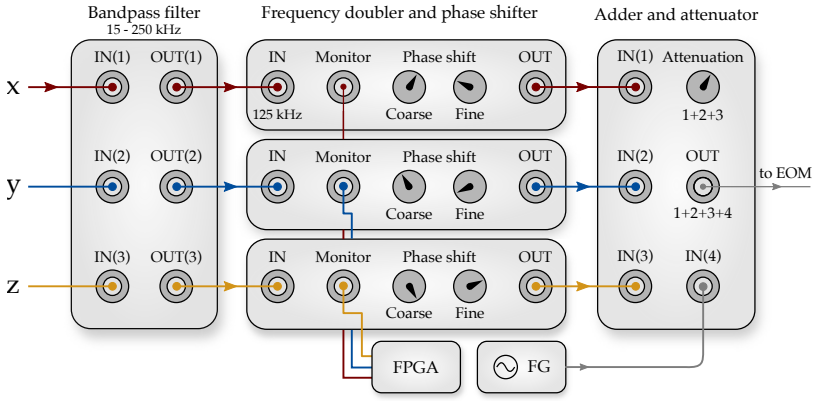

Figure 3.6: **Electronic feedback modules**. Schematics of how the signal from the x, y, and z detectors is processed by the feedback modules. In sequence we find bandpass filters, frequency doublers and phase shifters, adder and attenuator. The monitor signal is sent to an FPGA that records the particle's dynamics. The signal from the function generator (FG) is used to parametrically drive the particle.

its correct efficiency, parametric feedback is activated only after the particle's dynamics enters in the ballistic regime, i.e. when the oscillator performs the transition between the overdamped and the underdamped regime (see §2.2.1). To find the initial optimal settings of the feedback the mean energy $\langle \hat{E}^{(i)} \rangle$ of the particle along the three oscillation modes ($i = x, y, z$) is tracked while scanning the phase shifts $\phi_{FB}^{(i)}$. The instantaneous energy $\hat{E}^{(i)}$ is defined as

$$\hat{E}^{(i)} = \int_{\Omega_0^{(i)}-b}^{\Omega_0^{(i)}+b} S_v^{(i)}(\omega) \mathrm{d}\omega \tag{3.2}$$

and computed from a $\mathcal{T} \simeq 13$ ms time trace, where the integration bandwidth is tipically $b = 40$ kHz. From an ensemble of $N_{\mathrm{PSD}} = 1000$ realizations of $\hat{E}^{(i)}$ we estimate the mean energy $\langle \hat{E}^{(i)} \rangle$ and the standard deviation of the energy distribution $\sigma_{\hat{E}^{(i)}}$. Figure 3.7 shows the mean energy (normalized to its minimum to enable a direct comparison between the different modes), fitted with a quadratic function. We also show the extent of the energy distribution $\langle \hat{E}^{(i)} \rangle \pm \sigma_{\hat{E}^{(i)}}$. Clearly, optimal parameters can be found as minima in the trend of $\langle \hat{E}^{(i)} \rangle$, and manually set in the feedback electronics for efficient cooling operation. The different trend shown by the x–mode, compared to the other two, is due to both a higher feedback gain and a broader range of the phase shift.

[10] Agilent 33520A

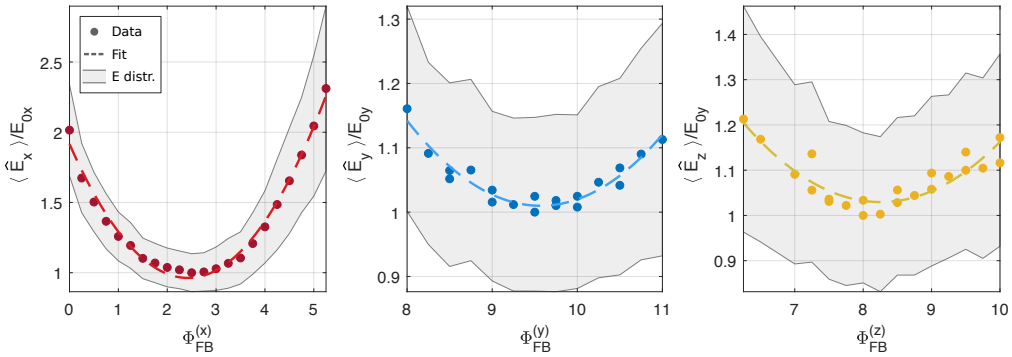

Figure 3.7: **Feedback optimization at high pressure**. Optimization of the phase shifts $\phi_{FB}^{(i)}$ at pressure $P \simeq 1$ mBar. From left to right we have $i = x, y, z$ respectively. The mean energy $\langle \hat{E}^{(i)} \rangle$ (normalized to its minimum E_{0i}) is shown as solid color circles. This is fit with a quadratic function that provides the optimal $\phi_{FB}^{(i)}$ at the vertex. Finally, the shaded area corresponds to the width (standard deviation $\sigma_{\hat{E}^{(i)}}$) of the energy distribution.

The initial optimization protocol, performed at moderate vaccum, can be followed by a finer tuning of the phase shifts $\phi_{FB}^{(i)}$ once high vacuum is reached. Such a readjustment is of utmost importance in case we want to operate the system in the nonlinear regime of oscillation, for example when parametrically driving the oscillator. In fact, under these conditions the particle's oscillation and consequently the feedback signal gets greatly amplified (up to factors of few tens) and the electronics has to operate in a different voltage regime. Moreover, when parametrically driving the resonator, the frequency gets downshifted (see nonlinear frequency shift in Eq. (2.93)), and the electronics could again have a different response to frequencies a few kHz lower then the ones used in the initial optimization. This further optimization of the phases $\phi_{FB}^{(i)}$ is based in the maximization of the nonlinear damping coefficients η_i introduced in (3.1), which is responsible for cooling the particle's motion. Some of the experimental procedures described in the following will be explained in more detail in § 6. The protocol consists in parametrically driving the particle in the first instability tongue (see §2.2.2) and recording the response of the oscillation as a function of normalized detuning δ_{m} and modulation depth ϵ. For each value of ϵ the amplitude $A(\delta_{\mathrm{m}}; \eta, \xi)$ is fitted by the corresponding analytical expression provided in Eq. (2.107) (note that for an easier notation we have here identified $A = q_0$). The nonlinear coefficients η and ξ are then extracted as free parameters in the fitting routine. Fig. 3.8a provides an example of the particle response in the first instability tongue., while 3.8b shows a cross cut for $\epsilon = 0.325$ and the corresponding amplitude fit in yellow dashed line. The final value of η for each specific value of $\phi_{FB}^{(i)}$

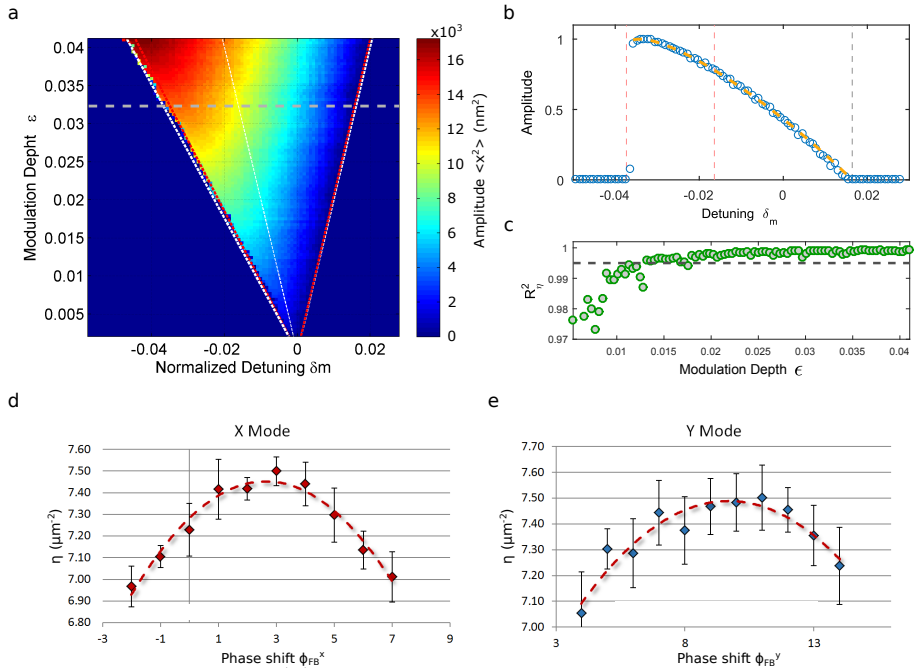

Figure 3.8: **Feedback optimization at low pressure**. (a) The particle is parametrically driven at the first instability tongue. The colormap shows the amplitude response along the x–mode in the parameter space (δ_m, ϵ). White and red dotted lines represent respectively the theoretical and experimentally fitted edge of the tongue, showing prefect agreement. The crosscut at $\epsilon = 0.325$ is shown in (b) and fitted with the analytical solution (2.107). (c) The confidence level R^2 of the fit is calculated for each value of ϵ. For $R^2 > 0.95$ we average the fitted coefficients η and obtain its mean value, which is shown in (d) and (e) as a function of the phase shifts $\phi_{FB}^{(i)}$. Here, only the results for the x– and y–mode are shown, though the z–mode displays a similar trend and the phases can be generally optimized.

is averaged over the fits that display confidence level higher that $R^2 = 0.95$. The process is repeated for every oscillation mode while sweeping the phase shifts $\phi_{FB}^{(i)}$. Finally, Fig. 3.8d shows the nonlinear damping coefficients $\eta_{(x,y,z)}$ as a function of the feedback phases. The trend clearly shows the presence of a maximum identifying the optimal values of the feedback phase settings.

3.4 Particle loading and clusterization

Particles[11] smaller than about 1 μm in diameter are loaded in the optical trap by spraying a solution of ethanol and particles inside the vacuum chamber.

[11] microParticles GmbH, SiO_2-R-0.15, SiO_2-R-0.25

We use a commercial nebulizer[12] that creates an aerosol of liquid droplets, about 5 μm in diameter. A droplet that crosses the trap with sufficiently low kinetic energy can effectively be attracted to the focus, conveying one or more nanoparticles in the optical trap depending on the concentration of the silica particles in the solution. Given that that the particles are provided by the manufacturer in a $wt5\%$ (weight percent) solution of distilled water, the average number of particles R per droplet of solution can be calculated as:

$$R = \frac{V}{V_e}\left(\frac{d_{drop}}{d}\right)^3 \frac{1}{1+19\rho_p/\rho_{dw}}\,, \tag{3.3}$$

with V and V_e being respectively particles and the ethanol volumes, d_{drop} and d_p the diameter of the aerosol droplets and of the nanoparticle, ρ_p and ρ_{dw} the density of bulk silica and of distilled water. In order to have $R \approx 1$, in our experiments we typically chose $V = 2.5\ \mu\ell$ and $V_e = 3\ m\ell$ for the $d_p = 143$ nm.

If a droplet of solution with multiple embedded silica nanoparticles falls into the optical trap, these form a cluster that can be nonetheless stably trapped and brought to vacuum. In most cases, this is a condition that needs to be avoided. In order to distinguish whether the object in the trap is a single nanoparticle or a cluster of multiple particles we observe its scattered intensity (or brightness B) with an imaging system placed below the vacuum chamber. The value of B is then compared with the typical range of values expected and previously characterized. This was done preparing a solution with $R \gtrsim 3$ and collecting the statistics of B from a sample of ~ 350 particles, $d_p = 143$ nm in diameter. Being the scattering intensity proportional to the sixth power of the object size, the exposure time t_{exp} of the CCD could not be maintained constant and had to be continuously readjusted to prevent saturation. We therefore introduce the normalized brightness:

$$B_{eff} = \frac{B - B_0}{t_{exp}}\,, \tag{3.4}$$

with B_0 being the background intensity with an empty trap. From the whole set of data we built the histogram shown in Fig. 3.9a. At first sight, this resembles a continuous distribution that extends over more than two orders of magnitude. This would clearly contradict the monodispersity of the particle solution. However, by zooming into the lowest intensity region (shaded area), one can easily recognize the presence of individual and well separated peaks corresponding to increasing integer number of particles in the trap. This specific result allowed to characterize the expected brightness from a single particle, as opposed to the multi–particle cluster case, therefore giving a reliable

[12] Omron MicroAir Nebulizer, NE-U22V

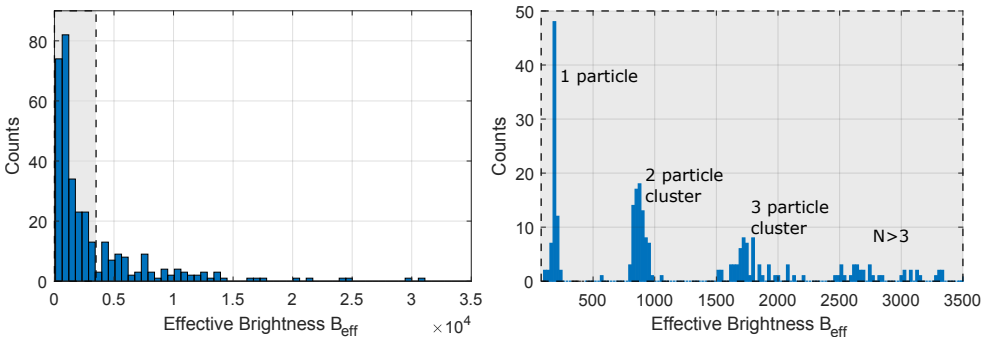

Figure 3.9: **Clusterization of $d_p = 143$ nm particles.**(a) Histogram of the effective brightness from a sample of ~ 350 particles. The shaded region indicates where the scattering from a single particle would be expected. (b) Zooming in the low brightness region, the histogram exhibits individual well separated peaks corresponding to single particles.

selective method for discarding clusters before going to vacuum and performing the specific experiments. A similar characterization was repeated for the $d_p = 235$ nm particles, showing in this case less tendency to form clusters.

3.5 Electric driving

In order to implement a direct actuation scheme, complementary to the parametric control generated via laser intensity modulation, the original setup described in § 3.2 and § 3.3 was provided with a pair of electrodes mounted inside the vacuum chamber. These generate an electric field that couples to the charged particle by means of Lorentz interaction ($\mathbf{F} = q\mathbf{E}$). Different electrodes geometries were tested, eventually finding better performances using small electrodes that could be fit right at the sides of the optical trap, therefore providing a more homogeneous field. A picture of the updated setup icluding the final design of the electrical actuation scheme is shown in Fig. 3.10. The electrodes are made of tempered steel, they have a diameter of $\phi = 1.000 \pm 0.003$ mm, an axial separation of $d_{el} = 1.410 \pm 0.013$ mm and are hold by a teflon support at a distance $\Delta z_{obj} = 0.43$ mm from the objective surface. In § 4.3.4 we will provide further details on the electrodes geometries and how these have been estimated. To generate the electric field and exert a force on the charged particle we connect one of the two electrodes to a function generator[13], while the other one is directly grounded via the vacuum chamber. Figure 3.11a shows the resonant response of a particle charged with

[13] Agilent 3320A Function/Arbitrary Waveform Generator.

$n_q = 8$ elementary charges to a $V_{\mathrm{dr}} = 18.4$ Vpp sinusoidal electrical driving at a frequency of $\omega_{\mathrm{dr}}/2\pi = 130$ kHz, superimposed to the thermal motion of the resonator (check §2.2.1 for analytical prediction).

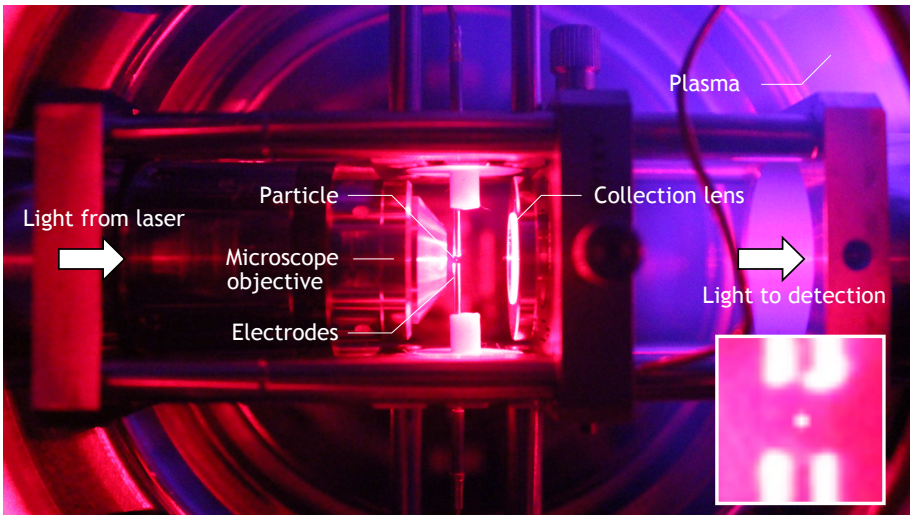

Figure 3.10: **Experiemental set-up inside of the vacuum chamber**. A pair of electrodes placed around the trap focus form an ideal parallel plate capacitor used to generate an electrical field that couples to the particle via Lorentz interaction.

Charge control method

The particles loaded in the optical trap with the nebulization method usually show a non-null initial net charge n_q^{in} of the order of ten elementary charges. In § 5.2.4 we build up considerable statistics on the value of n_q^{in}. Data shows a $70-30$ biased polarity distribution toward positive charges. Consequently these particles can already couple to the electric field from the electrodes. However, higher flexibility on the particle's polarity and on the number of charges n_q to be used in the experiments is desirable. Moreover, this initial charge is not known a priori and an experimental method to measure the particle's charge is paramount for quantitative analysis of the electrically driven dynamics. To address these issues, we developed an experimental technique to control the net charge of the levitated particles. Similarly to what has been shown in [29], this method consists in applying a high voltage to a bare electrode situated on a side of the vacuum chamber, few centimeters away from the optical trap (see Fig. 4.2 for set-up schematics). In a moderate vacuum of $P \sim 1$ mbar, the high voltage creates a plasma via the process of corona discharge [28]. In a nutshell, if a neutral air molecule is ionized by a natural environmental event (for example after being struck by an ultraviolet photon,

or a cosmic ray) the formed electron and positive ion get accelerated toward different directions due to the presence of the high voltage which in turn prevents them to recombine. Given the small mass of the electron, this latter acquires enough kinetic energy to ionize other molecules and form an electron avalanche. The violet glow of the corona (clarly visible in the top-right corner of Fig. 3.10) is indeed caused by electrons recombining with positive ions and emitting (mainly) UV photons. Coronæ can be classified into positive and negative coronæ, depending on the polarity of the high voltage applied to the electrode. These lead to very different phenomena and are indeed used in science and engineering for different purposes. Without entering too much into the details of these processes, it is sufficient to know that by creating either a positive or a negative corona one can bias the ratio of positive-to-negative ionized molecules that are accelerated toward the center of the chamber where the optical trap is situated. Ultimately, these can be adsorbed on the particle surface and change its net charge almost monotonically (exception made for few random unfavorable events) from positive to negative and viceversa, depending on the polarity chosen. Disconnecting the high voltage stops the corona discharge and the number of charges on the particle is maintained stable indefinitely.

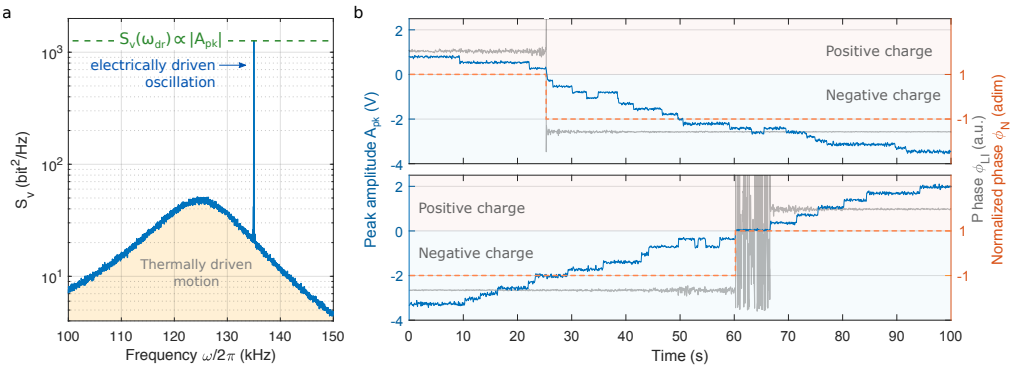

Figure 3.11: **Net charge control.** (a) Power spectral density of a thermally and electrically driven particle at a pressure $P \simeq 50$ mBar (corresponding to a linewidth $\Gamma/2\pi \simeq 30$ kHz). The height of the electrically driven peak $S_v(\omega_{\rm dr})$ depends quadratically on the number of charges $|n_q|$. (b) In order to monitor the value of $|n_q|$ while the corona discharge is active, the amplitude $A_{\rm pk}$ and phase $\phi_{\rm LI}$ are tracked in time. The discrete steps observed in $A_{\rm pk}$ identify single elementary charges being added or removed from the particle.

To monitor changes in the particle's net charge while the corona is active we look for integer steps in the height of the peak $S_v(\omega_{\rm dr})$ represented in Fig. 3.11a. For this task we make use a lock-in amplifier (check Fig. 4.2 for a sketch of the setup configuration). The lock-in is synchronized with the

function generator that drives the particle at frequency $\omega_{\mathrm{dr}}/2\pi$. As such it provides the amplitude A_{LI} and phase ϕ_{LI} of the driven oscillation, measured in a narrow band around ω_{dr}. It is important to stress that the lock-in only provides positive amplitudes, therefore making it impossible to discern the particle's polarity. In other words, the detected peak $S_v(\omega_{\mathrm{dr}})$ takes the same value for both $\pm n_q$ and assumes the value of the thermal noise floor $S_v^{\mathrm{th}}(\omega_{\mathrm{dr}})$ when $n_q = 0$. However, attraction/repulsion of Lorentz force is such that the particle's oscillation results in phase with the external driving if its polarity is positive, out of phase if this is negative and possesses an undefined phase if the particle is neutral. We can therefore introduce a normalized phase ϕ_{N} of the form:

$$\begin{cases} \phi_{\mathrm{N}} = 1, & \text{if } \phi_{\mathrm{LI}} > 0 \\ \phi_{\mathrm{N}} = 1, & \text{if } \phi_{\mathrm{LI}} \text{ is undefined} \\ \phi_{\mathrm{N}} = -1, & \text{if } \phi_{\mathrm{LI}} < 0\,, \end{cases} \tag{3.5}$$

such that the signed amplitude $A_{\mathrm{pk}} = A_{\mathrm{LI}} \cdot \phi_{\mathrm{N}}$ is now directly proportional to the charge (polarity included) of the particle. Figure 3.11b,c show A_{pk} (blue data), ϕ_{LI} (gray data) and ϕ_{N} (orange data) respectively for a discharging and charging process in the range $n_q \in [-16, 6]$. Discrete steps in A_{pk} can indeed be observed, proving the reliability of our method of controlling the net charge down to the single elementary charge resolution.

4

Accurate measurement of the particle's mass

Contents

4.1 Introduction

Owing to their high sensitivity, nanomechanical resonators are widely applied as both mass and force transducers. In the former case, typical operation schemes rely on measuring the shift of the resonance frequency due to a change in the mass of the resonator [17] (for example due to adsorption of a single molecule on its surface). In the latter, instead, forces are detected ob-

serving specific dynamical features in the oscillation and making use of the transfer function of the resonator to estimate the magnitude of the applied force [75]. In both cases, the information over the inertial mass of the resonator is indispensable for providing quantitative analysis of the results, and its uncertainty directly affects the accuracy of the measurement.

Although different classes of nanomechanical systems have reached state-of-the-art yocto-gram and zepto-newton sensitivities (including levitated nanoparticles in the latter case), clamped resonators still suffer from high uncertainty on their mass determination that severely impact their sensing accuracy. The main reason for such high uncertainties is mainly the impossibility of applying the rigid body approximation. This leads to consider an effective mass, different from the inertial mass, whose calculation requires precise assessment of the system's geometry, knowledge on material properties and complex flexural models to to include the shape of the fundamental oscillation mode and its higher harmonics.

In this context, levitated nanoparticles offer two great advantages. On the one hand, the rigid body approximation is largely fulfilled: the silica nanoparticle can be considered just as a bulk sphere, whose inertial mass is unambiguously defined. On the other hand, the isolation of the system provides force calibration strategies that are not affected by clamping losses. For instance, the possibility of preserving a well defined net charge enables controlled coupling to the system via Coulomb and/or Lorentz interaction, as explained in §3.5. It is clear, then, that while levitated systems share the lead with other types of nanomechanical resonators in terms of sensitivity, they could in principle provide unbeatable performances in sensing and metrology applications, where the accuracy of a measurement is just as important as its precision.

Standard approaches in levitodynamics calculate the particle's mass directly from the manufacturer specifications, or in some cases applying the kinetic gas theory. However, both provide a rather inaccurate measurement due the poor knowledge over quantities like mass density, particle's size, gas pressure and its molar mass. The resulting mass uncertainties are as high as $20-30\%$, with negative effects on the sensing performances.

In this chapter we propose and demonstrate a measurement protocol that is unaffected by the uncertainties mentioned above (density, pressure, size, etc...), and is able to calculate the particle's mass with statistical error below 1% and a systematic error of $\sim 2\%$. Our method exploits the new design of the optical trap presented in § 3.5, and is based on the analysis of the response of a charged particle in a harmonic trap to an external electric field. The study includes a careful error estimation in § 4.3.4 and § 4.3.5 to deter-

mine the ultimate mass uncertainty, together with the treatment of possible anharmonicities in the trapping potential.

4.2 Review of common measurement methods

In the following sections we briefly review the principal methods used for the estimation of the particle's mass. We first verify the manufacturer's specifications of particle size, and give en estimation of the resulting mass uncertainty. Then we report a second method to estimate the particle's mass from kinetic gas theory, and similarly perform error propagation to evaluate the associated error.

4.2.1 Manufacturer's size characterization

The specific type of nanoparticles used are monodispersed silica spheres (SiO_2) that come in a water solution (particle content $wt.5\%$ in mass), with manufacturer specifications reporting a coefficient of variation $\mathrm{CV} = \sigma_d/\langle d \rangle$ between 2% and 5%, d and σ_d being respectively the mean particle's diameter and its standard deviation. We performed an independent characterization of the particle's size by measuring the diameter of a sample of ~ 120 particles in a Scanning Electron Microscope (SEM). The results are given in Fig. 4.1 for the batch SiO2-R-L1914 and show a slightly higher σ_d compared to the manufacturer specifications. More precisely we measure $d = 232 \pm 16$ nm, instead of $d_{\mathrm{man}} = 235 \pm 10$ nm. However, the main source of error in this technique is the uncertainty on the mass density of amorphous silica. This quantity is given by the manufacturer as $\rho_{\mathrm{p}} = 1850\ \mathrm{g/cm^3}$ and no accuracy of this value is provided. Nonetheless, an extensive search in material science literature [31, 59, 81, 114] revealed significant variations of the nominal density, that ultimately depends on the fabrication process and can also largely vary depending on their water content (more details on this issue are provided in § 5). Moreover, particles are often exposed to washing and drying protocols [81] before the density is measured, therefore introducing an intrinsic incompatibility between literature or manufacturer specifications and the actual properties of the particles we optically trap. As a result, the mass density can be assumed only with an associated uncertainty of $(\sigma_{\rho_{\mathrm{p}}}/\rho_{\mathrm{p}}) \gtrsim 10\%$. Propagating the two known uncertainties in $m = \pi/6\rho d^3$, we have:

$$\frac{\sigma_m}{m} = \sqrt{9\left(\frac{\sigma_d}{d}\right)^2 + \left(\frac{\sigma_{\rho_{\mathrm{p}}}}{\rho_{\mathrm{p}}}\right)^2} \sim 25\% \tag{4.1}$$

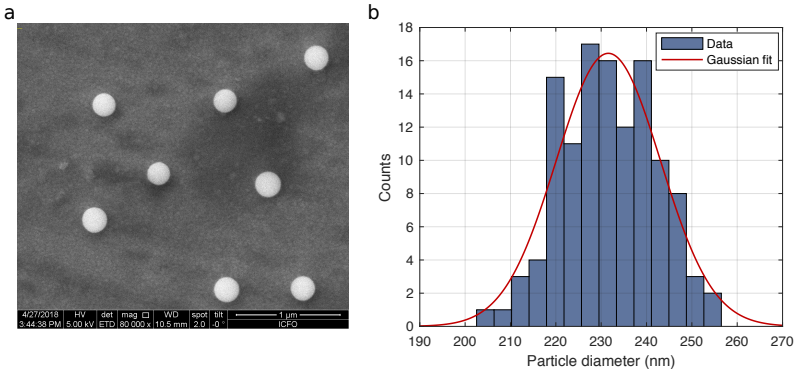

Figure 4.1: **Particle size characterization**. (a) SEM image of few nanoparticles deposited on a conductive glass substrate. The sample was prepared spraying on the conductive coverslip the exact same solution we use for trapping. (b) Statistics of the particles' diameter measured fitting a circle on the particle edges. We measure $d = 232 \pm 16$ nm.

4.2.2 Mass from kinetic theory of gases

To avoid relying on the manufacturer specifications, one could retrieve the particle's mass from observations of its dynamics [35], and more precisely making use of the kinetic theory of gases [10, 34]. This theory allows to relate the measured damping rate Γ, which in the harmonic approximation only depends on the gas pressure, to the particle's size. Its definition reads [34] :

$$\Gamma = \frac{6\pi\eta_{\text{air}} r_{\text{p}}}{m} \frac{0.619}{0.619 + \text{Kn}} (1 + c_K) \approx \frac{6\pi\eta r}{m} \frac{0.619}{\text{Kn}} , \tag{4.2}$$

with $\eta_{\text{air}} = 18.27 \times 10^{-6}$ Pa $\cdot$ s being the viscosity coefficient of air [42] and r_{p} the radius of the particle. $\text{Kn} = \ell/r$ is the *Knudsen number* which is defined as the ratio between the mean free path ℓ of the air molecules and the size of the particle. In practice $\text{Kn} \sim 1$ at ambient pressure, but becomes $\text{Kn} \gg 1$ in vacuum, which justifies the right-hand approximation in (4.2). Finally, $c_k = 0.31\text{Kn}/(0.785 + 1.152\text{Kn} + \text{Kn}^2)$. From the mean free path, which reads

$$\ell = \frac{\eta_{\text{air}}}{P_{gas}} \sqrt{\frac{\pi N_A k_B T}{2M}} , \tag{4.3}$$

with $M = 28.97 \times 10^{-3}$ kg/mol being the molar mass of dry air and N_A the Avogadro's number, we can retrieve particle's radius and mass as:

$$r = \frac{2.223}{\rho_{\text{p}}} \sqrt{\frac{M}{N_A k_B T}} \frac{P_{\text{gas}}}{\Gamma} \tag{4.4}$$

$$m = \frac{0.208}{\rho_{\text{p}}^2} \left(\frac{M}{N_A k_B T} \right)^{3/2} \frac{P_{\text{gas}}^3}{\Gamma^3} . \tag{4.5}$$

Error propagation on eq. (4.5) gives:

$$\frac{\sigma_m}{m} = \sqrt{\left(2\frac{\sigma_{\rho_\mathrm{p}}}{\rho_\mathrm{p}}\right)^2 + \left(\frac{3}{2}\frac{\sigma_M}{M}\right)^2 + \left(\frac{3}{2}\frac{\sigma_T}{T}\right)^2 + \left(3\frac{\sigma_{P_\mathrm{gas}}}{P_\mathrm{gas}}\right)^2 + \left(3\frac{\sigma_\Gamma}{\Gamma}\right)^2} \sim 35\% \,, \tag{4.6}$$

where for the molar mass we rely on measurements performed on a similar vacuum set-up [43] that provided an accuracy of $\pm 5\%$. The pressure's accuracy is given by the specifications of the gauge and reads $(\sigma_{P_\mathrm{gas}}/P_\mathrm{gas}) \sim \pm 10\%$. Finally, temperature and damping errors are detailed more carefully in §4.3.4 and are respectively on the order of $\sim 0.2\%$ and $\sim 0.3\%$.

It is clear from what has been shown in this section that the available methods to estimate the particle's mass provide very inaccurate results. On the one hand, this prevents a proper displacement calibration of the particle, which has crucial role in any sensing experiment. We conclude that a new and more reliable method for mass estimation would be paramount for precision experiments with levitated nanoparticles.

4.3 Mass from harmonically driven thermal states

In this section we describe and demonstrate a method for measuring the mass of the levitated nanoparticle that relies on the analysis of the particle's response to an external electric field. The experiment is carried out at a moderate vacuum, corresponding to pressures of $P \sim 50$ mBar. Under these conditions the parametric feedback is not yet activated. Moreover, the dynamics of the particle is tracked along one single oscillation mode, and the experimental set-up can be therefore described as a simplified version of the one presented in § 3.2.

4.3.1 Experimental configuration

Figure 4.2 depicts the experimental configuration. Along the x-mode axis a pair of electrodes form an ideal parallel plate capacitor that we use to generate an oscillating electric field $\mathbf{E}(t) = E_0 \cos(\omega_\mathrm{dr} t)\hat{x}$, which in turn induces a harmonic force $F_\mathrm{el}(t)\hat{x}$ on the charged particle.

The system dynamics is described by a thermally and harmonically driven damped resonator, with corresponding equation of motion:

$$m\ddot{x} + m\Gamma\dot{x} + kx = F_\mathrm{th}(t) + F_\mathrm{el}(t) \,. \tag{4.7}$$

Here, $k = m\Omega_0^2$ is the stiffness of the optical trap, with Ω_0 being the mechanical eigenfrequency of the oscillator. The first forcing term F_th models the random

collisions with residual air molecules in the chamber. It can be expressed as $F_{\text{th}} = \sigma\eta(t)$, where η is a white Gaussian noise process, and σ relates to the damping via the fluctuation-dissipation theorem: $\sigma = \sqrt{2k_B T m\Gamma}$, k_B being the Boltzmann constant and T the temperature of the residual gas in the chamber. The second forcing term F_{el} arises from the Lorentz interaction of the charged particle with the external electric field $\mathbf{E}(t)$, and can be expressed as $F_{\text{el}}(t) = F_0 \cos(\omega_{\text{dr}} t)$, where $F_0 = q \cdot E_0$. The charge $q = n_q \cdot q_e$, where q_e is the elementary charge and n_q the number of charges on the particle, can be finely controlled [29] as described in § 3.5.

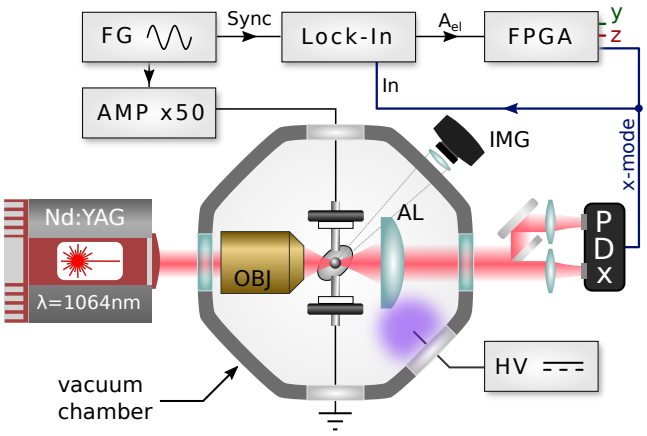

Figure 4.2: **Experimental configuration** (**a**) A microscope objective (OBJ) focuses a laser beam inside a vacuum chamber, where a single nanoparticle is trapped in the focus. The light scattered by the particle is collected with an aspheric lens (AL) and the motion of the particle is detected with a split detection scheme. Imaging (IMG) of the particle is performed from the bottom of the vacuum chamber with a CMOS camera. A pair of electrodes are connected to the amplified signal from a function generator (FG), creating an electric field that drives the charged particle. An FPGA and a lock-in amplifier are used to bandpass and record the signal from the detector. A high voltage applied at one side of the chamber creates a little plasma that is used to control the particle's net charge (see § 3.5).

4.3.2 Measurement protocol

We load a single nanoparticle at ambient pressure by nebulizing a solution of ethanol and silica particles into the chamber. The pressure is then decreased down to $P \lesssim 1$ mBar where the net number of charges n_q can be optimally set with zero uncertainty (see 3.5). Finally, the vacuum chamber is vented with nitrogen, and the system is brought back up to an operating pressure of $P \simeq 50$ mBar. Here the particle has already entered the ballistic regime but its dynamics is still highly damped. This condition is favorable for our experi-

ments since the high damping reduces the amplitude of oscillation, and hence the contribution of anharmonicities to the dynamics of the particle [36]. This allows us to apply the fully linear (harmonic) oscillator model. The analytical expression of the power spectral density (PSD) for this model was derived in § 2.2.1. We report it here for completeness:

$$\begin{aligned} S_x(\omega) &= S_x^{\mathrm{th}}(\omega) + S_x^{\mathrm{el}}(\omega) \\ &= \frac{4\, k_{\mathrm{B}} T\, \Gamma}{m\left[\left(\omega^2 - \Omega_0^2\right)^2 + \Gamma^2\omega^2\right]} + \frac{F_0^2\, \tau\, \mathrm{sinc}[(\omega - \omega_{\mathrm{dr}})\tau]}{m^2\left[\left(\omega^2 - \Omega_0^2\right)^2 + \Gamma^2\omega^2\right]} \,. \end{aligned} \tag{4.8}$$

More precisely, $S_x(\omega)$ is the single-sided PSD of the thermally and harmonically driven resonator, whose dynamics $x(t)$ is being observed for a time $\mathcal{T} = 2\tau$ Note that $S_x(\omega)$ relates to the experimentally measured PSD $S_v(\omega)$ via the calibration factor c_{cal}, such that $S_v(\omega) = c_{\mathrm{cal}}^2 \cdot S_x(\omega)$. The determination of c_{cal} is provided in A. In the absence of electric driving, the motion of the particle is purely thermal and its PSD is well approximated by an ordinary Lorentzian function.

From an experimental measurement of $S_v^{\mathrm{th}}(\omega)$ we extract the value of $S_v^{\mathrm{th}}(\omega_{\mathrm{dr}})$ and perform maximum likelihood estimation (MLE) to obtain the values of Ω_0 and Γ as fitting parameters. Likewise, when the harmonic driving is applied to the system, we determine the height of the driven resonance $S_v(\omega_{\mathrm{dr}})$, and from this we calculate electric contribution $S_v^{\mathrm{el}}(\omega_{\mathrm{dr}}) = S_v(\omega_{\mathrm{dr}}) - S_v^{\mathrm{th}}(\omega_{\mathrm{dr}})$. Figure 4.3 exemplifies this process for an arbitrarily chosen $\omega_{\mathrm{dr}}/(2\pi) = 135$ kHz and for a signal-to-noise SNR $= S_v(\omega_{\mathrm{dr}})/S_v^{\mathrm{th}}(\omega_{\mathrm{dr}}) \simeq 60$. The curve shown is computed with Bartlett's method from an ensemble of $N_{\mathrm{psd}} = 1000$ averages of individual PSDs, calculated from $\tau = 40$ ms position time traces. In § 4.3.4 (paragraph *Power Spectral Density*) we verify that over the whole measurement time $t = N_{\mathrm{psd}} \times \tau = 40$ s the system does not suffer from low frequency drifts. The electrically driven peak can be fully resolved (see inset in Fig. 4.3), and its shape agrees with the Fourier transform of the rectangular window function used for PSD estimation. The gray data points at the bottom of the plot represents the measurement noise, which is ~ 40 db below the thermal signal and more than ~ 55 db below the driven peak. Finally, the solid line is a MLE fit of a thermally driven Lorentzian to the experimental data. Note that, in order to perform the fit and to retrieve the value of $S_v^{\mathrm{th}}(\omega_{\mathrm{dr}})$, the electrically driven peak is numerically filtered out by applying to the time series a notch filter of variable bandwidth b around ω_{dr}. The value of b depends on the height of the peak, with typical values of the order of tens of Hz. We computationally verified that this method does not affect the estimated fitting parameters Ω_0, Γ and the thermal contribution

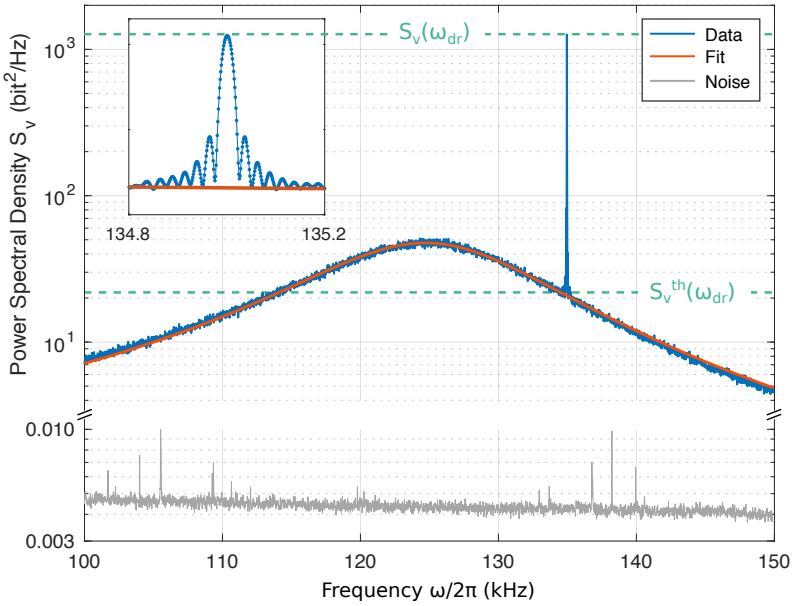

Figure 4.3: **Measurement.** Power spectral density $S_v(\omega)$ of a thermally and harmonically driven resonator at $P = 50$ mBar. The broad peak centered at $\Omega_0/2\pi \simeq 125$ kHz corresponds to the thermally driven state. We fit it with a Lorentzian function (orange) to extract $S_v^{\rm th}(\omega_{\rm dr})$, together with Ω_0, $\Gamma/2\pi = 31.8$ kHz and the corresponding uncertainties. The narrowband peak at $\omega = 135$ kHz, also shown in detail in the inset, depicts the electrical excitation from which we retrieve $S_v^{\rm el}(\omega_{\rm dr}) = S_v(\omega_{\rm dr}) - S_v^{\rm th}(\omega_{\rm dr})$. Gray data points at the bottom of the plot is the measurement noise, which is $\gtrsim 40$ dB below the particle's signal.

$S_v^{\rm th}(\omega_{\rm dr})$, introducing negligible errors that remain well below ~ 0.01 %.

The mass of the particle can ultimately be calculated considering the ratio

$$R_S = \frac{S_v^{\rm el}(\omega_{\rm dr})}{S_v^{\rm th}(\omega_{\rm dr})} = \left.\frac{S_v - S_v^{\rm th}}{S_v^{\rm th}}\right|_{\omega=\omega_{\rm dr}} . \tag{4.9}$$

In fact, note that while both $S_v^{\rm el}$ and $S_v^{\rm th}$ depend quadratically on $c_{\rm cal}$, the latter scales as m^{-1} while the former scales as m^{-2}. Thus, from their ratio we obtain:

$$\boxed{m = \frac{n_q^2\, q_e^2\, E_0^2\, \tau}{8\, k_{\rm B} T\, \Gamma\, R_S}} . \tag{4.10}$$

4.3.3 Results

The suggested protocol for the mass measurement is tested on particles of different size: $d_{\rm p} = 143$ nm and $d_{\rm p} = 235$ nm. In both cases we measure mass mean values $\langle m \rangle$ in agreement with the ones predicted by the manufacturer's

specifications and kinetic gas theory (both methods described in § 4.2), and a reduction of the associated uncertainty of more than one order of magnitude (see § 4.3.4 and § 4.3.5 for comprehensive treatment of the errors). We report in the following the results relative to the $d_{\mathrm{p}} = 143$ nm case.

Figure 4.4a shows a reproducibility measurement, performed to estimate the statistical error of our method. From a sample of 20 independent measurements we find $\sigma_m^{\mathrm{stat}} \simeq 0.7\%$. To validate the generality of our method, the mass is also measured at different driving parameters, as shown in Fig. 4.4b. The linear model ensures independence of the measured mass from the driving frequency ω_{dr}. We indeed find compatibility between the statistical error σ_m^{stat} and the standard deviation of the experimental measurements σ_m, shown in Fig. 4.4b respectively as error bars and green dash-dotted line. The mismatch in the measured mean value $\langle m \rangle$ with respect to Fig. 4.4a is due to slightly different experimental conditions (most probably a temperature change that was not take into account when computing the mass). Figure 4.4c presents the response of the system to the external excitation when the driving frequency is swept in the range $\omega_{\mathrm{dr}} \in [115, 135]$ kHz in steps of 1 kHz. For the main figure a driving voltage of $V_{\mathrm{dr}} = 13.7$ V was used, resulting in an electric field amplitude $E_0 = 4.0$ kV/m. For such amplitudes the particle is still driven in the linear regime. However, for higher driving the dynamics becomes nonlinear and the analytical model used to calculate the mass does not hold anymore. The presence of nonlinearities for higher driving amplitudes is exemplified in the insets of Fig. 4.4c, where second harmonic oscillatory components are detected only for $E_0 \gtrapprox 6$ kV/m. Finally, Fig. 4.4d presents again traits of nonlinear behavior for high field amplitudes. Blue data corresponds to the mass measured with the resonator in the linear regime (driven by a field amplitude $E_0 = 4.8$ kV/m), while red data correspond to the mass measured in the anharmonic case (with driving amplitude $E_0 = 21.2$ kV/m). The use of the linear model to fit a Duffing resonator clearly introduces appreciable systematic errors in the analysis, and the measured mass for high amplitudes carries an *unphysical* dependency on the driving frequency. As a result, we avoid this situation maintaining the driving field amplitude below 5.5 kV/m throughout all our measurements.

4.3.4 Uncertainties

In order to estimate the overall mass uncertainty, a careful study of all the sources of error needs to be carried out. Table 4.1 summarizes the absolute values and the relative uncertainties of the quantities entering in eq. (4.10).

For several variables and constants, we can neglect the corresponding un-

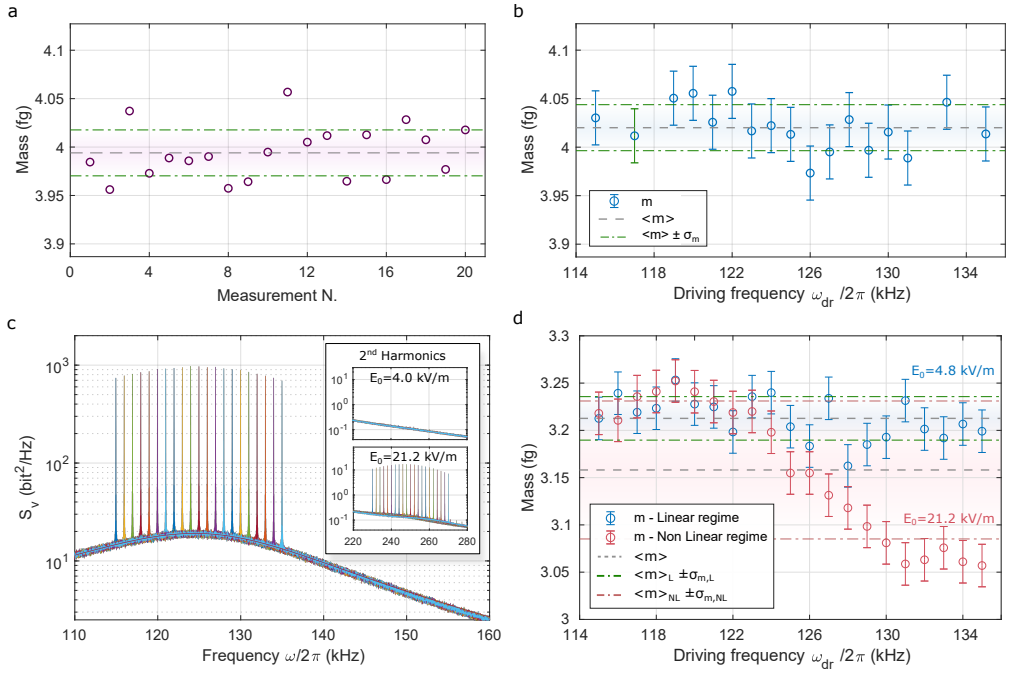

Figure 4.4: **Mass measurement results**. (a) A reproducibility measurement is performed to determine the experimental random error of our protocol. We find $\sigma_m/m \sim 7 \times 10^{-3}$, in agreement with the expected statistical error $\sigma_m^{\text{stat}}/m \sim 9 \times 10^{-3}$. (b) The mass measurement is performed at different driving frequencies in order to verify the compatibility with the linear approximation. The resulting dispersion of data-points σ_m^{sweep}, displayed as a green dot-dashed lines, is compatible with the error bars representing the statistical error from panel (a). (c) An example of the driving frequency swept in the range $\omega_{\text{dr}} \in [115, 135]$ kHz. Nonlinear features such as second harmonic oscillations are detected when the resonator is driven in the nonlinear regime. (d) Mass measurement datasets for different driving amplitudes. Blue data correspond to a harmonic oscillator, where no dependency on the driving frequency is observed. Red data, instead, is measured with the resonator driven into the nonlinear regime. In this case the measurement exhibits systematic artefacts depending on the driving frequency and a constant shift in the mean value $\langle m \rangle$.

certainty. Accordingly, for the error propagation we set: $\sigma_{q_e} = \sigma_\tau = \sigma_{k_B} = 0$. Concerning the other quantities, we follow the arguments stated below.

Electric field The absolute value and the corresponding uncertainty on the electric field E_0 have a high impact on the measurement of the mass (we see indeed from Table 4.1, that the electric field provides the largest relative error in our set of variables).We estimated the magnitude of the electric field with finite element simulations (COMSOL). The geometry of the system was inferred from a high resolution image of the electrodes (see Fig. 4.5a), obtained *in situ* with a portable microscope (adjustable magnification $40 \times -1000\times$).

Quantity	Value z_i	Error σ_{z_i}/z_i
n_q	8	0
q_e	1.602×10^{-19} C	6.1×10^{-9}
E_0	5.305 kVm^{-1}	0.011
$\mathcal{T}$	40 ms	4×10^{-5}
$S_v(\omega_{\mathrm{dr}})$	1057.8 bit^{2}Hz^{-1}	0.005
$S_v^{\mathrm{th}}(\omega_{\mathrm{dr}})$	14.7	0.007
k_{B}	1.380×10^{-23} JK^{-1}	5.72×10^{-7}
T	295.8 K	0.002
Γ	1.998×10^5 rads^{-1}	0.003
m	**4.01 fg**	**0.009** (stat.) $\pm$ **0.024** (syst.)

Table 4.1: **Uncertainties table.** The different quantities z_i involved in the calculation of the mass are here reported together with the corresponding error σ_{z_i}. Color coding indicates negligibility of the uncertainty, with gray rows implying $\sigma_{z_i} \simeq 0$. Last row summarizes the result of the mass calculation and the relative uncertainty for the red highlighted point in Fig. 4.4.

The maximum achievable resolution was limited by the actual fitting of the microscope inside the vacuum chamber, and by the field of view of the microscope that needed to include both electrodes in the same image. The factor $c_{\mathrm{img}} = 4.64 \pm 0.04$ μm/px, used to calibrate pixels into physical distance units, is calculated comparing the size of the electrodes with their nominal diameter: $\phi = 1$ mm, ISO h6 tolerance corresponding to $\sigma_\phi = 3$ μm. The uncertainty on the distance d_{el} separating the two electrodes is derived from the uncertainty on each electrode's edge position. We crop a 20×20 px^2 area at the edge of one of the electrodes, close to its center (see grayscale map in Fig. 4.5b). Averaging along the z axis, provides the experimental profile $I(x)$ of the electrode (red crosses). A *sigmoid* function of the form

$$\Sigma(x) = a_{\mathrm{high}} - \frac{a_{\mathrm{high}} - a_{\mathrm{low}}}{1 + e^{-(x-x_0)/\tau}} \tag{4.11}$$

is used to fit the profile, the result being displayed as a green solid line in Fig. 4.5b. The fitting parameters a_{high}, a_{low} x_0, τ, representing respectively the high/low plateau level, the center of the edge and its width, are used to calculate the separation w between 1/10 and 9/10 of the step height (dashed purple vertical lines). The error over the position of the single electrode edge is then $\sigma_p = w/2 = 1.14$ px, and the error over the electrodes distance $\sigma_{\Delta p} = \sqrt{2}\sigma_p$. Using c_{img} to calibrate into physical units and to propagate with the corresponding error $\sigma_{c_{\mathrm{img}}}$, we finally obtain $d_{\mathrm{el}} = 1411 \pm 13$ μm. The mapped geometry of the electrodes, together with their distance from the objective and from the collection lens are plugged into a COMSOL finite element simulation

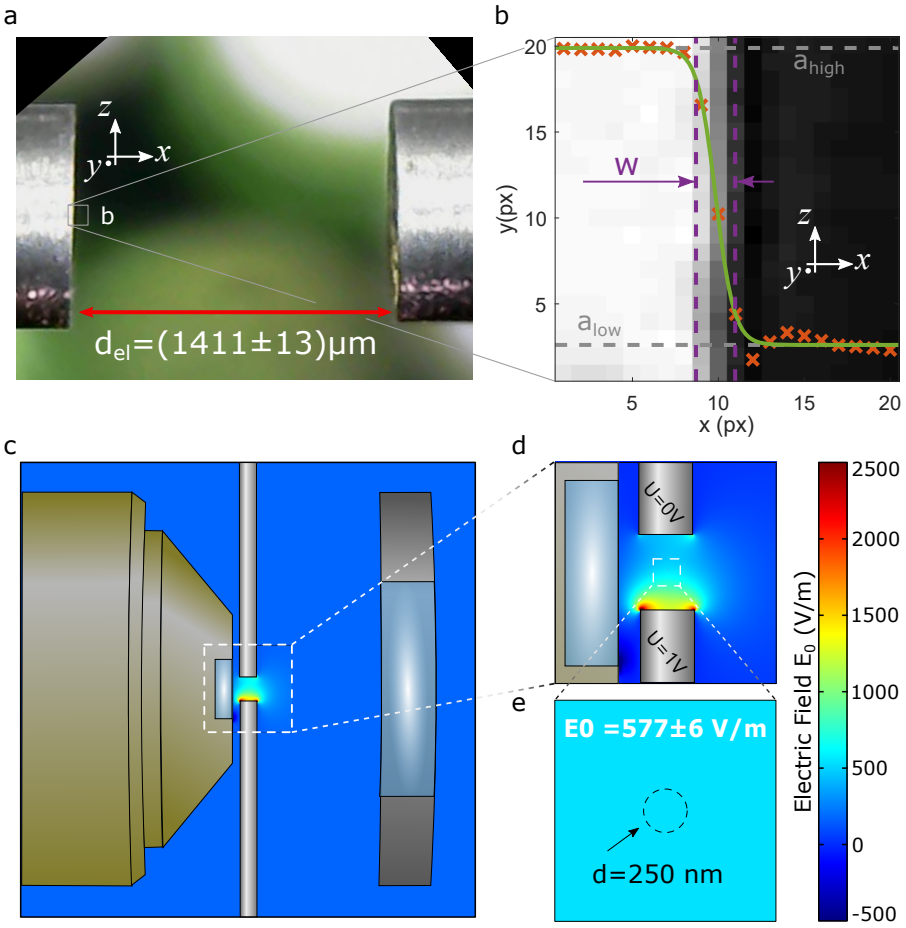

Figure 4.5: **Electrodes geometry and electrical field simulation**. (a) A high resolution image of the electrodes geometry taken *in-situ* with a portable microscope. Distances are calibrated via the electrodes diameter, which are known up to 1 μm tolerance. We measure a separation between the electrodes $d_{\text{el}} = 1411$ μm . (b) The uncertainty $\sigma_{d_{\text{el}}}$ over the electrodes' gap is calculated from the edge blurring of the image. (c) Overall geometry of the set-up that is used to simulate the electric field at the trap position. (d) Magnified version of (c) shows that field between the electrodes is barely affected by the presence of the dielectric lens in the objective. (e) The field E_0 can be considered constant and homogeneous in the volume explored by the particle. The uncertainty on the value of E_0 is calculated performing different simulations while varying the distance d_{el} and misplacing each of the electrodes by $\sigma_{d_{\text{el}}} = 13$ μm.

in order to estimate the electric field at the particle's position. Both objective and collection lens are modeled as a metal holder with an inset dielectric. One of the two electrodes is grounded (i.e. $U = 0$ V potential), while on the other we apply a dc voltage ($U = 1$ V). Figure 4.5c–e shows the outcome of the simulation. As expected, the effects of the collection lens are negligible, while we observe the field being slightly affected by the objective and the dielectric

lens. Nevertheless, in between the electrodes the field is quite homogeneous, and we find $E_0 = 577 \pm 6$ V/m, where the uncertainty σ_{E_0} is estimated performing different simulations while varying the distance d_{el} and misplacing each of the electrodes by $\sigma_{d_{\mathrm{el}}} = 13$ μm.

Power spectral density The two heights of the power spectral densities $S_v(\omega_{\mathrm{dr}})$ and $S_v^{\mathrm{th}}(\omega_{\mathrm{dr}})$ from which the ratio R_S is calculated are only affected by statistical errors since simulations confirm the validity of the linear model. σ_{S_v} is thus calculated as the standard error of the mean of N_{psd} measurements, with the $1/\sqrt{N_{\mathrm{psd}}}$ trend being verified. The same applies for S_v^{th}, where in this case $\sigma_{S_v^{\mathrm{th}}}$ is calculated from the measurements in the absence of external electric driving.

The statistical nature of the errors affecting $S_v(\omega_{\mathrm{dr}})$, $S_v^{\mathrm{th}}(\omega_{\mathrm{dr}})$ and Γ ideally allows one to increase the integration time of the measurement in order to arbitrarily reduce the associated errors σ_{S_v}, $\sigma_{S_v^{\mathrm{th}}}$, and σ_Γ. However, this approach is only valid as long as the system is not affected by slow drifts that affect the system over long timescales. As demonstrated by Hebestreit et al. [44], one can define an optimal measurement time to extract the *energy* $\hat{E}(\mathcal{T}) = \langle v^2 \rangle_{\mathcal{T}}$ of the particle. Here $\mathcal{T}$ expresses the time span of the dataset from which the variance $\langle \cdot \rangle$ is calculated. Note that $\hat{E}$ is not the physical energy, but is proportional to it. More precisely we have $\hat{E} = \frac{2E_{\mathrm{pot}}}{m\Omega_0^2}$. The longest useful integration time is thus assessed through the *Allan Deviation* of the variance $\hat{\sigma}_E$, calculated from a long position time trace $v(t)$ of ~ 2 hours. After chopping $v(t)$ into $N_{\mathcal{T}}$ shorter sections of variable length $\mathcal{T}$, we compute $\hat{E}_j(\mathcal{T})$ for each section $j = 1, \ldots, N_{\mathcal{T}}$. The Allan deviation of the the energy is then calculated for each value of $\mathcal{T}$ as:

$$\hat{\sigma}_A = \sqrt{\frac{1}{2(N-1)} \sum_{j=1}^{N} \left(\hat{E}_{j+1} - \hat{E}_j\right)} \tag{4.12}$$

In Fig. 4.6 we show $\hat{\sigma}_A$ as a function of τ for different pressures in the vacuum chamber. The experimental results demonstrate maximum stability for integration times of $\tau \sim 40$ s. Moreover, for higher pressures we observe lower minimas in the Allan deviation, which also indicates a better stability of the system. We believe this is due to the minor influence of nonlinearities, that are minimized for pressures $P > 10$ mBar.

Fitting parameters and nonlinear contributions In order to estimate the uncertainty of the Lorentzian fitting parameters, and to additionally ensure the

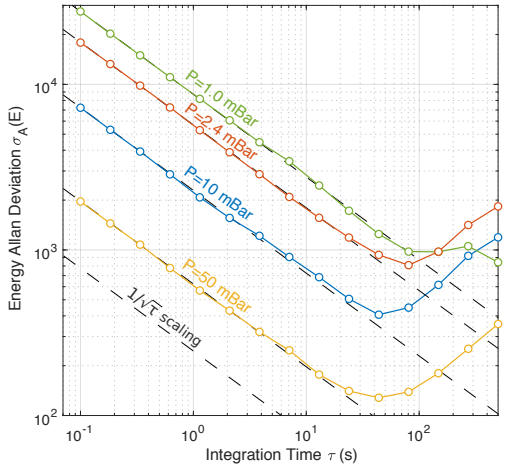

Figure 4.6: **Energy Allan deviation measurement.** The Allan deviation of the energy $\hat{E} = \langle v^2 \rangle$ is shown as a function of the integration time τ, for different pressures. At the operating pressure of $\sim$ 50 mBar we obtain maximum stability for $\tau \simeq 40$ s. Lower pressures present a higher Allan deviation, and consequently a degraded stability, probably due to the onset of higher nonlinearities in the dynamics of the particle.

validity of the linear resonator model, the effects of nonlinearities in the dynamics of the particle need to be further investigated. Such nonlinearities arise from the anharmonicity of the optical potential [36]. The system can then be modeled as a Duffing resonator, for which the linear stiffness becomes a function of position $k(x)$, and the equation of motion therefore reads:

$$m\ddot{x} + m\Gamma\dot{x} + m\Omega_0^2\left(1 + \xi x^2\right)x = \mathcal{F}_{\text{th}}(t) + F_{\text{el}}(t)\ , \tag{4.13}$$

where $\xi < 0$ is the so called nonlinear *Duffing* coefficient. Prompt consequence of the presence of nonlinearities in the dynamics of a resonator is that the eigenfrequency Ω_0 does not correspond to the curvature of the harmonic potential, but it gets shifted (down-shifted if $\xi < 0$, up-shifted if $\xi > 0$) and becomes energy dependent. More precisely we have:

$$\Omega_{\text{NL}} = \Omega_0\left(1 + \frac{3}{4}\xi\langle x^2\rangle\right), \tag{4.14}$$

where $\langle x^2 \rangle$ is the variance of the oscillation. We can exploit equation (4.14) to retrieve the value of ξ by driving the particle with increasingly stronger electric field E_0 and monitoring the frequency Ω_{NL} shifted by the nonlinearity. We use the calibration factor c_{cal} to convert the experimental variance $\langle v^2 \rangle$ into a calibrated $\langle x^2 \rangle$ with physical units of nm^2. Figure 4.7 shows the nonlinear frequency shift $\frac{\Omega_{\text{NL}}}{\Omega_0} - 1$ for increasing variance $\langle x^2 \rangle$. Low driving does not

affect the energy of the particle, and no shift is indeed detected. For $\langle x^2 \rangle \gtrsim 2100$ nm^2 a shift in frequency is observed, and we perform a linear fit to the experimental data according to Eq. 4.14. From the fit we retrieve: $\xi = (-9.03 \pm 0.44)\ \mu\text{m}^{-2}$. The obtained value is in agreement with previous measurement obtained from a completely different method [88] that provided $\xi = (-9.68 \pm 0.15)\ \mu\text{m}^{-2}$.

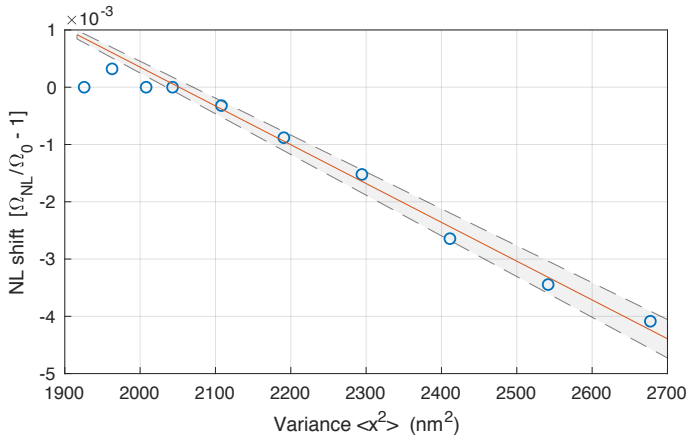

Figure 4.7: **Nonlinear frequency shift.** Due to the anharmonicity of the optical potential, a nonlinear frequency shift is observed when the particle is excited by the electric actuation. For variances $\langle x^2 \rangle \gtrsim 2100$ nm^2 we observe a linear shift, in agreement with eq. (4.14). A linear regression (red solid line) and related standard deviation (gray area) allow to extract the value of the nonlinear coefficient $\xi = (-9.03 \pm 0.44)\ \mu\text{m}^{-2}$.

Once the onset of nonlinearities in the system has been characterized, it is important to understand whether these play a role in the mass measurement protocol described in the previous section. To ensure the validity of the linear (harmonic) model, we also considered a cubic term in the restoring force and performed Montecarlo simulations of the resulting Duffing resonator with parameters compatible with our experimental settings and an overestimated value of the Duffing coefficient [38, 88] $\xi = 12\ \mu\text{m}^{-2}$[1]. The outcome of the simulations, detailed in Fig. 4.8, show that at pressures of $P = 50$ mBar nonlinearities lead to relative errors on the estimated fitting parameters Ω_0 and Γ of the order of a few 0.1% with respect to the exact values used in the simulations. This magnitude of errors is consistent with the validity of the linear model. Note that this is not the case for lower pressures $P \lesssim 10$ mBar, where the errors result to be at least one order of magnitude higher, and a more complicated nonlinear response model would be needed. This is also con-

[1] I acknowledge G.P. Conangla for his help in the simulations

firmed by Fig. 4.8 (see inset), where for the $P = 10$ mBar case we observe a non-negligible nonlinear shift of the resonance peak.

[h]

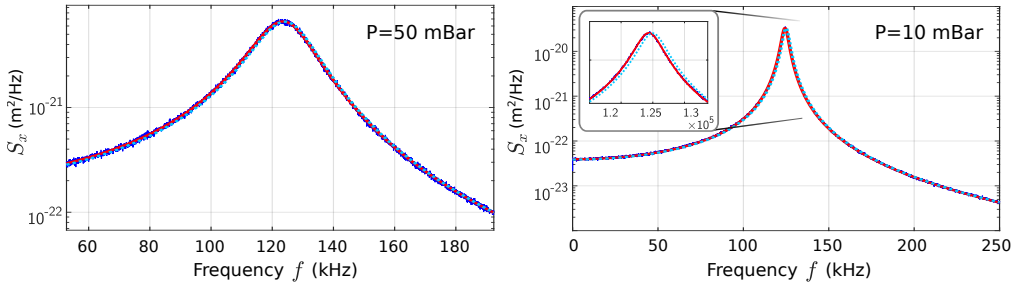

Figure 4.8: **Estimated PSD from simulated traces**. Two PSDs, estimated from the simulation of 1000 traces of 40 ms each, are displayed, corresponding to pressures of 50 mBar (left panel) and 10 mBar (right panel). Dark blue lines corresponds to the results of the simulation, red lines corresponds to the fitted function (which assumes a linear model, even if the simulated potential has a Duffing term), and the dashed light blue corresponds to the exact linear response, calculated with the values of Γ and Ω_0 used in the simulation.

Temperature The thermal bath surrounding the particle is assumed to be constantly thermalized with the set-up, and more precisely with the walls of the vacuum chamber, i.e. $T_{\text{bath}} = T_{\text{chamber}}$. Note that this assumption would not hold for low pressures ($P \lesssim 1$ mBar), where the rarified gas reduces the efficiency of convection and infrared laser absorption would rise the internal bulk temperature T_{bulk} of the particle [46]. In that case, one should include a two bath model [69] and consider a higher effective bath temperature and a corresponding higher uncertainty. However, the moderately high pressure $P = 50$ mBar used in our measurements ensures the assumption $T_{\text{bulk}} = T_{\text{bath}} = T_{\text{chamber}} = T$. To estimate this value, multiple temperature measurements on the surface of the vacuum chamber are carried out with a precision thermistor (0.5°C accuracy) in order to exclude the presence of temperature gradients and significant variations during the experimental times. The uncertainty on the bath temperature is therefore of the order of $\sigma_T/T \sim 0.2\%$. However, a stable and constant temperature T is ensured only if the set-up is properly isolated from the lab environment. Isolation is achieved by enclosing the whole optical table in a unique box that maintains a more stable temperature and screens the setup from air turbulence. The effect of this latter is to introduce pointing instabilities in the optical path, with the more drastic consequence being the unbalancing of the photoreceivers up to saturation. Figure 4.9 displays the measured temperature trend in the lab (probe placed in the middle of the room) and at the vacuum chamber position. We

observe that while the lab is exposed to temperature fluctuations of a few degrees, the temperature inside of the box screening the set-up is maintained stable, with variations that are well within the assumed accuracy.

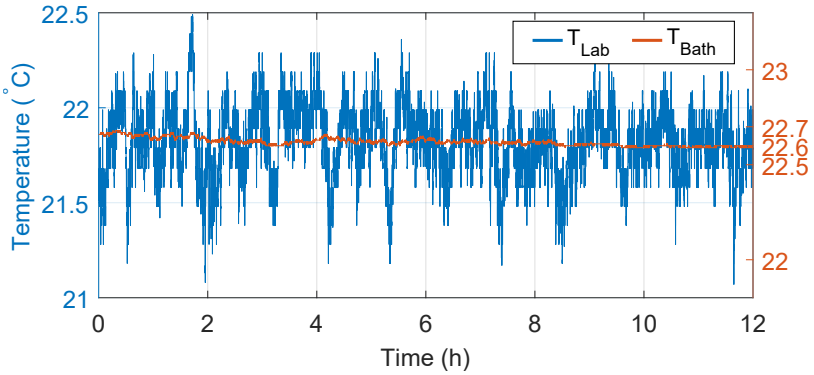

Figure 4.9: **Temperature measurement in the system**. A first temperature probe (blue solid line) is placed in the middle of the lab, exposed to air turbulences and the constant variations due to the air conditioning. However, a second probe (red solid line) in contact with the vacuum chamber's walls measures the bath temperature surrounding the particle. A consistent reduction of the temperature fluctuations is achieved enclosing the set-up and carefully screening it from air turbulences.

4.3.5 Error Estimation

All the quantities involved in the mass calculation are subject to both systematic and statistical errors. However, it is legitimate to assume that for E_0 and T, the systematic one has a dominant contribution and the random error is negligible, while for R_S and Γ the opposite holds.

Assuming uncorrelated variables, we can therefore apply the well-known variance formula [58] to propagate the relative errors:

$$\sigma_m = \sqrt{\sum_i \left(\frac{\partial m}{\partial z_i}\right)^2 \sigma_{z_i}^2}, \tag{4.15}$$

where z_i runs over the variables reported in Table 4.1, exceptions made for those in gray color for which $\sigma_{z_i} \simeq 0$. As a result we obtain:

$$\frac{\sigma_m^{\text{syst}}}{m} = \sqrt{\left(2\frac{\sigma_{E_0}}{E_0}\right)^2 + \left(\frac{\sigma_T}{T}\right)^2} \tag{4.16}$$

$$\frac{\sigma_m^{\text{stat}}}{m} = \sqrt{\left(\frac{\sigma_{S_v}}{S_v^{\text{el}}}\right)^2 + \left(\frac{\sigma_{S_v^{\text{th}}}}{S_v^{\text{el}}}\right)^2 + \left(\frac{\sigma_{S_v^{\text{th}}}}{S_v^{\text{th}}}\right)^2 + \left(\frac{\sigma_\Gamma}{\Gamma}\right)^2} \tag{4.17}$$

Plugging in the errors reported in Tab. 4.1, and thoroughly assessed in the previous paragraphs, we obtain $\sigma_m^{\text{syst}}/m = 2.24\%$ and $\sigma_m^{\text{stat}}/m = 0.91\%$

As a concluding remark, we stress once more the importance of such an accurate measurement of the particle's mass, that outperforms existing methods by more than one order of magnitude. This results are pivotal for boosting the accuracy of levitation-based sensors, paving the way for more reliable impact of levitodynamics in sensing and metrology.

5 Pressure-dependent mass and charge

Contents

5.1 Introduction

At the early stages of this doctoral work, the silica nanoparticles used in our experiments were modeled as solid spheres of bulk amorphous silica. Their mass (thoroughly discussed in § 4.3) was indeed calculated using the density of fused silica reported in common material science handbooks, and the properties of particle's material were considered constant throughout the whole experiments. However, unexpected irreversible phenomena (described in § 5.2.1 and consisting in pressure-dependent properties of the particle) could be repetitively observed while going to vacuum right after loading the particle in the trap. Such observations were shared with other research groups

working in levitation, yet without a commonly accepted explanation of their causes. This chapter is dedicated to an in-depth investigation of the phenomenon, with the objective of disclosing its unclear causes.

In the first part of the chapter (§ 5.2 and § 5.2.2) we will restrict ourselves to pure experimental observations, leaving out (where possible) any interpretation of the presented data. Then, in § 5.4 we will suggest a surface chemistry model (Zhuravlev model) of silica that seems to correctly explain our observations and will provide a quantitative matching of this theory with our data. The objective of such a careful study of the involved phenomena seeks a deeper understanding of our system, and consequently goes toward the establishment of a reliable sensor.

5.2 Observations of pressure-dependent mass and charge

In this section we will provide an in-depth description of the particle's behavior during the process of pressure reduction in the vacuum chamber. We will monitor important pressure-dependent variations of oscillation frequency Ω_0, mass m, charge q and scattering intensity B. In order to get a better understanding of the behavior of these quantities we tracked their values while performing consecutive pump down and venting cycles. A qualitative and quantitative analysis of the results will provide the basis for an interpretation of the observed phenomena and will pave the way for the development of a simplified model in § 5.4.

5.2.1 Properties changes during pump down process

In a typical levitation experiment, once a single nanoparticle is loaded in the trap the pressure in the chamber is lowered in order to reach the high vacuum conditions. During the pump down the particle's dynamics along the three motional degrees of freedom is continuously monitored. In the following we will consider only the x–mode of oscillation. The position x is sampled at a rate $f_s = 625$ kHz, and the corresponding single-sided power spectral density $S_v^{(x)} = S_v$, is computed at a rate of $f_s/N \simeq 76$ Hz ($N = 8192$ being the number of points in the PSD). This allows us to measure the eigenfrequency Ω_0 and the mode energy $\hat{E} = \int_{\Omega_0-b}^{\Omega_0+b} S_v(\omega)\mathrm{d}\omega$, where $b \simeq 40$ kHz.
Right after loading, the particle naturally carries a few elementary charges (of the order of $n_q^{\mathrm{in}} \simeq 10$, although this value depends on the particle's size). These are sufficient to monitor possible charge variations Δq. This is done

by applying a voltage signal to the electrodes that creates an electric field $E(t) = E_0 \cos(\omega_{\mathrm{dr}} t)$ in the vicinity of the trapping region. This oscillating electric field excites a coherent oscillation of the nanoparticle along the x axis. We detect the oscillation as a sharp peak appearing at ω_{dr}, whose associated energy $\hat{E}_{\mathrm{el}} = \int_b S_v(\omega)\mathrm{d}\omega \propto q^2$ is tracked in time integrating S_v in a small bandwidth b around ω_{dr} (see inset in Fig. 5.1d and Fig. 3.11a).
Finally, the pressure P is continously measured with a *full-range* gauge and the scattered light B from the particle is detected with an imaging system placed below the vacuum chamber (see set-up schematics in Fig. 4.2).

In the first stage of the pump down, more precisely between ambient pressure and $P \sim 0.1$ mBar we always observe a continuous decrease of particle's eigenfrequency and brightness, followed by an abrupt drop of those quantities at $P \lesssim 0.1$ mBar. Figure 5.1 is a typical example of such experiments, where a pump down and vent cycle is followed by a second pump down process. This Figure shows the pressure P, the brightness B, the eigenfrequency $\Omega_0 = \Omega_0^{(x)}$ and the energy $\hat{E}_{\mathrm{el}}$ as a function of time. For the sake of clarity in the description, the plot has been divided into five different time slots:

I) The system is brought from ambient pressure to $P \lesssim 1$ mBar. As soon as we start reducing the pressure we observe a smooth decrease ($\sim 30\%$) of the brightness B. The shaded regions are meant to avoid confusion marking the regime where the dynamics is overdamped and hence quantities such as Ω_0 and E_{el} are ill-defined. As a result, a properly determined $\Omega_0 \simeq 130$ kHz appears when the particle enters in the ballistic (underdamped) regime at $P \lesssim 50$ mBar. We observe a slight drift in frequency between $t = 200$ s and $t = 300$ s. This is due to the pressure dependency of the susceptibility $\chi(\omega)$ of the resonator, and for the same reason the energy $\hat{E}_{\mathrm{el}}$ also decreases (Fig. 5.1d). We stress, however, that this drift cannot be attributed to variations in the particle's charge. Indeed, we observe the same behavior even when the particle is fully discharged and no peak is present at ω_{dr}.

II) In this pressure range the system reaches a steady state condition and all the tracked quantities (B, Ω_0, E_{el}) now display a plateau. At $t \simeq 450$ s and $P \simeq 0.1$ mBar, both the brightness B and the frequency Ω_0 drop abruptly. Simultaneously, the energy $\hat{E}_{\mathrm{el}}$ sharply increases indicating an abrupt charging (or discharging) event that leads to $|n_q^{\mathrm{fin}}| \gg |n_q^{\mathrm{in}}|$, with n_q^{in} and n_q^{fin} being the electrical charge before and after the abrupt event, respectively.

III) The system displays overall stability after phase II. We stop the pump

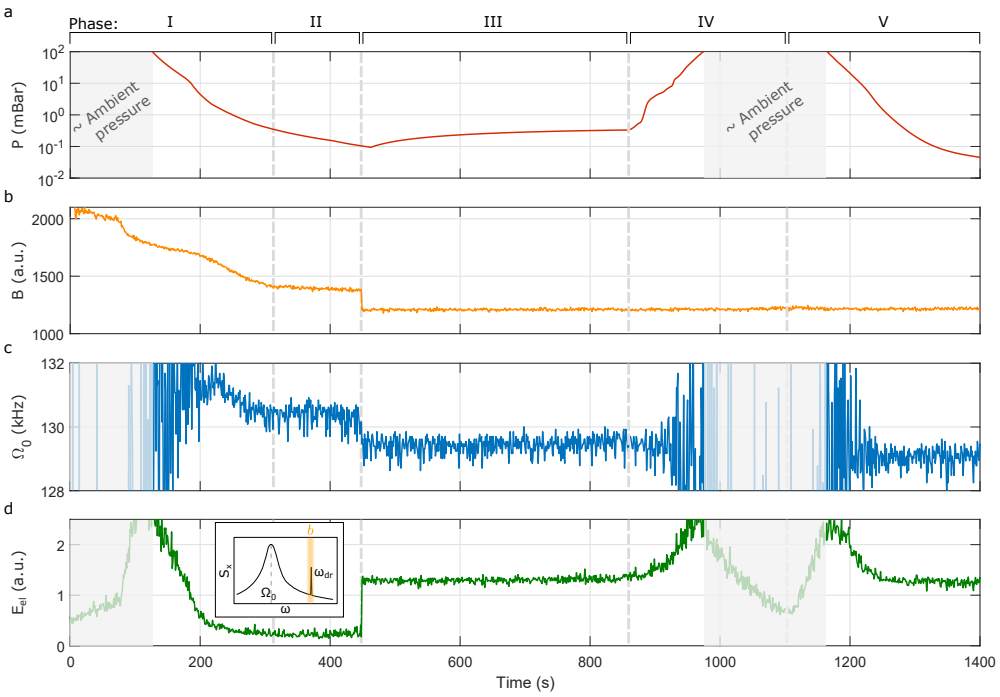

Figure 5.1: **Observation of pressure-dependent properties.**(a) Pressure during a sequence of pump down, venting and aditional pump down. (b) The scattering intensity B, measured with an imaging system and a CCD camera, shows a smooth initial decrease, followed by a stable plateau and an abrupt drop. After this sudden event, the intensity is maintained constant throughout venting and subsequent pump down. (c) The oscillation frequency Ω_0 shows a similar behavior of B, exceprtion made for the regions of too high damping. (d) The energy of the electrically driven oscillation shows an abrupt and considerable increase during corresponding to the drop of B and Ω_0, consistent with a charge variation.

down, pressure reequilibrates at ~ 0.5 mBar and no significant changes in the observed quantities are detected.

IV) Increasing the pressure back to ambient conditions demonstrates the irreversibility of the observed phenomena. Although the frequency Ω_0 and the energy $\hat{E}_{\mathrm{el}}$ feature a trend similar to the one observed during the pump down due to the pressure-dependent susceptibility $\chi(\omega)$ of the oscillator, the brightness B remains constant. This clearly indicates that the particle is not affected by pressure changes anymore.

V) Finally, a second pump down to even higher vacuum ($P < 0.1$ mBar) leads to almost identical values of the tracked magnitudes. We only observe a negligible shift in the eigenfrequency ($\Delta\Omega_0 \approx 0.25\%$) , probably due to the hysteresis of mechanical stresses in the chamber.

5.2.2 Mass measurement during pump down process

The mass measurement protocol developed in § 4.3.2 can be used to correlate the observations made in the previous section with possible mass losses from the particle. The mass measurement method provides reliable results only if the system is operated in the linear regime, i.e. at relatively high pressures of $P \simeq 50$ mBar. Consequently, although an ideal protocol would consist in consecutive mass measurements at progressively lower pressures, we will need to alternate pump downs and venting (up to $P \simeq 50$ mBar) in order properly estimate the mass. Figure 5.2 exemplifies such an adapted protocol. First, the pressure in the vacuum chamber is reduced from ambient to $P = 50$ mBar. In this process particles lose on average $(15 \pm 1)\%$ of the initial scattering intensity B. Interestingly, this percentage loss is independent from the particle size. A first mass measurement is performed with the method described in § 4. We stress that the initial scattering loss suggests that the mass measured at $P = 50$ mBar probably does not coincide with the original mass of the particle (at ambient pressure) right after loading. Subsequent measurements are operated after progressively higher vacuum levels are reached and show a constant trend of mass loss. The bottom panel of Fig. 5.2 represents this situation for a particle $d \simeq 235$ nm in diameter. Both the absolute percent loss $\Delta m^{(0)}$(with respect to the first measurement, i.e. the accumulated mass loss) and the relative loss $\Delta m^{(i-1)}$ (with respect to the previous mass read) are displayed. These measurement are usually repeated until $P = 1$ mBar. Below this pressure the particle undergoes the sudden and abrupt event described in the previous section § 5.2.1. Interestingly, a considerable fraction of mass is lost during this phenomenon. Repeated measurements on different particles seems to show that the amount of mass lost during the abrupt event is proportional to the slope of the pressure trend, i.e. faster pump downs lead to more prominent sudden mass losses. This observation, however, should be the object of more quantitative analysis in future experiments.

In the inset of Fig. 5.2, top panel, we show a peculiar feature of the investigated phenomenon. Concurrently with a cycle of pump down and venting, we observe a decrease and a subsequent increase of the scattered intensity B. Note that the final level is always slightly lower than the starting level right before the pump down. Assuming a monotone relation between m and B[1], this observation suggests that mass is lost as pressure is reduced, and it is partially regained when the chamber is vented. Further investigations on this

[1]This assumption is supported by the following argument: the volume corresponding to the mass lost is replaced by vcuum (e.g. voids in the bulk structure of the particle), with a consequent reduction of the overall refractive index.

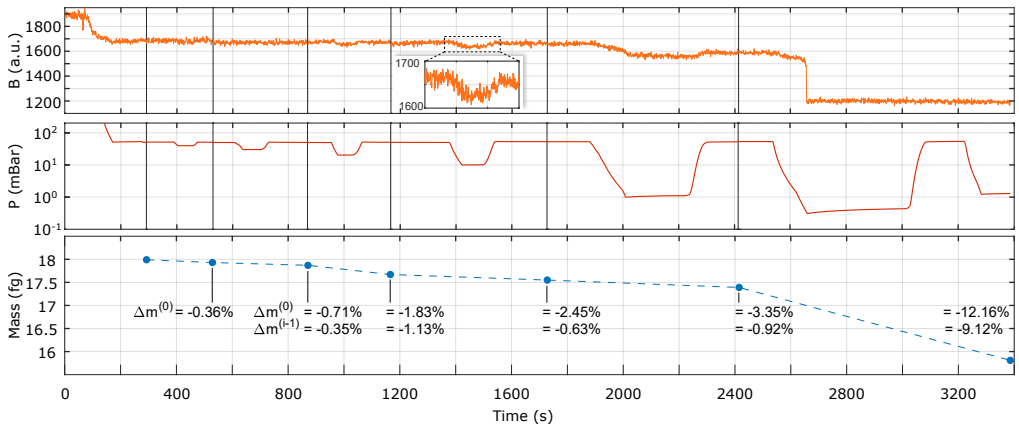

Figure 5.2: **Mass measurement during pump down**. The top two panels represent respectively scattering intensity B, and pressure P during repetition of pump downs and venting where progressively lower pressures are reached. The bottom panel shows the mass m, measured after every venting cycle at a pressure of $P = 50$ mBar. We observe a clear trend of mass loss during the first part the pump down, and a considerable mass lost during the abrupt event at $P \sim 0.1$ mBar. Numbers indicate the absolute percent loss $\Delta m^{(0)}$ (with respect to the first measurement) and and the relative loss $\Delta m^{(i-1)}$ (with respect to the previous mass read).

peculiar behavior are carried out in the next section, where different venting procedures seems to confirm the hypothesis of a a possible mass uptake.

5.2.3 Mass uptake from a humid environment

A comprehensive description of the particle material, as well as its surface chemistry and other important related features will be given in the next section § 5.4. For the moment it is sufficient to mention that the material composing the nanoparticles, the so-called *Stöber* silica [104] named after the inventor of the sinthetization method, is a highly porous material. Several studies [31, 59, 81, 114] report this fact and treat the subject of water evaporation and adsorption from porous amorphous silica. This well known fact suggests that the phenomenon observed in the inset of of Fig. 5.2 could be compatible with the evaporation of water contained in the particle (brightness decrease) followed by a subsequent uptake of water molecules from the humid environment (brightness increase). It should be reminded, in fact, that the loading of the particle takes place at ambient pressure and that humidity levels in the laboratory are maintained within 50-55%.

In order to support (or to exclude) this hypothesis, we performed the experiment shown in Fig. 5.3. During a first cycle of pump down from ambient pressure to $P = 50$ mBar and subsequent venting of the chamber, the scattering

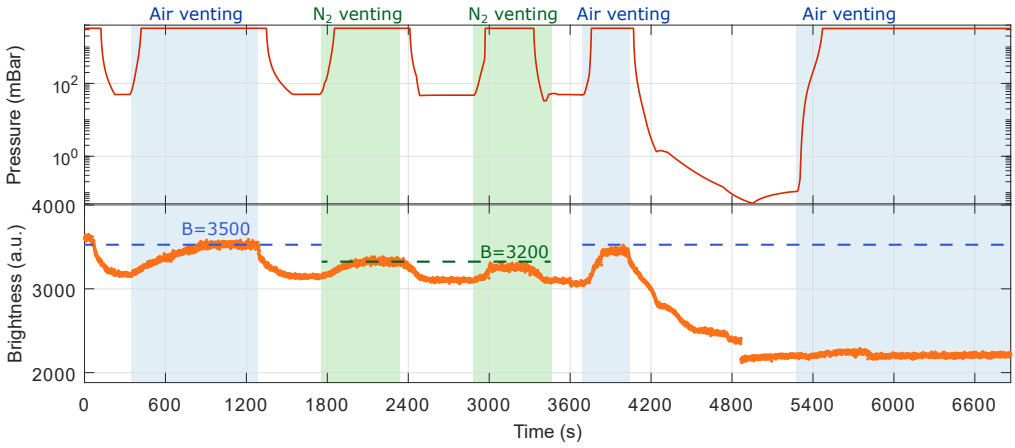

Figure 5.3: **Water uptake during chamber venting.** Pressure (top panel) and scattering intensity B (bottom panel) of a repetition of pump downs and venting with different types of gasses: humid air and dry N_2. Data shows the ability of amorphous silica of loosing mass (water desorption) and uptake mass (water absorption) if exposed to a humid environment.

showed the expected behaviour. When venting with (humid) air from the lab, we observe that B goes back almost to the initial scattering level ($B \simeq 3500$). However, if we repeat the pump down an the venting process, this time with dry N_2 we observe a considerable reduction of the final level of $B \simeq 3200$. This effect is reproduced a second time, and shows compatible results. Finally, if the air venting is restored and one additional cycle is performed, the scattering intensity goes back to higher levels ($B \simeq 3500$), compatibles with the initial state of the particle. This observations can be easily explained by porous amorphous silica losing water content when brought to vacuum, and regaining mass in the form of water molecules from the humid environment. This also explain why the nitrogen venting, i.e. lower water content in the vacuum chamber, leads to less prominent increase of brightness. Interestingly, such a pressure-dependent behavior disappears after the system undergoes the sudden event in which both mass and scattering drop and the particle acquires additional charges.

5.2.4 Charge variations: observations and statistics

In this section we investigate in more detail the sudden charging/discharging phenomenon that takes place when going into vacuum right after the loading (see Fig. 5.1d, sector II). We will provide also some statistical insights about the magnitude of the charge variations.

As a first interesting observation we point out that although the mass con-

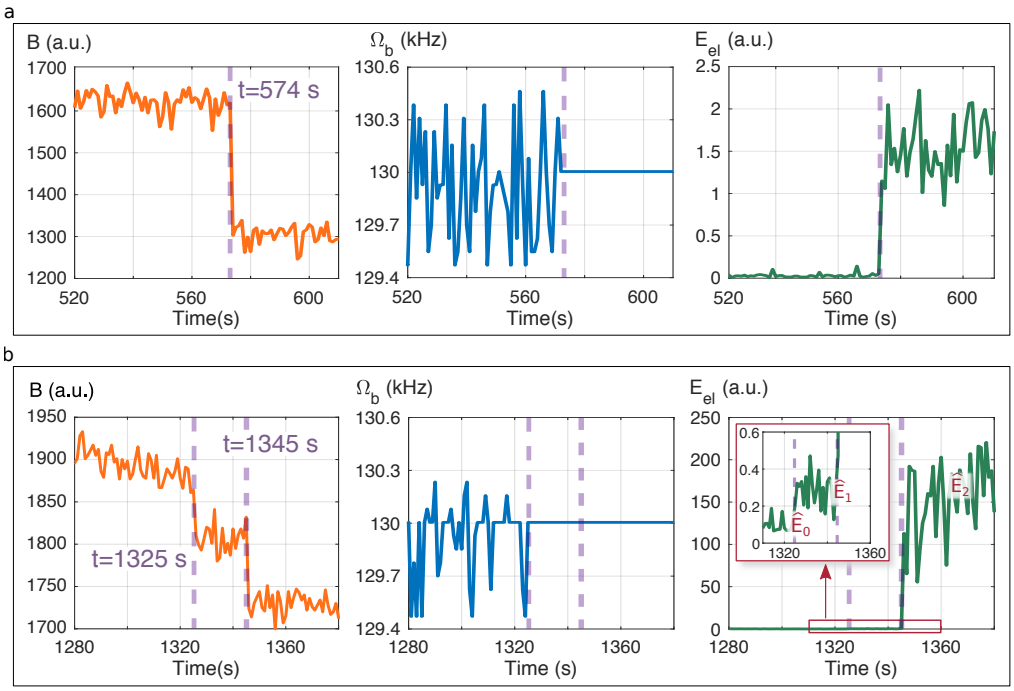

Figure 5.4: **Typical and peculiar event of particle abrupt charging**(a):Left to right: scattering intensity$B$, frequency Ω_b and energy $\hat{E}_{\rm el}$ of the electrically driven oscillation for a typical mass drop event at $P \sim 0.1$ mBar. (b) The same quantities reported in (a) for an event more rare case where a double drop is observed. As explained in the main text, the peculiarity of such an event is that most of the final charge is gained during the second drop at $t = 1345$ s.

tinuously changes: from the beginning of the pump down process, until the occurrence of the mass drop between $P \in 10^{-2} - 10^{-1}$ mBar, charge variations are detected only during this final abrupt event.

To further investigate this fact, we can now fully discharge the particle (to neutral) with the ignition of the plasma (see § 3.5) before it reaches the critical pressure regime. Figure 5.4a displays the parameters of interest for a neutral particle close to the abrupt event taking place at time $t = 574$ s (dashed vertical lines). An external electric field $E(t) = E_0 \cos(\omega_{\rm dr} t)$ is applied during the measurement. From left to right we show the brightness B, the oscillation frequency Ω_b and the energy $\hat{E}_{\rm el} \propto |n_q|^2$, these latter two being calculated in a narrow bandwidth ($b \simeq 1$ kHz) around $\omega_{\rm dr}$. As expected, the neutral particle does not respond to the applied electric field. Therefore, at $t < 574$ s we observe $\hat{E}_{\rm el} \simeq 0$, an undefined Ω_b and a stable value of B. As soon as the particle undergoes the abrupt event, at $t = 574$ s, the scattered intensity drops and the appearance of a driven peak at $\omega_{\rm dr}$ indicates that the particle now couples to the electric field. This observation unambiguously confirms

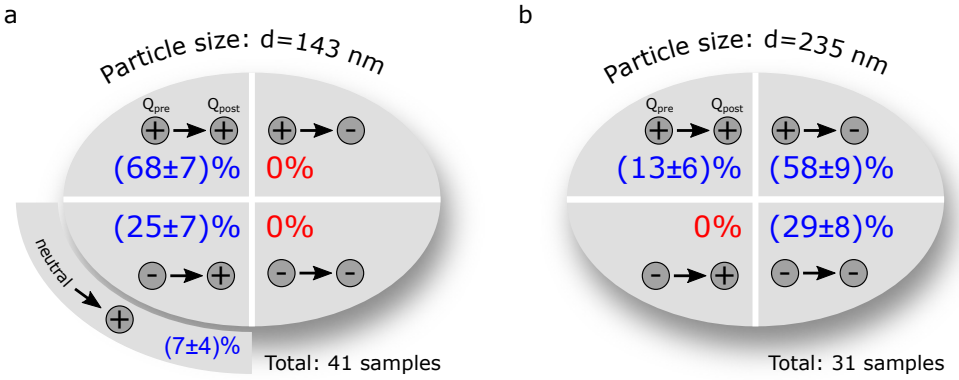

Figure 5.5: **Statistics of the particle's charge before and after the abrupt event.** (a) For the $d_p = 143$ nm particles we only observe positive polarity after the charging event, with the majority of particles also having an initial positive charge. Note that for this size, neutral particles can also be found after the loading. (b) The $d_p = 235$ nm particles show a completely different statistics than the smaller ones. Most of the times ($\sim 90\%$) they end up being negatively charged but we still observe particles with positive polarity after the charging event. The only case that seems not to be possible for this size is the transition from negative to positive polarity.

that the neutral particle gains a net charge during this event. In Figure 5.5 we report some statistical analysis of this charging event for two different particle size: $d_p = 143$ nm and $d_p = 235$ nm, and observe that these lead to a radically different statistics of the initial and final polarity. First of all we note that for both sizes the initial polarity after the loading is predominantly positive (70% vs. 30%). However, the behavior of the two samples studied seems to be be the opposite after the charging event. We in fact end up with only positive particles for the smaller size (100% vs. 0%) and a statistics predominantly negative for the bigger particles (87% vs. 13%). These observation could be valuable information for the development of a model that takes into account the surface chemistry as well as the surface charge of amorphous silica particles.

What has been shown in Figs. 5.1 and 5.4a is the general behavior of a particle brought to vacuum right after being loaded in the trap. We now describe a less frequent event that has nevertheless been observed several times, especially with $d_p = 143$ nm. In Fig 5.1b we report the same measurement described above, carried out with a particle from the same batch as Fig 5.1a. In the left panel we see that the usual drop in B consists this time of two well separated drops. The interesting feature of this occurrence is that, at a first sight, the energy $\hat{E}_{el}$ steps up only at the second event, indicating that despite the two drops display comparable magnitudes, only the second one is affect-

ing the particle's charge. A more careful analysis, however, shows that this is only partially true (see inset in right panel). A little step in the charge is also observed during the first brightness drop. From the measured energies $\hat{E}_0 \simeq 0.1$, $\hat{E}_1 \simeq 0.3$ and $\hat{E}_2 \simeq 150$, and given the proportionality $(\hat{E}_i - E_0) \propto n_{q,i}^2$, with $i = 1, 2$, we can estimate that $n_{q,2}/n_{q,1} \sim 30$. In other words, throughout the second drop the particle acquires a charge approximately 30 times larger than during the first one. The reason of such an asymmetry is still not clear and will be subject of future investigation. We speculate that this could be due to a multilayer of water molecules (we will indeed introduce H_2O multilayers in § 5.4) that is desorbed in two subsequent events. In such a scenario most of the charges would depart only during the second drop because they tend to accumulate in the inner shell, close to the silica surface.

5.3 Measurement protocol for highly charged particles

In this section we propose and demonstrate a simple protocol to measure arbitrarily high number of charges n_q on the levitated nanoparticle. As shown in 3.5, when the corona discharge in the vacuum chamber is active, one can track the charge-steps that lead to a neutral particle and therefore retrieve the initial value of n_q by merely counting their number. This method is exemplified in Fig. 5.6a, resulting in $n_q = -19$. However, while the particles right after loading have a relatively small number of charges, on the order of $|n_q| = 10$, the abrupt event happening at $P \sim 10^{-1} - 10^{-2}$ mBar highly boosts this number leading to $|n_q| \gtrsim 50$ in small particles ($d_p = 143$ nm) and up to a few hundreds for the bigger ones. As a result, counting the number of steps during a particle discharge from an initial $n_q \gg 10$ is often a tricky task. In fact, one would need to observe the particle response to the external field for long times (of the order of one to few hours) to fully resolve all the charge steps. As we show in Fig. 5.6b, in fact, for $|n_q| \gtrsim 20$ the amplitude response displays a smooth decrease, while integer steps can be resolved only below this threshold (see figure insets). This is due to a rapid initial discharging of the particle[2] and to the detection of the high oscillations being affected by the nonlinearity of the probe beam.

Therefore, a more general method to measure $|n_q| \gg 10$ in these cases is highly desirable. In the following we describe an alternative protocol that

[2]When the particle is highly charged, ionized molecules of opposite polarity are strongly attracted towards the particle due to Coulomb interaction. Therefore, we expect an initial higher collision rate that quickly takes the particle close to neutral. However, this collision rate is much lower when $|n_q| \approx 0$ and and hence change variations happen on a slower time scale.

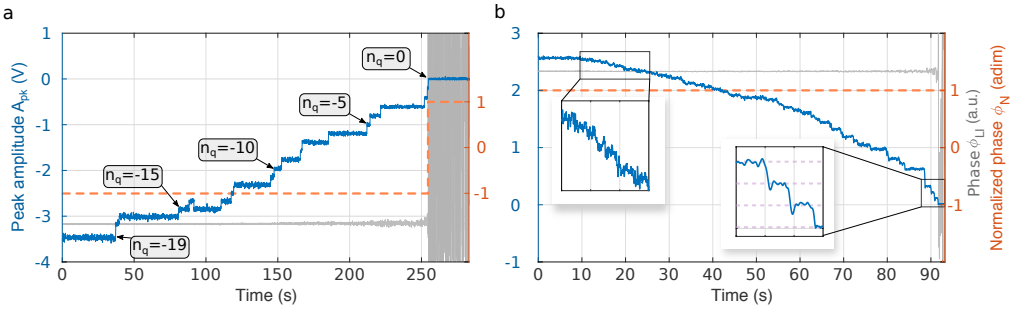

Figure 5.6: **Discharge to neutral before and after the abrupt event** (a) Peak amplitude A_{pk}, lock in phase ϕ_{LI} and normalized phase ϕ_{N}, as defined in § 3.5, while discharging from $n_q = -19$. (b) After the abrupt event $n_q \gg 10$ and steps cannot be fully resolved (see insets).

allows us to measure arbitrarily high number of charges.

(i) Suppose a particle with an unknown number of charges n_q^{in} is trapped in the focus. Bringing the system to $P = 50$ mBar enables us to apply the mass measurement protocol as described in 4.3. We recall here the equation for the ratio R_S that leads to the mass calculation:

$$R_S = \frac{S_v^{\mathrm{el}}(\omega_{\mathrm{dr}})}{S_v^{\mathrm{th}}(\omega_{\mathrm{dr}})} = \frac{S_v - S_v^{\mathrm{th}}}{S_v^{\mathrm{th}}}\bigg|_{\omega=\omega_{\mathrm{dr}}} = \frac{(n_q^{\mathrm{in}})^2}{m} \cdot \frac{q_e^2 E_0^2 \mathcal{T}}{8 k_B T \Gamma}. \tag{5.1}$$

Here all the quantities involved, except m and n_q^{in}, are either experimentally determined from the PSD of the thermally and harmonically driven resonator (i.e. Γ, R_S), or are parameters of our system (T, E_0, $\mathcal{T}$) or are physical constants (k_B, q_e). Consequently, we can define and calculate a quantity α_{qm} that takes a similar role to a *charge-to-mass* ratio:

$$\alpha_{qm} = \frac{(n_q^{\mathrm{in}})^2}{m} = \frac{8 k_B T \Gamma R_S}{q_e^2 E_0^2 \mathcal{T}} \,. \tag{5.2}$$

(ii) Once the α_{qm} is measured, we can discharge the particle through the plasma and set a (small) known number of charges n_q^{fin} by simply counting the step.

(iii) Repeating the mass measurement protocol, this time with the known value n_q^{fin} allows us to determine the absolute mass of the particle within $\sim 2\%$ error.

(iv) Assuming that no mass variations take place between (i)) and (iii) the initial number of charges n_q^{in} can finally be calculated as:

$$n_q^{\mathrm{in}} = \sqrt{\alpha_{qm} m} \tag{5.3}$$

This method has been experimentally validated using an initial known value of $n_q^{\text{in,real}} = 61$. Following the protocol (i)) to (iv) with a chosen value $n_q^{\text{fin}} = 5$ we estimated $n_q^{\text{in,est.}} = 64 \pm 2$, where the 3% uncertainty has been propagated using the erros provided in § 4.3.5. Although we don't exactly match $n_q^{\text{in,real}}$ (further verification should be carried out), we see that this method still provides a reliable quantitative measurement of highly charged particles.

5.4 Observations explained: the Zhuravlev model

In this section we provide a simple model to account for the experimental observations described in § 5.2.1-5.2.3. As a first step towards a better understanding of the observed particle behavior, a quite obvious, but essential fact should be stressed: the silica nanospheres used in our experiments were not specifically conceived for optical levitation experiments in vacuum, and they are indeed widely used in very diverse fields like biology, medicine and material science among others. The synthesis of these particles with size smaller then ~ 1 μm in diameter was proposed by Stöber et al. in 1968. One major advantage of this process is that it can produce higly monodisperse silica particles with coefficient of variation cv $= \sigma_d / \langle d \rangle$ as low as a few percent. Therefore, they provide an ideal model for studying colloidal phenomena. In a nutshell, the process consists in hydrolyzing tetraethyl orthosilicate $Si(OEt)_4$, commonly referred as TEOS. This is usually done in ethanol and using ammonia as a catalyst. The reaction produces $Si(OEt)_3OH$ and $Si(OEt)_2(OH)_2$ that can condensate producing granular silica with diameters ranging from 50 to 2000 nm depending on the experimental conditions. One important feature of Stöber synthesis is that the silica is produced in the amorphous (glass) phase, and not in the crystalline phase (quartz). Figures 5.7a,b exemplify the differencies in atomic conFiguration between the two types of SiO_2. Another fundamental trait of the silica obtained via the Stöber process, and more generally of any type of amorphous silica, is to have silanol groups (Si-O-H) on the surface. Figure 5.7c shows the different types of silanol that can be encountered. These are classified into isolated silanols (Q^3), geminal silanols (Q^2), vicinal silanols, surface siloxanes(Q^4) and internal silanols. Finally, amorphous silica is universally a porous material, both at the surface (open pores) and in the intenal structure (close pores) [81]. Depending on their size we can distinguish between macropores ($d > 200 - 400$ nm), mesopores ($3.0 - 3.2$ nm $<$ d $< 200 - 400$ nm) and supermicropores ($1.2 - 1.4$ nm $< d < 3.0 - 3.2$ nm). Ad-hoc chemical processes can

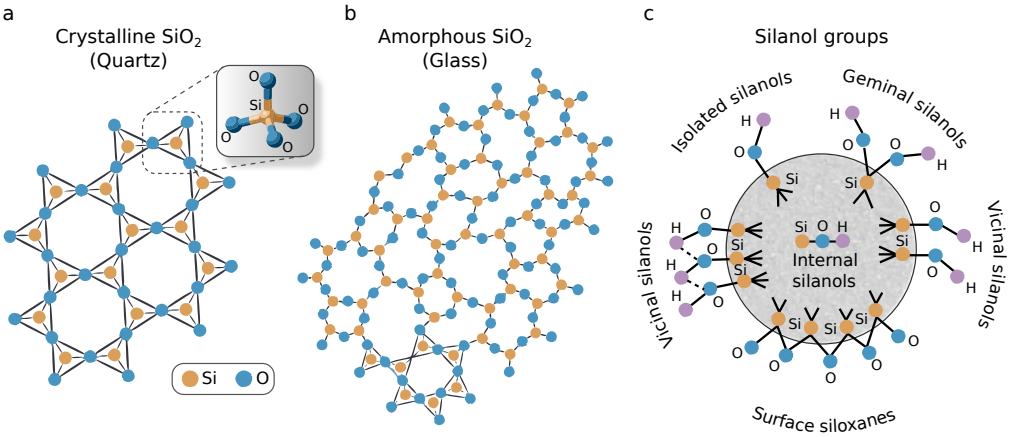

Figure 5.7: **The Stöber silica model** Difference between the (a) crystalline phase of silica (quartz) and (b) the amorphous phase. Inset shows the tetrahedral molecular geometry of SiO_2. (c) adapted from [114] shows the various types of silanol groups on the surface of amorphous Stöber silica.

be developed in order to intentionally make the material highly porous (for example for drug delivery in bio-medical applications [112]).

Although these porosity-boosting processes are not implemented in the synthesis of our nanoparticles, it is very likely that supermicropores are present both on their surface and in their internal structure [81]. A direct consequence of micro-porosity and of the presence of silanol groups at the surface is that the nanoparticles present a substantial content of water. This is referred as the silica being hydrophilic, which is the typical condition of the Stöber synthesis. Water can be found in different forms: physically adsorbed (or physisorbed) and chemically adsorbed (or chemisorbed). The former indicates H_2O molecules contained in the pores and/or physically bound to the surface, while the latter refers to the O–H carried by the silanol groups. Accordingly, one can define the processes of dehydration (removal of physically adsorbed water), dehydroxylation (the removal of silanol groups from the silica surface) and rehydroxylation (the restoration of the hydroxyl covering) [114]. These processes, and in particular the ones concerning the removal of water are usually performed by exposing the particle to high temperatures and vacuo for long times [31]. Depending on the temperatures reached one can observe different magnitudes of mass-losses in the form of water desorption, together with several other changes of particle properties such as density, refractive index, and most importantly surface chemistry. In particular, a comprehensive description of this latter as a function of the material temperature is provided by the so called *Zhuravlev model* [114].

Optically levitated nanoparticles in vacuum are expected to display similar behaviors to those observed and supported by the Zhuravlev model. In fact, although the light absorption of silica at the laser wavelength $\lambda = 1064$ nm is tiny, the fact of being levitated restricts the channels of energy exchange with the environment, leaving scattering asnd emission of black-body radiation and gas convection as the only cooling mechanism in high vacuum [16]. As a result, trapped silica spheres can experience internal bulk temperatures as high as $\sim$ 1000 °C below $P = 10^{-4}$ mBar [46]. In the following we will review some basic concepts of surface chemistry of amorphous silica, linking the model with the experimental observations drawn in § 5.2. We will often refer to Fig. 5.10 for a schematic representation of the particle's evolution.

STAGE 1

Right after loading, the particle is in a maximum state of hydroxylation (hydroxyl coverage θ_{HO}), meaning that every surface site is covered with an O-H group. Under these conditions, the silanol number α_{OH} (defined as the superficial density of silanols on the silica surface) has been extensively studied and literature largely agrees on the value $\alpha_{OH,T} = 4.60$ nm^{-2} [3]. Note that $\alpha_{OH,T}$ is considered a physico-chemical constant (independent of origin and structural characteristics of the silica) that goes under the name of *Kiselev–Zhuravlev* constant. Additionally, the SiO_2 surface is covered with physically adsorbed water in a multilayer (ML) form: $\theta_{H_2O} \gg 1$. Observations of up to $\sim$ 12 ML have been reported in [101], and we expect this value to be even higher in our case. In Fig. 5.8 we calculate and represent the mass of water on the surface of the particle as a function of the number of multilayers and of the particle's size. In the two cases we studied $d_p = 143$ nm and $d_p = 235$ nm the values obtained are compatible with the mass-losses dicussed in § 5.2.2.

STAGE 2

During the first part of the pump down the external layers of water molecules are desorbed from the surface according to the dehydration process. This is responsible for the smooth mass and scattering losses shown in Fig. 5.2. The relatively high pressure in this regime still provides sufficient gas convection that ensures a cooling rate higher than the heating rate from light absorption, and the particle thus maintains a room bulk temperature. This is consistent with the existing literature [114] which confirms that the initial removal of

[3] In addition to the agreement with literature, $\alpha_{OH,T}$ coincide with the surface concentration of Si atoms of β–cristobalite and β–tridymite (($\alpha_{Si,fi} = 4.55$) that are silica phases with refractive index close to the amorphous silica

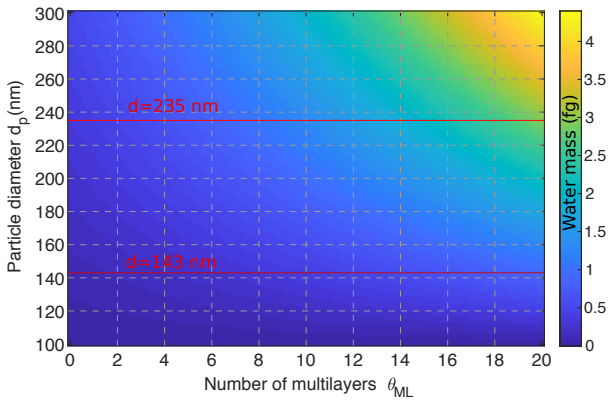

Figure 5.8: **Mass of water multilayer on the particle surface**. The water content on the particle's surface is calculated as a function of the number of multilayers of water molecules and of the particle's surface.

physically adsorbed water is achiavable by simple vacuum drying. According to the Zhuravlev model, this process is readily reversible upon the introduction of an excess of water. This was indeed verified in Fig. 5.3. The silanol coverage θ_{OH} remains unvaried, while $\theta_{\mathrm{H_2O}}$ decreases towards unity, i.e. only few layers of water molecules in an H-bond configuration. Due to furher decrease of the pressure, the light absorption overcomes the covective cooling rate and the bulk temperature start to increase [43]. As an explanation to the sudden drop in B, Ω_0 and m observed in Fig. 5.1, we believe that at $P = P_0 \in [10^{-2}, 10^{-1}]$ mBar the remaining few layers of physically adsorbed water molecules are abruptly desorbed. According to [43], the particle's temperature in this pressure regime is $T \sim 200$ °C. Interestingly, this temperature coincides with a threshold temperature $T_B = (190 \pm 10)$ °C introduced in the Zhuravlev model [114]. At $T = T_B$ the model predicts that the isothermic free energy of the free water ΔF, or in other words the binding strength A of the physically absorbed water on the surface) becomes equal to zero:

$$-\Delta F = A = RT \log\left(P_0/P\right) . \tag{5.4}$$

Concurrently, the kinetic order of desorption n varies abruptly from $n = 1$ to $n = 2$, and the activation energy of water desorption E_D also displays a rapid increase. Data demonstrating this phenomena has been shown in [114], and we report in Fig. 5.9 the corresponding adapted figures for clarity. The coefficients n and E_{a} shown describe the desorption rate:

$$\Gamma_{\mathrm{des}} = \nu e^{-E_a/k_B T} N^n . \tag{5.5}$$

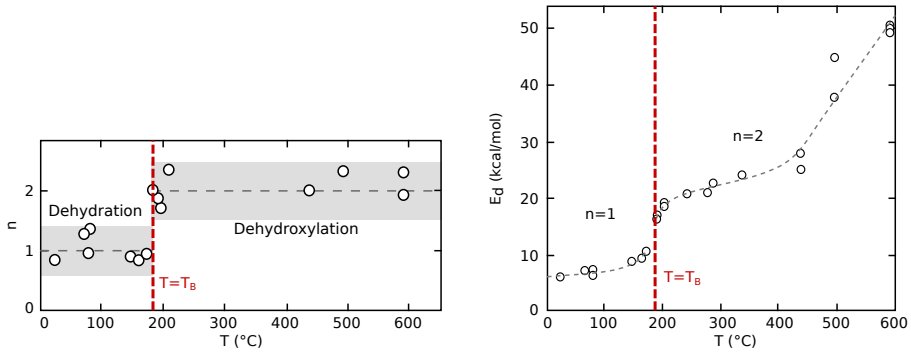

Figure 5.9: **Kinetic parameters as a function of temperature**

where ν, also called attempt frequency, represents the probability of an adsorbed molecule to overcome its potential barrier to desorption, while N is the concentration of the adsorbed material [102]. As a result, all the predictions and our observations seem to be consistent with the complete removal of physically adsorbed water at the end of STAGE 2 (i.e. for $T = T_B \simeq 190\ ^\circ\text{C}$).

Besides the satisfactory agreement established, the charge variation observed during this event is not yet fully understood. Some studies [101] report the so-called *protonation* as a surface charging process. This consists in the SiOH–H_2O bond rearranging in a dipolar complex of the form $SiO^- \cdots H_3O^+$. Therefore, stripping away the water termination would leave a negatively charged surface. This could only partially explain our measurements, where we often observe particles ending up with a positive net charge after the abrupt water removal. Also, the differing behavior observed between smaller ($d_p = 143$ nm) and bigger ($d_p = 235$ nm) particles remains unclear. A possible mechanism for differential particle charging can be conceived if we consider take into account the different solutions for the synthesis of the two types of particles: the impurities in suspension in each case, as well as pH conditions, are likely to be quite different. Therefore, after the removal of the water, some of these impurities could in principle remain adsorbed on the surface of the silica, thus determining a different final charge for the the two particle sizes. As we will discuss in § 7, this remains an open issue of high interest, both towards a comprehensive understanding of the system, and for the fields of silica surface chemistry and material science.

STAGE 3

After the abrupt event observed between $P = 10^{-1}$ and $P = 10^{-2}$ mBar, that according to our interpretations coincide with the system reaching the thresh-

old temprature $T_B \simeq 190$ °C, the particle surface is still in a maximum state of hydroxylation $\theta_{OH} \simeq 1$, but there is no presence of physically adsorbed water $\theta_{H_2O} = 0$. This state is often referred as the *dry SiO_2 surface*. Nevertheless, the presence of silanols of all types at the surface makes it possible for the particle to uptake H_2O molecules upon the introduction of an excess of water. Continuing to heat up the particle, silanols at the surface are removed, and the desorption of water becomes progressively more irreversible. The Zhuravlev model predicts that internal silanols are removed above $T = 900$ °C and that complete removal of all OH groups happens at the final threshold temperature $T = 1200$ °C. At this stage (final stage in Fig. 5.10) the surface is covered with only siloxanes bridges and becomes completely hydrophobic. We stress that this is the only fully irreversible stage in the surface chemistry of silica. However, the reverse processes of re-hydoxylation and re-hydration are extremely slow once the threshold temperature $T = T_B$ has been overcome. In fact, after the abrupt water-mass drop, we do not observe any trend similar to those reported in § 5.2.3. Even after leaving the particle trapped at ambient pressure for several consecutive days, we couldn't detect any variation of scattered intensity. Santamaria et al. [31] observed complete rehydroxylation and rehydration after leaving the particles immersed in distilled water for over two months. We therefore conclude that, in the experimental conditions were levitation experiments operate, the abrupt event can be considered fully irreversible although the silica has not achieved the hydrophobic state.

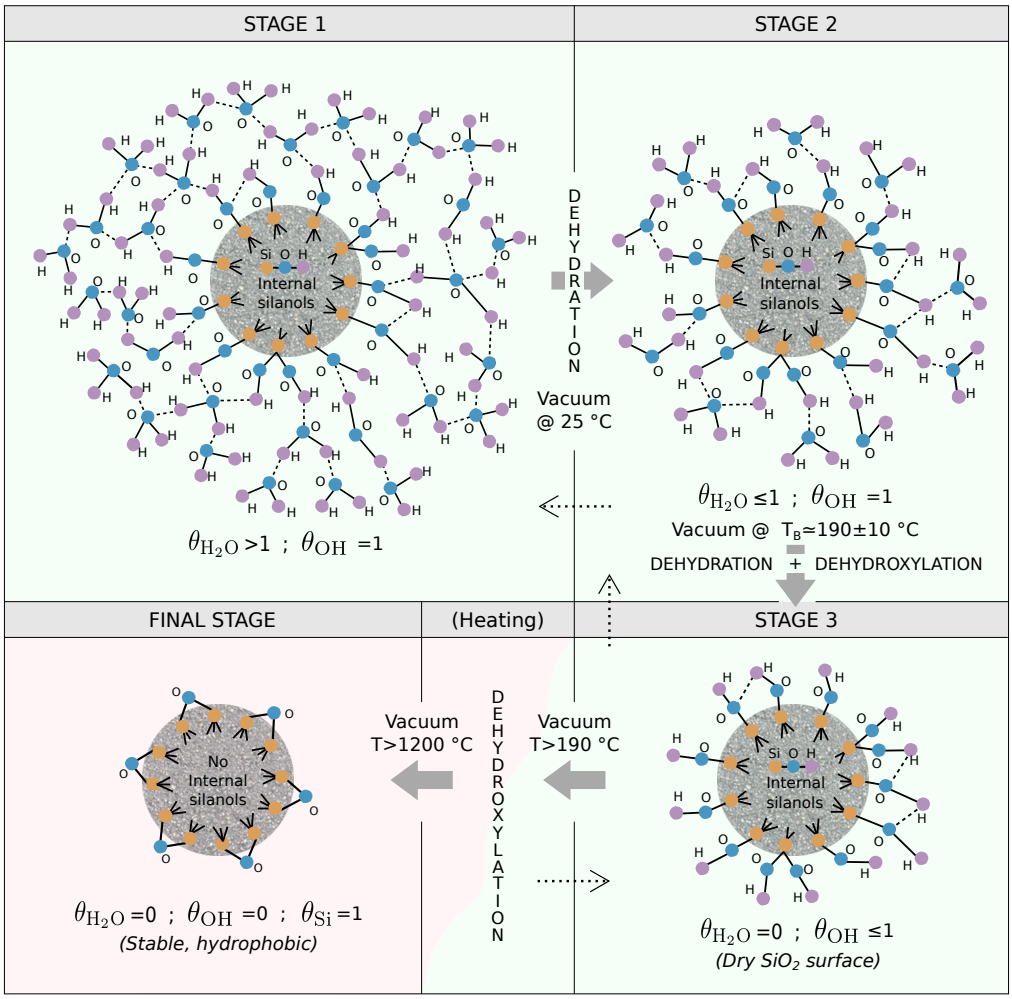

Figure 5.10: **The mass-loss model**. The observations of mass losses from the silica particle are compatible with the the amorphous surface chemistry model, called Zhuravlev model. The panels here shown represent different stages of the particle's evolution when brought to vacuum. STAGE 1 corresponds to the state of the particle right after loading it in the trap wile STAGE 2 and 3 represent the particle respectively before and after the abrupt event. The FINAL STAGE shown in the bottom left panel is the ultimate state of a calcined particle upon substantial heating. Dotted arrows correspond to reversible processes, while the green/red color coding indicates the stated that we are able to achieve with an optically trapped silica sphere. We stress that in our experiments, when particles are brought to high vacuum, they end up in an intermediate state between STAGE 2 and the FINAL STAGE which can nonetheless be considered indefinitely stable.

6

A model system for stochastic bistable dynamics

Contents

6.1 Introduction

Nano-mechanical resonators need to meet criteria of light mass and high-Q factor in order to maximize their performances when operated as linear

force transducers. However, these features lead to intrinsically nonlinear behaviour [36], with consequent vanishing dynamical range. To overcome this limitation, modern nanotechnology requires new sensing schemes that take nonlinearities into account and even benefit from them [109]. Many of the proposed solutions operate inside an instability region [2, 80] or close to a bifurcation point [53, 98], where the system ideally becomes infinitely sensitive. Others exploit fluctuations of noisy environments to trigger stochastic resonances [30] that amplify weak harmonic signals [4, 9, 108]. For all these sensing applications, a single nanoparticle optimally decoupled from the environment represents a particularly interesting system in the family of high-Q resonators.

In this chapter, we demonstrate full control on the linear, nonlinear (§ 6.3.1) and bistable dynamics (§ 6.4) of a levitated nanoparticle in high vacuum and under the effect of external noise (§ 6.3.2). The potential of our platform is validated by the implementation of two nonlinear amplification schemes: Stochastic Resonance (SR) [30] in § 6.5 and direct amplification via stiffness modulation in § 6.5.3. The unprecedented level of control achieved demonstrates the possible use of levitated nanoparticles as a model system for stochastic bistable dynamics with applications to a wide range of fields including biophysics [5, 41], chemistry [40, 99] and nanotechnology [76].

6.2 Experimental configuration and equation of motion

The experiments described in this section have been performed at a stage where the electrodes for the direct electrical driving, described in § 3.5, were not implemented yet. The experimental configuration used in the experiments presented in this chapter is sketched in Fig. 6.1a. The main optical trapping scheme, together with the particle's detection, have been extensively described in §3.2. Here, the central part of the experiment is played by the imprinted modulation on the laser intensity. The signal we feed to the EOM is obtained adding up:

1. the parametric feedback that cools the COM motion of the particle via nonlinear damping. The system is initialized activating the FB at a moderate vacuum with a pressure of $\sim$ 1 mBar, and then brought to $\sim 10^{-6}$ mBar.

2. the parametric driving that excites coherent oscillations and allows to explore the nonlinear features of the optical potential. This signal is

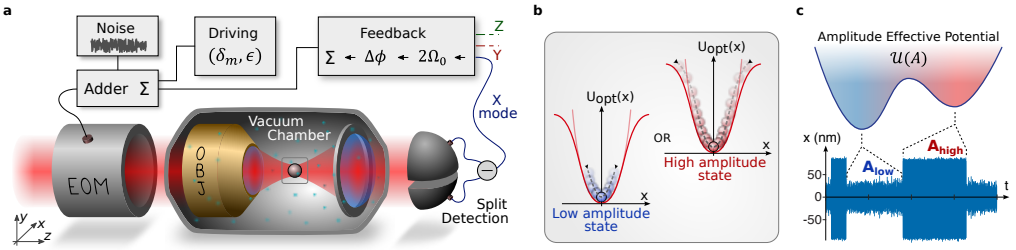

Figure 6.1: **Experimental set-up for parametric driving**. (a) A single silica nanoparticle is trapped inside a vacuum chamber by a tightly focused laser beam. Its motion is measured with a split detection scheme and parametric feedback is applied via an electro-optical modulator (EOM) in order to cool its center of mass motion. Likewise, an additional modulation at twice the the particle's oscillation frequency drives the latter into the nonlinear regime of the optical potential. The system can be modeled as a parametrically driven duffing resonator, and its amplitude response displays typical nonlinear features such as hysteresis and bistability. (b) In this regime, a low amplitude and a high amplitude oscillation states states coexist. (c) An effective amplitude bistable potential describes the probability of the two states and, when laser noise is injected via the EOM, the system displays interwell stochastic transitions (switching).

fully characterized by the modulation amplitude ϵ and the modulation frequency Ω_m of the driving signal.

3. a broadband Gaussian noise signal that heats up the particle and, under specific conditions, triggers the stochastic bistable dynamics of the system.

As a result the overall dynamics of the particle along driven mode can be described by the following equation of motion:

$$\ddot{x} + \left(\Gamma + \Omega_0 \eta x^2\right) \dot{x} + \Omega_0^2 \left[1 + \xi x^2 + \epsilon \cos\left(\Omega_m t\right)\right] x = \frac{\mathcal{F}}{m} \tag{6.1}$$

where η is the nonlinear (feedback-induced) damping coefficient, ξ is the Duffing term factor. Finally, the fluctuating force $\mathcal{F} = \mathcal{F}_{\text{th}} + \mathcal{F}_{\text{noise}}$ has two contributions. The first one, $\mathcal{F}_{\text{th}}$, represents the stochastic force arising from random collisions with residual air molecules in the chamber, while the second, $\mathcal{F}_{\text{noise}}$, represents the artificial noise that we add through the EOM.

6.3 Parametric control

In this section we will analyze the response of a parametrically driven levitated nanoparticle in vacuum. The theory of parametrically driven nonlinear oscillators is provided in § 2.2.2, and we will here compare such theory with experimental results.

6.3.1 Nonlinear dynamics at the first instability tongue

The particle response to the external parametric driving is fully characterized by measuring oscillation amplitude and frequency in the driving parameters phase space (δ_m, ϵ), where $\delta_m = \Omega_m/\Omega_0 - 2$ is the normalized detuning.

Substantially different dynamics can arise in the system depending on how close to the resonant condition $\Omega_m \approx 2\Omega_0$ is the modulation, and whether its strength is above or below the instability condition (2.102) :

$$\epsilon = \frac{2}{Q}\sqrt{1 + Q^2\delta_m}\,. \tag{6.2}$$

In the following we will mainly focus on the dynamics above threshold and inside of the instability tongue, where hysteresis and other bistable features are observable.

In order to simplify the problem we can neglect the stochastic term $\mathcal{F}(t)$ on the right-hand side of (6.1), since under typical experimental high vacuum conditions ($Q \gg 1$) is much weaker than the nonlinear terms and the parametric driving on the left. We are therefore left with a fully deterministic equation that can be solved using the *Slowly Varying Envelope Approximation*, which provides the amplitude response of the resonator. Full analytical derivation is provided in §2.2.2 and leads to the solution (2.106):

$$A^2(\delta_m, \epsilon; \eta, \xi) = \frac{1}{\eta\delta_{th}^2}\left[\frac{3\xi}{\eta}\delta_m + \frac{1}{Q} + \sqrt{\epsilon^2\delta_{th}^2 - \delta_m^2 + \frac{3\xi}{\eta}\frac{1}{Q^2}\left(2Q\delta_m - \frac{3\xi}{\eta}\right)}\right] \tag{6.3}$$

$$\approx \frac{1}{\eta\delta_{th}^2}\left[3\frac{\xi}{\eta}\delta_m + \sqrt{\epsilon^2\delta_{th}^2 - \delta_m^2}\right] \tag{6.4}$$

where $\delta_{th} = \sqrt{9\xi^2 + \eta^2}/2\eta$, and again the approximation made in (6.4) is valid for $Q \gg 1$. Notice that the oscillation amplitude q_0 expressed in (2.106) has been here renamed A for simplicity. We will adopt this convention throughout the whole chapter.

To experimentally measure the amplitude response of the resonator we sweep the modulation frequency across the resonant condition $\delta_m = 0$ (corresponding to $\Omega_m = 2\Omega_0$). This produces sideband components at frequencies $|\Omega_0 \pm \Omega_m|$, and leads to energy transfer from the sideband to the particle whenever the lower sideband $\Omega_m - \Omega_0$ is close to the particle resonance Ω_0. Two types of sweeps can be performed which lead to qualitatively different responses, i.e. the system displays hysterisis. In the following we provide a detailed description of the particle's response corresponding to these sweeps.

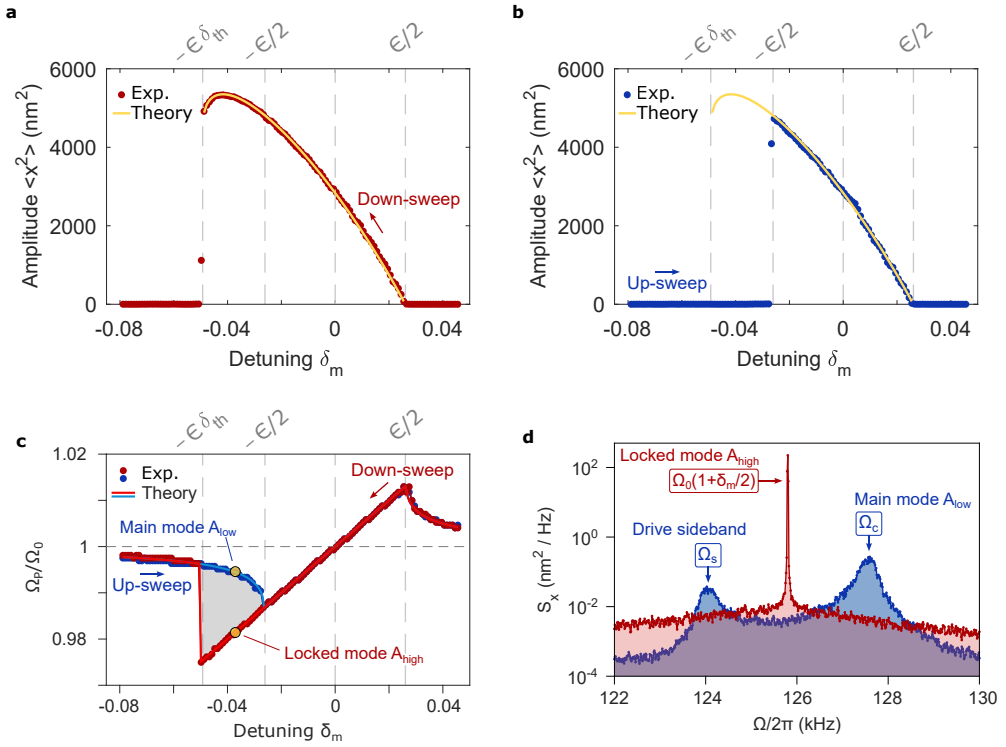

Figure 6.2: **Amplitude and frequency response to external parametric driving** (a) The oscillation amplitude (experimental dots in red) during a down-sweep of the the modulation frequency and (b) during an up-sweep (blue dots). The yellow solid line shows a fit to eq. (6.4), being η and ξ free parameters. $\delta_{\mathrm{m}} = \epsilon/2$, $-\epsilon/2$, and $-\delta_{\mathrm{th}}\epsilon$ represent particularly interesting points in the evolution of the dynamics (see main text). (c)The main oscillation frequency Ω_P shows a similar behavior to the amplitude, with a clear hysteresis observed when reversing the modulation sweep direction. We also observe frequency pulling phenomena at $\delta_{\mathrm{m}} = \epsilon/2$ and $\delta_{\mathrm{m}} = -\delta_{\mathrm{th}}\epsilon$. **(d)** Spectral features of the two stable oscillation modes. The low amplitude state (blue) is characterized by a carrier mode and a sideband, while the high amplitude state is locked to the external modulation at a frequency $\Omega_{\mathrm{m}}/2 = \Omega_0(1 + \delta_{\mathrm{m}}/2)$.

.

Frequency down-sweep When the modulation frequency is decreased across the resonance, the system behaves as depicted in Fig. 6.2a. The particle enters in the locked region for $\delta_m = \epsilon/2$, and the oscillation amplitude starts to increase according to equation (6.4). It reaches a maximum for $\delta_m^{max} = -\epsilon\delta_{th}/\sqrt{1+\eta^2/(9\tilde{\zeta}^2)}$, and decreases while approaching the left edge of the nonlinear instability region given by $\delta_m = -\epsilon\delta_{th}$. This condition identifies a saddle-node bifurcation point, where one of the two solutions of the secular equation of motion becomes unstable. As a result, the system *jumps* to the low-amplitude branch $\mathcal{A}_{low}$ which is not locked anymore to the external modulation and leaves the instability tongue.

Likewise, the oscillation frequency of the resonator follows a similar behavior, shown in Fig. 6.2c. A primary carrier component and a sideband can be found at

$$\Omega_{c,s} = \Omega_0 \left[1 + \frac{\delta_m \mp \sqrt{\delta_m^2 - (\epsilon/2)^2}}{2}\right] \tag{6.5}$$

with $\mp$ corresponding to carrier (c) and sideband (s) respectively (see Fig. 6.2d). Therefore, far from the instability tongue ($\delta_m \gg \epsilon/2$), the resonator maintains its main frequency component at $\Omega_c \approx \Omega_0$. Approaching the $\delta_m = \epsilon/2$ condition, the particle undergoes the phenomenon of frequency pulling [55]: the sideband *pulls* the oscillation to a new primary carrier component with pulled frequency given by (6.5), i.e: $\Omega_c = \frac{\Omega_m}{2} - \frac{1}{2}\sqrt{(\Omega_m - 2\Omega_0)^2 - \Omega_0^2(\frac{\epsilon}{2})^2}$. Once the instability tongue is reached the particle locks to the external modulation and maintains its frequency at $\Omega_m/2$ until the bifurcation at $\delta_m = -\epsilon/\delta_{th}$ is reached. Below this point the motion features again the carrier and the sideband components, and the former smoothly goes back to the eigenfrequency Ω_0.

Frequency up-sweep When the sweep crosses the resonance starting from negative detuning δ_m towards a positive one, the resonance curve is different from the down-sweep case (see Figs. 6.2b,c). In particular, the particle remains unlocked for detunings $-\delta_{th}\epsilon < \delta_m < -\epsilon/2$ with low oscillation amplitude $\mathcal{A}_{low}$. A second saddle-node bifurcation is encountered at $\delta_m = \epsilon/2$, and only here the system switches abruptly to the high amplitude state $\mathcal{A}_{high}$, locking to the external modulation. For $\delta_m > -\epsilon/2$ it continues following the high amplitude branch given in (6.3) until $\delta_m = 2\epsilon$, the mode is pulled a bit further according to (6.5) and finally separates again into into carrier and sideband, with the particle going back to its initial state oscillating at the eigenfrequency Ω_0.

The dynamics of up- and down-sweeps can be generalized for increasing

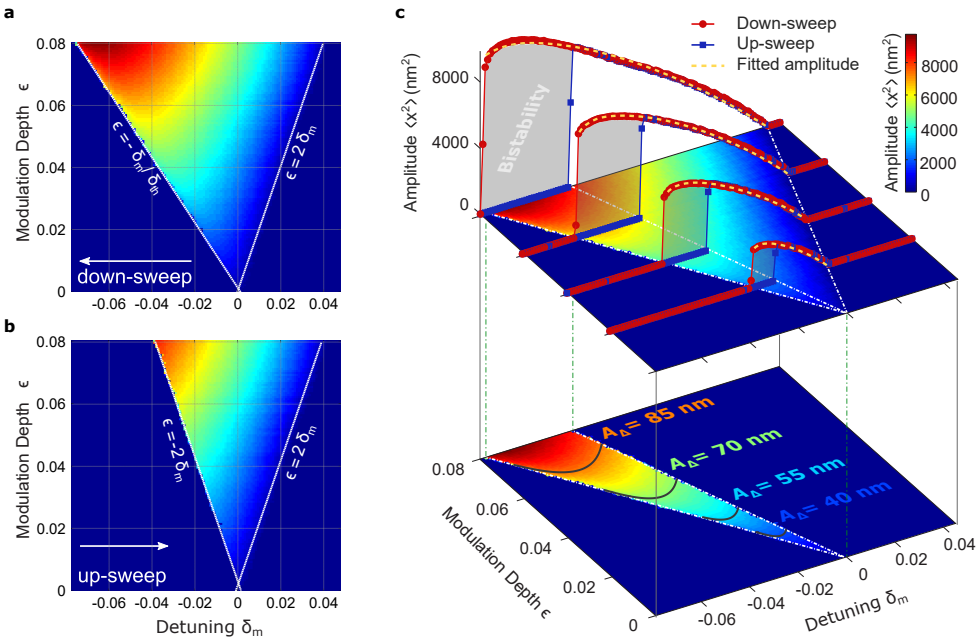

Figure 6.3: **Amplitude response in the (δ_m, ϵ) parameters phase space.** (a) When down-sweeping the detuning δ_m for increasing values of modulation depth ϵ, the amplitude response spans a triangular region corresponding to the first instability tongue [62]. The left edge of this region extends up to $\epsilon = -\delta_m/\delta_{th}$ due to the nonlinear terms. (b) In the opposite case of a frequency up-sweep, however, the system displays hysteresis, and the tongue results narrower, symmetric, and limited by $\epsilon = |2\delta_m|$.(c) A combination of these two maps, together with crosscuts for constant ϵ that are fitted by eq. 6.4. The bistable regime is identified in the parameters space by subtracting the up-sweeps map from the down-sweeps ones. Solid lines correspond to the iso-amplitude lines described by (6.8).

modulation depths ϵ. The emerging 2-D maps are shown in Fig. 6.3a,b respectively.

Iso-amplitude lines

Figure 6.3c shows a combination of up- and down-sweeps of the modulation frequency. The cross-cuts in the top map illustrate the 2-dimensional surface in the (δ_m, ϵ, A) space that corresponds to the amplitude response of the trapped particle. The bistable regime in the lower map appears by subtracting the up-sweep map from the down-sweep one. In order to introduce the bistable potential model that we will use in the following sections, it is interesting now to focus on the amplitude trend inside the bistable regime. In particular, it is instructive to analytically determine the subset of the driving parameters space that leads to a constant amplitude gap $\mathcal{A}_\Delta = \mathcal{A}_{high} - \mathcal{A}_{low}$. Noting that

$\mathcal{A}_{\text{high}} \gg \mathcal{A}_{\text{low}}$ over the whole bistable regime, we can simplify this condition into:

$$A^2(\delta_m, \epsilon) = \mathcal{A}_\Delta^2 \quad \rightarrow \quad \frac{1}{\eta\delta_{th}^2}\left[3\frac{\xi}{\eta}\delta_m + \sqrt{\epsilon^2\delta_{th}^2 - \delta_m^2}\right] = \mathcal{A}_\Delta^2 \tag{6.6}$$

$$\rightarrow \quad \sqrt{\epsilon^2\delta_{th} - \delta_m^2} = \frac{1}{\eta}\left[\mathcal{A}_\Delta^2\eta^2\delta_{th}^2 - 3\xi\delta_m\right] \tag{6.7}$$

$$\Rightarrow \quad \epsilon(\delta_m) = \left[\left(1 + \frac{9\xi^2}{\eta^2}\right)\frac{\delta_m^2}{\delta_{th}^2} - 6\xi\mathcal{A}_\Delta^2\delta_m + \eta^2\delta_{th}^2\mathcal{A}_\Delta^4\right]^{1/2} \tag{6.8}$$

Equation (6.8) defines the so called *Iso-Amplitude* lines: a subset of the bistable parameter space where the two oscillation states remain equally separated. These lines are displayed in the bottom map of Fig. 6.3c for different values of $\mathcal{A}_\Delta$ and demonstrate perfect agreement with the experimental data shown by the color gradient. The observed trend is also shown in the analytical solution plotted in Fig. (2.7).

6.3.2 Particle response to external parametric noise

Inside the bistable region, natural thermal noise can activate spontaneous transitions between low- and high-amplitude states. However, in high vacuum and with parametric feedback activated, these events are extremely rare. Thus, in order to observe stochastic activation within a reasonable time the particle needs to be heated up by additional external noise. As depicted in Fig. 6.1a, we do so with a function generator that creates a noise signal $\zeta(t)$ of variable amplitude N_V, which is sent to the pockels cell (EOM) and results in a parametric noise of the form $\mathcal{F}_{\text{noise}} \propto N_V\zeta(t)x$. Noise calibration can be performed by measuring the particle's oscillation amplitude A in the absence of parametric driving [68]. Figure 6.4a shows the mean amplitude $\mathcal{A} = \langle A\rangle_\mathcal{T}$ together with its standard deviation as a function of N_V. The response of the noise-driven particle clearly shows the presence of two regimes. At low noise levels the noise injected does not affect the particle's dynamics, which is still dominated by the thermomechanical noise of the environment. However when noise in sufficiently high (N_V above few hundreds mV), the particle's amplitude starts to increase and so does the corresponding standard deviation. We can model the observed behavior assuming an effective temperature $T_N = \frac{m\Omega_0^2 < x^2 >}{k_B}$ given by the total noise in the system. We finally extract the noise calibration by fitting the trend with a power law that, in the regime of noise levels where we will operate, is found to be $T_N \propto N_V^{1.47}$. This relation will be used from now on to address the noise level with its effective temperature.

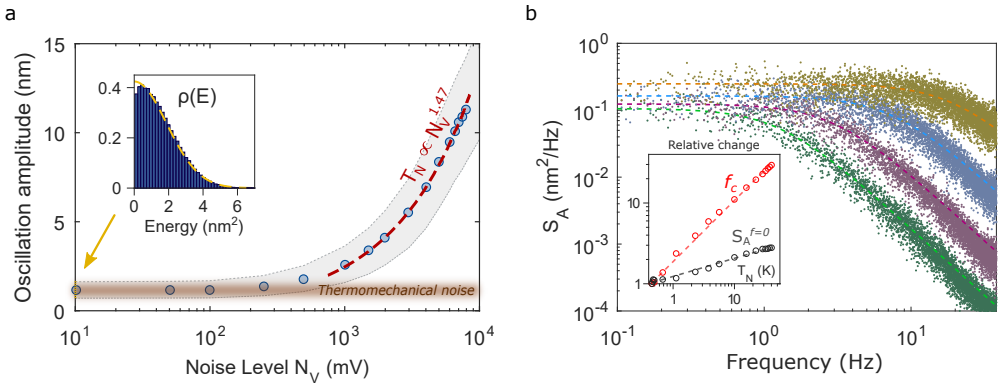

Figure 6.4: **Particle response to external noise** (a), When injecting noise in intensity of the laser, the particle's oscillation amplitude increases (blue dots), together with its standard deviation (shaded area). Converting amplitudes into effective temperatures one can map noise levels into noise temperatures and extract a power law calibration curve. The inset shows the energy distribution predicted by (6.9) when the particle is solely subjected to thermal noise. (b), The particle's amplitude power spectral density for different noise levels shows an overdamped behavior. The corner frequency and the plateau height depend on the noise temperature and their trend is presented in the inset figure.

The inset of Fig. 6.4a shows the energy distribution $\rho(E)$ in the absence of external noise, calculated from an ensemble of 10^5 amplitude (or equivalently energy) measurements. The data is fitted with the analytical prediction of $\rho(E)$, which reads [34]:

$$\rho(E) \approx \exp\left[-\beta\left(E + \frac{\eta}{4m\Omega_0\Gamma}E^2\right)\right], \tag{6.9}$$

where $\beta = 1/(k_B T)$, T being the bath temperature. It is remarkable, here, that Γ is the only free parameter in the fit (η being known from the nonlinear response in the instability tongue, see Fig. 3.8 and 6.3). Therefore, this measurement can be an equivalent method for determining the natural quality factor $Q = \Omega_0/\Gamma$ in the presence of feedback and avoiding the more complex 'ring-down' measurement that should be repeated several times to average the energy fluctuations [37]. In the specific case the fit yields a natural linewidth of $\Gamma/2\pi \simeq 1.1$ mHz, and a corresponding quality factor of $Q \simeq= 1.2 \times 10^8$.

Tracking the time evolution of the amplitude also provides information about its spectral properties. In the absence of coherent driving one finds that the oscillation amplitude behaves as an overdamped variable, in spite of being the result of the average over a fast (underdamped) oscillating variable [38]. This behaviour is depicted in Fig. 6.4b where the amplitude power spectral density S_A is shown for different effective noise temperatures. We

fit the measured power spectral densities (PSDs) with a typical overdamped Lorentzian $S_A = S_0 \frac{f_c^2}{f^2+f_c^2}$ where $S_0 = S_A(f = 0)$ is the height of the plateau and f_c is the corner frequency. The inset shows the power law dependency of these fitting parameters (in terms of relative change with respect to the no-injected-noise case) as a function of noise temperature. As expected, the low-frequency plateau raises with the noise intensity, in agrement with the observation in Fig. 6.4a [65,68]. Interestingly, the corner frequency also increases with the injected noise, leading to a larger bandwidth of amplitude fluctuations. This effect is likely to be related to the multiplicative nature of noise after the EOM [110]. Let us stress that the findings of this section, especially referring to Fig. 6.4b, are essential to justify our modeling of the particle's dynamics in the bistable regime as a fictitious overdamped particle moving in an effective bistable potential. This model is further detailed in the next section.

6.4 Noise activated switching in the bistable regime

6.4.1 Effective potential shaping

The stochastic switching dynamics of the levitated nanoparticle is investigated via the injection of noise. Figure 6.5a illustrates position and amplitude time traces corresponding to few switching events and emphasizes the remarkable ability of our tracking scheme to resolve considerably different time scales. Interestingly, we can even observe the fast dynamics of the particle during a switching event, observing that the transition from one state to the other is a process that takes a significant number of particle's oscillations. The amplitude probability distribution $\rho(A)$, obtained by analysing the particle trajectory over approximately one minute, is show in Figure 6.5b. Even though the particle is in a non-thermal state due to the applied parametric control [37], we introduce a simplified model that describes the dynamics of its amplitude as the motion of a thermal *fictitious* particle in a double well potential. This justifies the use of the Boltzmann-Gibbs distribution:

$$\rho(A) \propto \exp\left[-\frac{\mathcal{U}(A)}{k_B T_N}\right], \tag{6.10}$$

and allows us to retrieve the amplitude effective potential $\mathcal{U}(A)$ that models the bistable dynamics:

$$\mathcal{U}(A) = -k_B T_N \ln\left[\rho(A)\right] + \mathcal{U}_0 \tag{6.11}$$

where $\mathcal{U}_0$ is a constant offset that we can set at will in order to have $\mathcal{U}(\mathcal{A}_{un}) = 0$, $\mathcal{A}_{un}$ being the amplitude of the unstable equilibrium. SOme

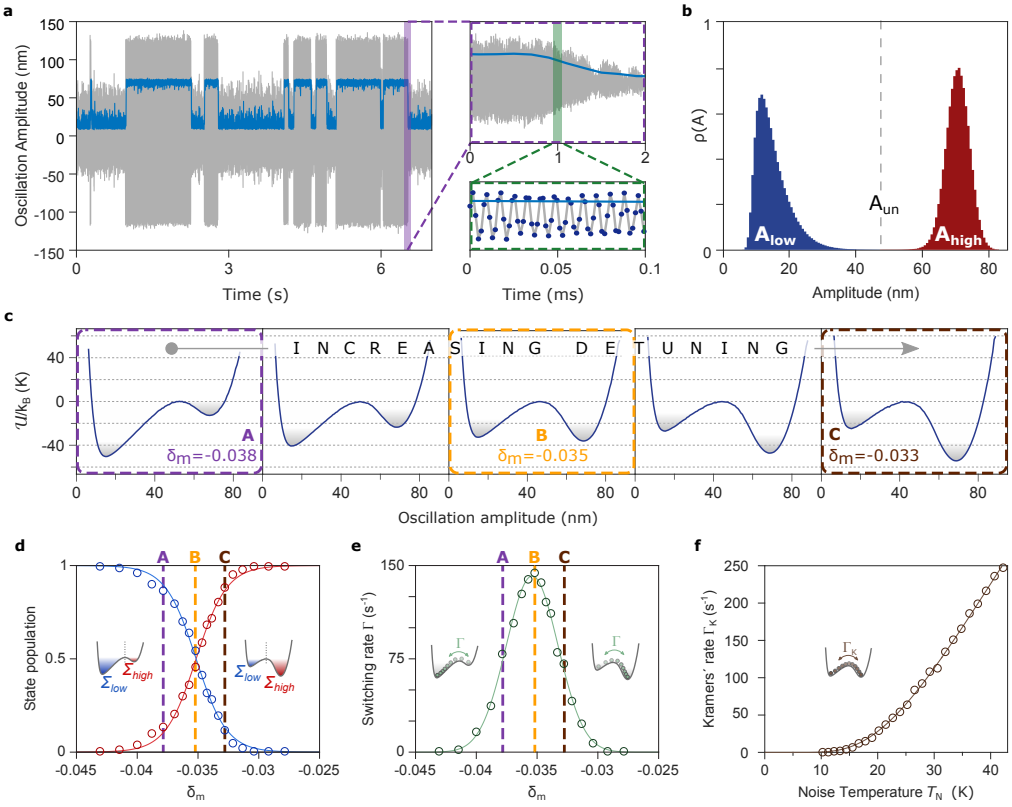

Figure 6.5: **Stochastic switching dynamics and effective potential shaping.** (a), Position time trace (grey) and corresponding amplitude (blue) reveal a typical bistable behaviour of the system, with randomly distributed stochastic switches between the two stable oscillation states. The distinctive trait of our system is to be able to follow the dynamics of the overdamped variable down to very short time scales (insets) and therefore control the dynamics with high accuracy. (b) A histogram of the amplitude distribution featuring two fully separated amplitude states from which the effective potential $\mathcal{U}(A)$ can be retrieved by inverting the Boltzmann-Gibbs distribution. (c) With ad-hoc tuning of the driving parameters (δ_m, ϵ) the potential can be finely shaped. For the dynamics here shown one expects a state population inversion and a maximization of the transition rate as shown in (d) and (e) respectively, where points A, B and C correspond to the marked potentials in (c). (f) Transition rate as a function of noise injected for the symmetric potential case. Solid line is a fit to Kramers' law, which yields $\Gamma_0 = (1814 \pm 96)\ \mathrm{s}^{-1}$ and $\Delta\mathcal{U}/k_B = (83 \pm 2)\ \mathrm{K}$.

examples of this effective potential are given in Fig. 6.5c. The high stability of the system allows us to continuously modify this probability distribution, and hence to engineer almost at will the shape of $\mathcal{U}(A)$ following any path inside the bistable regime. As previously mentioned in § 6.3.1, an interesting case consists in the so called *iso-amplitude* lines: paths along which the amplitude gap $\mathcal{A}_\Delta = \mathcal{A}_{\text{high}} - \mathcal{A}_{\text{low}}$, is kept constant. These particular subsets of the phase space are generally blurred by the frequency noise of the resonator, but clearly visible in our system thanks to the low frequency fluctuations (see Fig. 6.3c). By following an iso-amplitude line with a fixed $\mathcal{A}_\Delta$, we obtain a very smooth evolution of the effective potential (see Fig. 6.5c). As we show in Fig. 6.5c, starting from an asymmetrically tilted configuration, the potential progressively undergoes an inversion of its shape, passing through a quasi-symmetric condition where the potential barrier determines equal depth of the two wells. It is important to stress that, upon this *ad-hoc* dynamical sweep of ϵ and δ_m, the two minima of the potential corresponding to the amplitudes $\mathcal{A}_{\text{high}}$ and $\mathcal{A}_{\text{low}}$, maintain their position fixed. Clearly, this would not be the case when following any other path, for example moving along $\epsilon = \text{const.}$ lines (see cross-cuts in Fig. 6.3c).

Once the amplitude distribution $\rho(A)$ is determined for a certain set of parameters $(\delta_\text{m}, \epsilon; T_N)$, we can derive the state populations as:

$$\Sigma_{\text{low}} = \frac{1}{\Sigma}\int_0^{\mathcal{A}_{\text{un}}} \rho(A)\mathrm{d}A \qquad ; \qquad \Sigma_{\text{high}} = \frac{1}{\Sigma}\int_{\mathcal{A}_{\text{un}}}^{\infty} \rho(A)\mathrm{d}A\,, \tag{6.12}$$

being $\Sigma = \int_0^\infty \rho(A)\mathrm{d}A$ a normalization factor. Their evolution as a function of the detuning is shown in Fig. 6.5d, and display an inversion consistent with the potential dynamics observed in Fig. 6.5c. Solid lines are *sigmoid* fits to the experimental data, of the form:

$$\sigma_{\text{low}}(\delta_\text{m}) = 1 - \frac{1}{1+e^{-(\delta_\text{m}-\delta_\text{m}^*)/\tau}} \qquad ; \qquad \sigma_{\text{high}}(\delta_\text{m}) = \frac{1}{1+e^{-(\delta_\text{m}-\delta_\text{m}^*)/\tau}} \tag{6.13}$$

where δ_m^* and τ are free fitting parameters. The former represents the detuning at which we find a symmetric potential configuration inside the bistable tongue, while the latter corresponds to the effective width of the bistable regime.

Similarly, the overall switching rate Γ_{sw} also depends significantly on the detuning (see Fig. 6.5e). The extremely biased configurations of the potential found at the edges of the bistable region do not enable almost any switch within the duration of the experiment. We therefore have $\Gamma_{\text{sw}} \approx 0$ for high absolute detunings $|\delta_\text{m}|$, while we encounter a maximum corresponding to

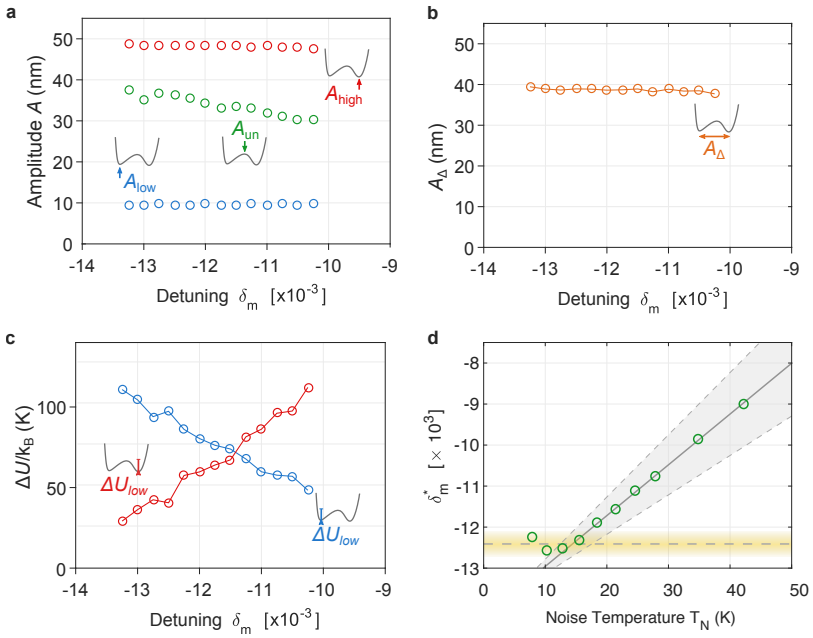

Figure 6.6: **Symmetric potential configuration measurement**. (a) Amplitude states $\mathcal{A}_{\text{low}}$, $\mathcal{A}_{\text{high}}$ and $\mathcal{A}_{\text{un}}$ as a function of the scanned detuning. (b) Over a narrow region of the bistable regime, the amplitude gap $\mathcal{A}_\Delta$ remains constant. (c) Potential barrier height for $\mathcal{A}_{\text{low}} \rightarrow \mathcal{A}_{\text{high}}$ (blue) and $\mathcal{A}_{\text{high}} \rightarrow \mathcal{A}_{\text{low}}$ transitions (red). (d) Similarly to what shown in Fig. 6.5d, state populations Σ_{low} and Σ_{high} invert at the symmetric configuration δ_{m}^*. As a result, fitting with sigmoid functions $\sigma_{\text{low}}(\delta_{\text{m}})$ and $\sigma_{\text{high}}(\delta_{\text{m}})$ (see eq. 6.13)provides information on the position δ_{m}^* of the symmetric configuration and on the width τ of the bistable regime, respectively plotted in (c) in green circles and gray shaded area. The solid line is a linear fit used to compensate for symmetry drift at high noise levels.

the symmetric potential configuration $\delta_{\text{m}} = \delta_{\text{m}}^*$, as predicted by Kramers' theory [93].

A closer look at the effective potential shape in the proximity of this symmetric configuration is shown in Fig. 6.6. More precisely, Fig. 6.6a confirms that the two states $\mathcal{A}_{\text{high}}$ and $\mathcal{A}_{\text{low}}$ maintain their value fixed along the amplitude axis. The only change we observe concerns the position of the unstable state $\mathcal{A}_{\text{un}}$, which due to the population inversion undergoes a shift of $\sim 20\%$ of the whole amplitude separation between the two stable states. Similarly, $\mathcal{A}_\Delta$ remains unvaried as shown in (6.6)b. Finally, the potential barrier shown 6.6c also displays a crossing dynamics, in agreement with the state population previously observed. This type of characterization needs to be repeated whenever the noise level T_N injected in the system is varied. In fact, it allows to know the exact position of the symmetric condition δ_{m}^* and to compensate for possible noise-induced drifts of this latter.

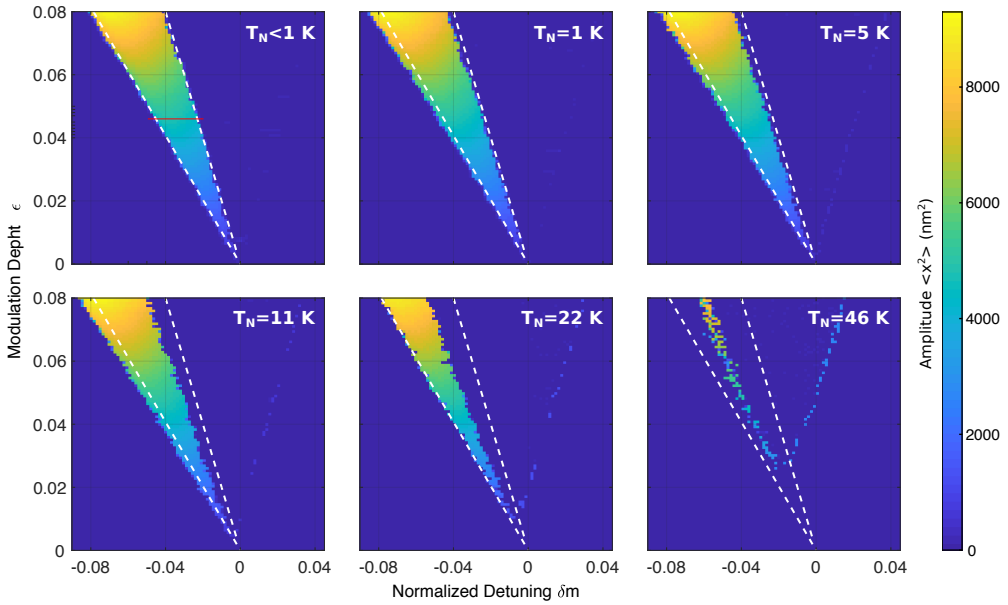

Figure 6.7: **Hysteresis quenching for increasing noise levels**. The hysteretis regime is shown at the indicated effective temperatures. For increasing noise levels the instability tongue becomes narrower, according to the phenomenon of hysteresis quanching [3, 108].

6.4.2 Hysteresis quenching and noise induced effects

Figure 6.3c clearly shows that in the absence of externally injected noise, the bistability region has a well defined triangular shape described by

$$\epsilon > -\delta_{\rm m}/\delta_{\rm th} \quad \wedge \quad \epsilon < -2\delta_{\rm m} \tag{6.14}$$

However this regular shape gets affected when noise in the system is increased above a critical threshold, according to a phenomenon sometimes called *hysteresis quenching* [3]. Here we first observe and quantify this phenomenon in our bistable system, and then use the findings of the previous sections to give a probabilistic description in terms of the bistable effective potential.

Figure 6.7 shows the bistability region for increasing levels of noise. White dotted lines correspond to the edges of this region in the approximation $T_N = 0$, and are meant to guide the eye through the changes of the system response. At $T_N = 0.36 \simeq 0$ all data fit inside the expected region. At temperatures of $T_N = 1$ to 5 K the noise has still small effects on the system: the hysteretic regime preserves its size, and only a slight shift towards smaller values of $\delta_{\rm m}$ is observed. For $T \gtrsim 10$ K more drastic effects are visible, with the hysteresis region greatly reduced, and almost disappearing for $T_N \simeq 50$ K.

This observation can be interpreted recalling the effective amplitude po-

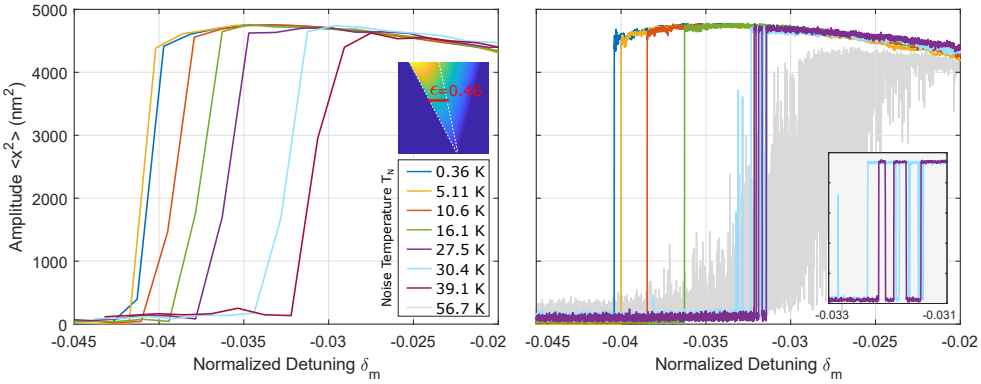

Figure 6.8: **Hysteresis quenching at different sweeping speeds**. (a) A fast sweep of the detuning shows that for increasing noise temperatures the transition from $\mathcal{A}_{\text{high}}$ to $\mathcal{A}_{\text{low}}$ takes place at progressively higher δ_{m}, in agreement with the tongue reduction described in Fig. 6.7. (b) Reducing the speed of the sweep, and for sufficiently high noise, we start observing recrossing events that repopulate the instability tongue. This suggests a probability interpretation of the phenomenon of hysteresis quenching.

tential introduced in § 6.4.1 and comparing fast with slow modulation frequency sweeps. Figure 6.8a shows the oscillation amplitude for a fast frequency down-sweep through the bistable regime. The frequency change is realized at a rate of $R_{\text{fast}} \simeq 11.6$ kHz/s. The behavior shown is compatible with that of Fig. 6.7. We indeed observe a reduction in the size of the bistable regime for increasing T_N the left edge of the hysteretic regime shifts towards $\delta_{\text{m}} > 0$ for increasing T_N. In this case the dynamical modulation of the effective potential is fast enough to prevent recrossing events after the system has performed the transition from $\mathcal{A}_{\text{high}}$ to $\mathcal{A}_{\text{low}}$. Similar behavior is observed for low noise when repeating the sweep at a lower speed $R_{\text{slow}} \simeq 30.5$ Hz/s (see Fig. 6.8b). However already at $T_N \simeq 30$ K, the system starts to perform multiples recrossing events when approaching the symmetry condition, for which the noise allows to overcome the potential barrier separating the two states. This is clearly shown in the inset of Fig. 6.8b for $T_N = 27.5$ K and $T_N = 30.4$ K. For extremely high noise $T_N \gtrsim 50$ K, these recrossing events are faster than our amplitude-tracking scheme,which is unable to follow the full transitions. As a result, fictitious points appear at $\mathcal{A}_{\text{low}} < A < \mathcal{A}_{\text{high}}$ as an average between $\mathcal{A}_{\text{high}}$ and $\mathcal{A}_{\text{low}}$, weighted by the corresponding probability given by the depth of the potential. Thus, we conclude that the timescale relation between the the potential modulation and the switching rate Γ_{sw} (given by the noise in the system), determines the shrinking of the bistable regime reported in Fig. 6.7.

The observation of noise-induced changes in the shape of the hysteretic regime poses the question whether the symmetry condition $\delta_{\mathrm{m}} = \delta^*_{\mathrm{m}}$ is also affected by an increase of the noise in the system. It is clear from Figs. 6.5d,e that an asymmetric potential quenches the switching rate for a given noise level due to to the difference between the barrier heights ΔU_{low} and ΔU_{high} respectively associated to the transitions $\mathcal{A}_{\mathrm{low}} \to \mathcal{A}_{\mathrm{high}}$ and $\mathcal{A}_{\mathrm{high}} \to \mathcal{A}_{\mathrm{low}}$.

The drastic effects of hysteresis quenching can in fact prevent the observation of stochastic resonance [108] as a consequence of drifts in the symmetry condition. An asymmetrical potential would lead to to different resonant conditions for the $\mathcal{A}_{\mathrm{high}} \to \mathcal{A}_{\mathrm{low}}$ and for the $\mathcal{A}_{\mathrm{low}} \to \mathcal{A}_{\mathrm{high}}$ transition. A fine characterization of the potential shape for increasing noise, and in particular of its symmetric configuration, is therefore of utmost importance. We do so by repeating the measurements shown in Fig. 6.6a-c for a fixed $\epsilon = \epsilon^*$ and for increasing T_N, determining each time symmetry detuning δ^*. The evolution of this latter is shown in Fig. 6.6d. Again, for low levels of noise, the potential symmetry is not affected. However, for $T_N \gtrsim 15$ K we detect a drift towards higher detunings, which can be fitted linearly in the regime of noises used in the experiment. This allows us to adjust the driving parameters $(\delta^*_{\mathrm{m}}, \epsilon^*)$ for each different noise value, therefore following the symmetry condition and preventing the system to escape from the bistable regime.

6.4.3 Kramer's rate

Figure 6.9 shows a typical bistable potential $\mathcal{U}$ as a function of its general coordinate x. *Reaction Rate Theory* predicts the interwell transition rates Γ_{ac} and Γ_{ca} between the two stable states A and C (local minima of the potential) as:

$$\Gamma_{\mathrm{ac}} = \frac{\omega_{\mathrm{a}}\omega_{\mathrm{b}}}{2\pi\gamma} e^{-\frac{E_{\mathrm{ab}}}{k_B T}}, \tag{6.15}$$

where $\omega_i = \sqrt{U''(x_i)}$, $E_{ib} = |\mathcal{U}(x_i) - \mathcal{U}(x_{\mathrm{b}})|$ for $i = a, c$. γ and T are respectively the damping and the bath temperature. The inverse rate Γ_{ca} is obtained by swapping the indexes a and c.

For a symmetric configuration, we have $\Gamma_{\mathrm{ac}} = \Gamma_{\mathrm{ca}}$, and using the equivalent bath temperature T_N, eq. (6.15) simplifies into the Kramers' rate:

$$\Gamma_K = \Gamma_0 \, e^{-\frac{\Delta\mathcal{U}}{k_B T_N}}. \tag{6.16}$$

The adjusted detuning $\delta^*_{\mathrm{m}}(T_N)$ allow us to maintain this symmetric configuration, and therefore to experimentally verify the prediction of Kramers' law. Figure 6.5f shows the switching rate as a function of injected noise, with a fit

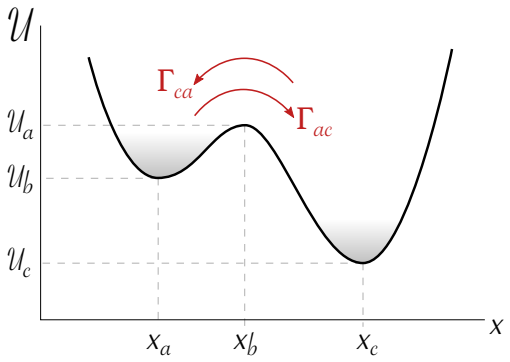

Figure 6.9: **Bistable potential**. A general bistable potential features minima at x_a and x_c (stable equilibrium) and a relative maxima at x_c (unstable equilibrium). Transition rates Γ_{ab} and Γ_{ba} between these states are predicted by Kramers' rate theory (6.15). In our measurements we verified the symmetric potential case given by (6.16).

according to eq. (6.16) that shows excellent agreement with the experimental trend.

6.5 Stochastic Resonance

Once the static potential $\mathcal{U}(A)$ has been fully characterized for different sets of parameters (δ_m, ϵ) and for increasing noise temperatures T_N, we can now study the system response to a dynamic (i.e. modulated in time) effective potential. These conditions can trigger the phenomenon of Stochastic Resonance (SR) [30]. In a nutshell, a weak periodic perturbation in the system induces a modulation of the potential barrier separating the two stable states. Whenever the interwell transition rate Γ_{sw} matches twice the frequency of the perturbation, the system displays an overall synchronized (i.e. quasi-coherent) switching dynamics between $\mathcal{A}_{high}$ and $\mathcal{A}_{low}$. Now, given that the rate Γ_{sw} depends monotonically on the amount of noise in the system, SR turns into a noise-induced rise (and then fall) of the external perturbation's signal-to-noise ratio (SNR). As a result, this phenomenon can in principle be exploited to amplify a narrow-band signal in a nonlinear system under appropriate conditions.

6.5.1 Amplitude modulation

A modulation in the driving parameters is introduced in order to mimic an external perturbation on the system. In the case of amplitude modulation we have:

$$\epsilon(t) = \epsilon^* \left[1 + \chi_{AM} \cos(\tilde{\omega} t)\right] \quad , \quad \delta_m = \delta_m^*. \tag{6.17}$$

Here, ϵ^* and δ_{m}^* are the set of parameters that ensure symmetry of the effective potential. Note that, as described in § 6.4.2, these set of parameters are actually a function of the noise temperature T_N: $\delta_{\mathrm{m}}^* = \delta_{\mathrm{m}}^*(T_N)$; $\epsilon^* = \epsilon^*(T_N)$. This dependency avoids the escape from the bistable region as a consequence of hysteresis quenching [3, 108], which in turn would prevent the observation of the full SR curve when noise is increased. The modulation strength χ_{AM} is an adimentional parameter that, in the experiment performed takes the values $\chi_{\mathrm{AM}} = (5, 25, 50) \times 10^{-3}$. However, knowing the modulation depth ϵ^* and the stiffness of the trap $k = m\Omega_0^2$, those values can be converted into physical force units, and correspond to force modulations of ten to hundreds atto-Newton.

To observe the SR phenomenon we record long amplitude time traces $A(t)$ ($\sim 10^3$ s) and compute their power spectral densities $S_A(\omega)$ for increasing levels of noise T_N. Figure 6.10 shows the complete response of the system: at $T_N \sim 10$ K (point marked A) switching events are only partially correlated with the modulation signal (see Fig. 6.10b). Instead, when noise is increased to $T_N \sim 16K$ (point B) the system clearly exhibits an overall synchronization. A spectral analysis of the corresponding amplitude trace shows that S_A features an extremely sharp peak precisely at $\tilde{\omega}/2\pi = 1$ Hz (see inset in Fig. 6.10a). Although SR phenomena ultimately describe the resonance in the SNR of the detected modulation, it is interesting to track the evolution of both the spectral amplification G (signal) and noise floor N (noise). As expected by looking at the time traces in Fig. 6.10b, the spectral amplification G first increases, reaching a maximum for the most synchronized dynamics, and then falls back to zero when noise is further increased and destroys the coherence of the system. Interestingly, a similar and counterintuitive behavior is observed in the noise floor N, which presents a non-monotonic trend due to a redistribution of noise intensity towards higher frequencies. The overall evolution of $SNR = G/N$ is shown in Fig. 6.10c for the different values of χ_{AM}, and fitted with the linear perturbation theory of stochastic resonance [30], that predicts:

$$SNR = \pi \left(\frac{\chi \mathcal{A}_\Delta}{T_N} \right)^2 \Gamma_0 \exp\left(-\frac{\Delta \mathcal{U}}{k_B T_N} \right) + \mathcal{O}(\chi^4), \tag{6.18}$$

where χ is the amount of modulation of the potential, proportional to the experimental value of χ_{AM}. The fits display very good agreement with the experiment. Moreover, the ratios of the fitted modulation depths $(2 : 5.4 : 11)$ are also in good agreement with the expected ratios $(2 : 5 : 10)$ used in the experiment, remarking once again the quality of the modeled bistable dynamics.

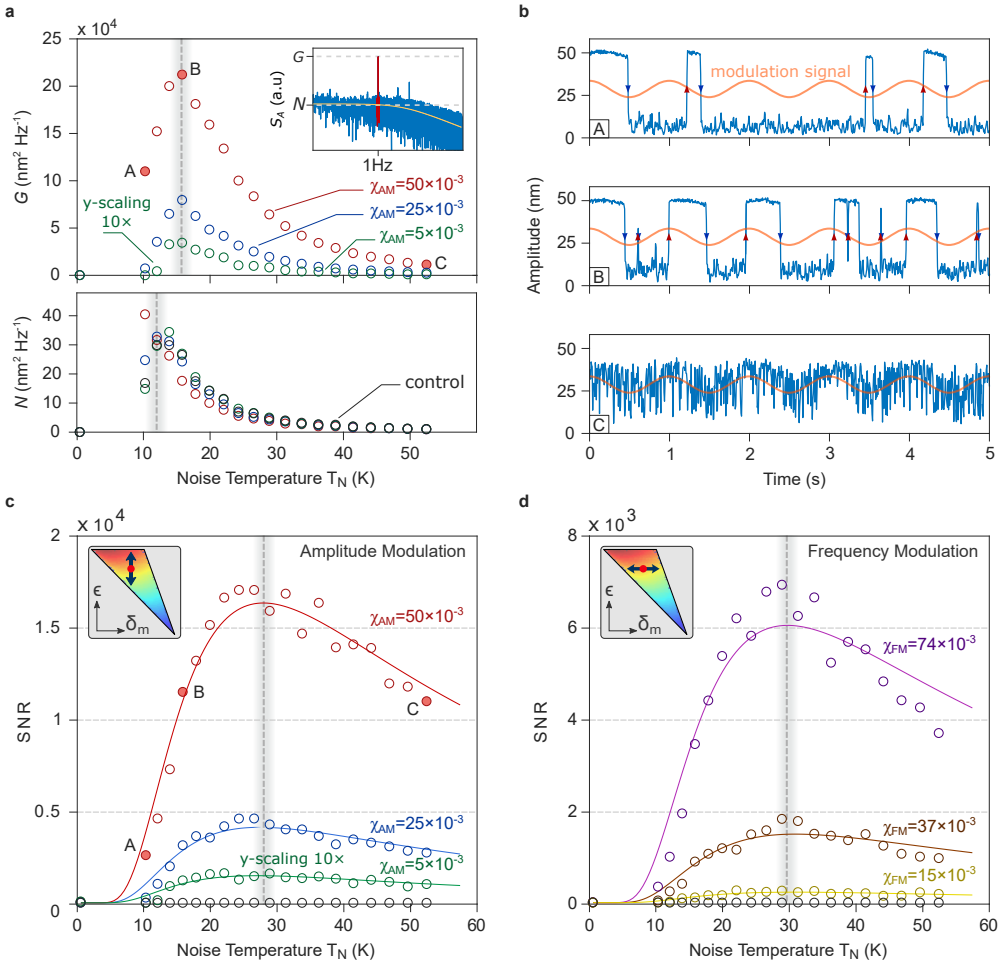

Figure 6.10: **Stochastic resonance experiment**. (a) Spectral amplification G and noise floor N as a function of the noise temperature for three different modulations. (b) Three examples of amplitude time traces for different noise temperatures (corresponding to points A,B and C in (a), together with the modulation signal (orange line, not to scale in y axis). For low noise (A) there is little correlation between switching dynamics and modulating signal. However, for higher noise (B) the system reaches synchronization and a maximum in G is found. If further increased (C), the noise leads to a degradation of the coherence in the switching dynamics. (c) The signal to noise ratio (SNR) of the detected modulating signal clearly presents a maximum (resonance) at $T_N \sim 28$ K. Note that the peak position depends on both G and N and is therefore not expected to coincide with the peak in (a). (d) The SNR curve for the SR experiment performed with frequency modulation of the driving signal. The same observations reported for (c) apply here. In both cases, black circles represent control data with $\chi_{AM/FM} = 0$ to show that no amplification is encountered without modulation.

6.5.2 Frequency Modulation

A second SR experiment was carried out for frequency modulation of the driving signal:

$$\delta_m(t) = \delta_m^* \left[1 + \chi_{\mathrm{FM}} \cos(\tilde{\omega} t)\right] \quad , \quad \epsilon = \epsilon^*. \tag{6.19}$$

which according to our study (see Fig. 6.5c), induces a potential modulation consistent with the SR requirements. The corresponding results are shown in Fig. 6.10d. We emphasize the fact that previous experiments [3, 9] have only explored the case of an amplitude modulation, and that this is the first experimental demonstration of SR with frequency modulated signals. Again the fitted modulation strengths give ratios $(1.9 : 2.6 : 4.9)$, in good agreement with the expected ones $(2 : 2.5 : 5)$. Interestingly, the resonance appears at a noise temperature equivalent to the one observed in the amplitude modulation case. This is consistent with the fixed value of $\tilde{\omega}$ along the two experiments that requires an equal Γ_K in order to fulfill the time-scale matching of the resonant condition.

6.5.3 Comparison with direct amplification

It is interesting now to quantitatively compare the amplification obtained in the SR scheme with another nonlinear amplification scheme that we refer as direct amplification. This consists in observing the modulation of the particle amplitude, introduced by the external perturbation, when the system is driven at the resonant condition: $\delta_{\mathrm{m}} = 0$. Note that for zero detuning the particle is driven outside of the bistable regime, but still inside the instability tongue (see inset in Fig. 6.11). In this configuration the effective potential is monostable and the AM and FM modulations applied result in a modulation of the oscillation amplitude for which a spectral analysis still shows a peak at $\tilde{\omega}$. After performing the same type of analysis carried out for the SR phenomenon, we obtain the SNR (as a function of noise temperature T_N) shown in Fig. 6.11. We fit the experimental data with exponential decays that properly follow the experimental data for $T_N < 30$ K. Moreover, in order to ease a direct comparison of the two amplification schemes, we report as well the the fits of Fig. 6.10c,d as dashed lines. We observe that, independently of the noise level, direct amplification always features a higher SNR than the corresponding SR, with the two methods giving similar outcomes at high T_N. We can interpret this this result as an experimental verification of the central dogma of signal detection theory [107], namely that stochastic resonance can decrease the SNR degradation of a noisy signal but it does not provide a mechanism by which the

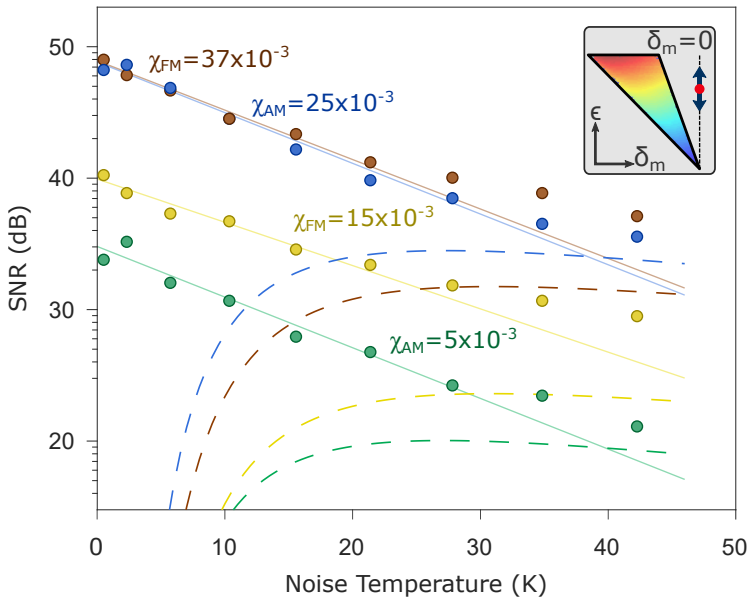

Figure 6.11: **Direct amplification experiment.** SNR of a 1 Hz weak modulation signal detected by the system prepared at resonance ($\delta_m = 0$) outside of the bistable regime, but still inside the instability tongue (inset). Circles are experimental data points for different AM/FM runs. Solid lines are fitted exponential decays, while dashed lines correspond to the fitted functions (6.18) of Fig. 6.10c,d and allow a straight comparison of the results obtained with the SR experiment (color coding preserved). In particular, independently of the noise level, direct amplification always features a higher SNR than the corresponding SR case, with the two curves approaching for high noise, in agreement with the central dogma of signal detection theory.

undetectable becomes detectable [22, 82]. The couterinuitive nature of SR, in fact, mainly relies on suboptimal parameter ranges [66], here exemplified by the fact that the same modulation becomes remarkably detectable when the detuning is set to zero, without the need of adding any noise. Nonetheless, the fact of SR being observed in a wide variety of settings poses the question of why this phenomenon is omnipresent and favored by nature. We surmise that suboptimal balanced configurations are generally preferable when dealing with very complex systems, for which optimal conditions would be difficult to achieve. Thus, exploiting ambient noise and stochastic resonance appears to be a successful strategy to ensure a robust amplification method that, at least above certain thresholds, is less sensitive to noise changes than other detection schemes (as exemplified by Fig. 6.11).

7 Conclusions and future perspective

In the first part of this concluding chapter we provide a general outlook of of the main achievement of this doctoral work. Next, future perspectives of the present work will be exposed, including possible technical improvements of the experimental apparatus, and proposals for future experiments.

7.1 Outlook

7.1.1 Technical improvements

At the beginning of this doctoral work considerable efforts have been put in the stabilization of the system. Leveraging on previous experiments [36, 38], further stabilization of the mechanical frequency has been achieved. An efficient optimization protocol of the feedback electronics was described in § 3.3, and allowed for a reduction of the optical noise. This, together with power optimization of the detection scheme (§ 3.2 and Fig. 3.4), and careful screening of air turbulence (affecting pointing stability of both the trapping and detection beam), provided an overall mechanical stability of $\sigma_{\Omega_0}/\Omega_0 \approx 10^{-4}$ over long term integration (experiment durations of $\sim 10^2$ s), and a maximum stability of $\sigma_{\Omega_0}/\Omega_0 = 2 \times 10^{-5}$ over short time scales ($\tau \lesssim 1$ s), at $P = 1.5 \times 10^{-7}$ mBar. As it was shown while discussing the stochastic bistable dynamics experiment (§ 6), the achieved stability has enabled for instance direct measurement of the nonlinear parameters of the

experiment ξ and η with just few percent uncertainty and was paramount for the quality of the results there reported.

The improvements of the vacuum system, compared to its initial stage, have been twofold: on the one hand, the setup was upgraded with a nitrogen pressure line for clean venting. Compared with air venting, this reduces contamination of the chamber and speeds up the pumping at subsequent evacuations. On the other hand, a baking system based on heating bands was implemented in order to heat the system up to temperatures of $\sim$ 140 °C, therefore achieving further cleaning of the chamber and consequently a better vacuum.

Finally, a direct force actuation scheme (see § 3.5) has been implemented in the set-up, complementary to the parametric actuation performed by laser modulation. The particles, previously considered to be neutral, were actually found to be initially charged in [85], bearing a net charge q of few elementary charges. This enabled the possibility to couple the particle to external electric fields E via Coulomb interaction $F = q \cdot E$. The generated electric field was estimated, up to just 1.1% error, via finite elements simulations which relied on a precise characterization of the electrodes geometry (see § 4.3.4 and Fig. 4.5). Additionally, a corona discharge scheme for controlling the charge of the particle was implemented by replicating the work of Frimmer et al. [29]. In our case, however, we showed that inverting the polarity of the high voltage generating the plasma, allowed to preferentially bias the final charge towards either positive or negative polarities. The implemented electrical driving was paramount in all the measurement related to § 4 and § 5, and will have an essential role in future experiments.

7.1.2 Experimental results

The present dissertation reports on the three main experiments conducted along the doctoral work. These are thoroughly discussed respectively in § 4, § 5 and § 6. In the following we summarize the results obtained in each case.

Precise measurement of the particle's mass
In § 4, a novel protocol for precisely measuring the mass of a levitated nanoparticle has been presented. This project was motivated by the necessity of more reliable displacement calibration procedures [44], which have a severe impact on the accuracy of the system in sensing applications. To put the experiment into context, in § 4.2 we estimated the uncertainties associated

with the already existing mass measurement protocols. The outcomes draw attention on a general problem of levitated nanoparticles, whose mass is usually given with errors as high as $\sim 30\%$. Making use of the analytical solution to the thermally and harmonically driven damped resonator (see § 2.2), in § 4.3.2 we showed that the response to a known resonant electric field carries information on the mass of the resonator. The main result of this section is contained in Eq. (4.10) which is used in § 4.3.3 to demonstrate the protocol in a real measurement. This equation for the particle's mass directly exhibits the possible sources of error in its calculation. Consequently, § 4.3.4 is dedicated to a precise estimation of such errors. We conclude that the one relative to the electric field $\sigma_{E_0}/E_0 = 1.1\%$ represents the dominant uncertainty, while for other quantities like bath temperature T, damping Γ and power spectral densities S_v and S_v^{th}, they can be maintained below 1%. Finally, error propagation has been applied to calculate both the statistical and the systematic errors associated to our measurement protocol. We obtained a total error of 2.4% which makes our scheme more than an order of magnitude more precise than other methods. Direct applications of the proposed protocol are given in the next experiment, where subsequent mass measurements during pressure pumps-down clearly demonstrate mass-losses from a levitated silica particle.

Pressure-dependent mass and charge

This chapter was dedicated to the understanding of an unexpected pressure-dependence of some particle properties. In § 5.2.1 we provided a comprehensive description of the observed phenomena . The section exemplifies the capabilities of our system to monitor in real time quantities such as the charge of the particle and its scattering intensity. Capitalizing on the mass measurement method, in § 5.2.2 we correlated such observations with intrinsic mass-losses from the silica particle. Further experimental investigations also demonstrated its reverse process, i.e. mass uptakes from an humid environment. In § 5.2.4 and § 5.3 we dealt with the measurement of the particle's charge. First, statistics on the charge variations when going to vacuum has been provided, suggesting the presence different ionic species adsorbed on the surface for different particle sizes, , probably due to the different synthesis routes. In § 5.3, we proposed and demonstrated a protocol to measure arbitrarily large numbers of elementary charges: a non-trivial task for highly charged particles ($|n_q| \gtrsim 50$). Finally the chapter is concluded with an extensive discussion on possible explanations for the observed phenomena. According to the so-called Zhuravlev model, the silica surface is covered by water both physically and chemically adsorbed. Our data seems to confirm that the former is

desorbed from the surface after the particle is brought into moderate vacuum. Chemically adsorbed water (i.e. OH silanol groups bound to silica atoms), instead, are most likely not completely removed, although their concentration is way lower than the physically adsorbed water, and can be further decreased in high vacuum thanks to the considerable bulk temperatures that the particle reaches [46]. For the current state of our experiments, the presence of chemisorbed water does not represent an issue. However, for future developments in the field, nanoparticles could be thermally treated above $T = 1200\ ^{\circ}\mathrm{C}$ either before the loading or while already in the trap with a focused a CO_2 laser [46].

A model system for stochastic bistable dynamics

The content of this chapter describes the most sophisticated (and somehow troublesome) experiment carried out along this doctoral work. Former studies [36, 38] with particles trapped in optical tweezers showed their intrinsic feature of behaving as a Duffing resonator, and as such, displaying interesting nonlinear phenomena like bistability and hysteretic behaviors. In § 6.3 we started with an extensive study of the particle's response to parametric driving. This section led us to the definition of iso-amplitude lines inside the first instability tongue. To our knowledge this feature was here observed for the first time, and played a crucial role in the development of a bistable model for particle dynamics in the nonlinear regime. To access the bistable dynamics, additional noise had to be injected in the system. In § 6.3.2 we characterized the particle's response to external noise, obtaining a temperature calibration that was paramount for quantitative analysis of the stochastic switching phenomenon. This first part of the chapter concludes with an in-depth characterization of the bistable double-well potential shape as a function of driving parameters (δ_m, ϵ).

The control obtained on the system, enabled us to implement an experiment to test the sensing capabilities of stochastic resonance (SR): a nonlinear stochastic process that was proposed as a force detection scheme in noisy environments [2,4,9,108]. The frequency stability achieved - in particular close to the bifurcation points - led us (to our knowledge) to the first qualitative and quantitative agreement between the SR of a nanomechanical resonator and the corresponding analytical models. Moreover, thanks to a deep understanding of the processes that degrade the SR (such as hysteresis quenching [108] and potential asymmetries), and implementing compensation techniques to avoid them, we believe that the capabilities of SR as a detection scheme have been pushed to their limits. Ultimately, we outperformed existing measure-

ments [108] and reported amplifications up to 10^4 of weak signals corresponding to parametric forces of tens to hundreds atto-Newtons. Nevertheless, in § 6.5.3 we provided a sensitivity comparison of SR with a complementary direct amplification scheme. Our results show that independently of the noise level, direct amplification always features a higher SNR than the corresponding SR, and the two methods give similar outcomes only at high noise levels. In agreeement with theoretical predictions [22, 82], these findings experimentally demonstrate that stochastic resonance can decrease the SNR degradation of a noisy signal but it does not provide a mechanism by which the undetectable becomes detectable. Although it is not generally convenient to perform force detection with stochastic resonance, we foresee in optically levitated nanoparticles a suitable platform for mimicking very complex stochastic nonlinear dynamics, the SR experiments being a prominent example. This could allow to shine a light on natural phenomena such as bio-molecule folding [5, 41], hearing [23, 64], neural signalling [67], and to tackle fundamental questions of stochastic thermodynamics [11].

7.2 Future perspectives

There are always characteristic transient times from the very first spark of a scientific idea to its practical implementation and ultimately to useful applications that have an impact either in everyday life or in fundamental research. This whole process takes considerable time and undergoes very diverse phases. It is worth mentioning that Arthur Ashink, the father of levitodynamics, has been recently awarded the 2018 Nobel prize in physics precisely for triggering that spark. His pioneering experiments in levitation of dielectric particles, paved the way for most of the works discussed and cited in this thesis. Likewise, T. Li, J. Gieseler (from whom I inherited the setup) and the scientists that started developing levitation in vacuum ten years ago share the credit for impelling a positive slope in the trend of growth of this field. Current levitodynamics experiment are still experiencing that trend, and an increasing interest from the scientific community can be inferred. Here we present what we envision as possible experiments, achievements or applications that could lead the field to take additional forward steps along that positive trending slope.

Quantum optomechanics with levitated nanoparticles Compared to atoms and molecules, nanoparticles used in levitation experiments are dense object with significant masses that belong to the often mentioned mesoworld. Bring-

ing these mesoscopic objects into the quantum regime is certainly one of the driving motors of levitodynamics (if not the *Holy Grail* of this field [92]). Current implementations and future proposals of groundbreaking experiments are paving the way toward the exploration of the quantum to classical transition. In this context we envision the possibility of performing matter-wave interferometry in order to test collapse model and study the decoherence effects responsible for such transition [91]. Although the state-of-the-art toward ground state of a levitated nanoparticle has been set with parametric feedback in a tweezer configuration [50], resolved sideband cavity cooling seems nowadays to have great potential to achieve the objective, and is soon expected to overtake the former systems in the race toward the quantum regime. Given the situation, parametric feedback may not be the most competitive approach. Still, better cooling schemes (for instance relaying on phase-locked-loop or exploiting Kalman filtering for optimal position estimation) could be desirable to reach the photon recoil limit, where higher Q-factors, better stability and in general higher sensitivity, would boost the performances of our force nano-sesensor.

Frequency stability of levitated nanoresonators The frequency stability of levitated oscillators is often a disregarded topic. Though, there are studied that show how in most cases (and actually always, when dealing with clamped SiN systems) resonators do not sit on the thermomechanical limit of frequency stability, and excessive unexplained phase noise is observed [95]. Similar investigations have not been yet carried out with levitated resonators, and there is not a clear opinion whether this class of resonators could be more suited to overcome this excess of noise, therefore reaching the thermomechanical limit. Amongst the possible causes of such noise excesses Sansa et al. suggest electrostatically induced changes in stiffness, molecules adsorbtion/desorption onto/from the resonator, or diffusing along its surface, dielectric and charge fluctuations and thermalization of higher order modes through nonlinear mode coupling [95]. Interestingly, these are all effects that could be minimized (an perhaps even completely suppressed) by the intrinsic nature of levitated systems of being decoupled from the environment and not oscillating in flexural modes.

Force sensing In its current current state, our system presents a resonant force sensitivity, as predicted by Eq (2.79), equal to $\sqrt{S_{F_{\text{min}}}} \sim 18$ zN$/\sqrt{Hz}$. This equation tells us which parameters could be optimized to boost our sensitivity. Firstly, smaller particles could be used, with diameters as small as

$d_p = 50$ nm. The mass would then result ~ 25 times smaller ($m = 0.15$ fg) than the ones currently used. Modern technologies allow for easy implementations of cryogenic refrigeration in optical experiments. The bath temperature could then be reduced down to $T \simeq 4$ K. Mechanical Q-factors as high as 10^{11} were predicted in ultra-high vacuum conditions [35]. However, it was later shown [50] that for the typical size of particle used, at pressures of 10^{-8} mBar the system already reaches the photon recoil limit. Therefore, lower pressures would not help in further reducing Γ. We expect this to be limited in the mrad/s range. Plugging everything into Eq 2.79, we would obtain sub-zepto-Newton sensitivity of $\sqrt{S_{F_{\mathrm{min}}}} \sim 0.2$ zN$/\sqrt{Hz}$. Finally, sensing experiment can in principle exploit long integration times (small bandwidths b) to reach smaller minimum forces detectable. This is eventually limited by the mechanical stability of the system, which should be free from frequency jittering of the mechanical resonance (notice, this is an additional motivation for stabilization of the resonator down to the thermomechanical limit, as expressed in the previous paragraph). The current stability of the system has been characterized and ensures integration times on the 1 s timescale. However, active stabilization has been demonstrated [32] and implemented in systems very similar to ours [43] to reach stability up to $\sim 10^3$ s. Performing a force measurement with these envisioned realistic parameters would take levitodynamics systems into the yoctoNewton regime ($1yN = 10^{-24}N$), with sensitivities comparable to those of trapped ions [12], while using significantly simpler experimental platforms.

An interesting force sensing scheme, recently demonstrated by Hebestreit et al., is based on free falling particles. The main difference of this scheme, compared to conventinal resonant force detection, is its sensitivity to static forces. Current implementations led to the detection of forces at the atto-Newton scale, and even higher sensitivities are within reach after technical improvements of the system. The ability of detecting DC forces opens up the possibility of exploring the regime of short-range forces such as Casimir and non-Newtonian gravity-like forces [33].

Finally, more exotic sensing schemes could be explored already with the current system. Following some proposals [80] and proof-of-concept experiments with macroscopic resonators [24], for instance, a nonlinear parametric symmetry breaking force transducer could be realized. This strategy would be very interesting in our system because it relies on concept already thoroughly investigated in § 6 such as parametric actuation in the first instability tongue and bistability.

Material science In § 5 it was mentioned how our assumptions on the particle's morphology had to be adapted along with our understanding of the particle's properties in vacuum. From a very simplified model of a solid and unchanging glass sphere, we are now dealing with very complex models (the Zhuravlev, for instance) on the surface chemistry of silica, and its interaction with adsorbed water. The results presented in § 5 provide a straightforward example of the kind of information that a levitation experiment can provide on the morphology of the silica particle. Needless to say that silica is one of the most widespread materials for technological applications: from optical fibers, to electrical isolators in microelectronics, up to more recent utilization in the creation of artificial opals with interesting optical properties for photonic crystals [31]. As such, we envision the interesting possibility to investigate material properties at the nanoscale, i.e. on a single isolated particle, as opposed to chemistry experiments where samples are usually an ensemple of individual elements and abrupt physical events get averaged out in collective behaviors. We stress that to overcome the light absorption problem (that severely limits the suitable materials for optical levitation), one could rely on different levitation schemes such as like Paul traps.

Appendices

A

Calibration of particle detection

In the experiments presented throughout this thesis, and more generally in any levitation experiment, the calibration of the particle's detection represents a central part of the experimental protocols. This consists in converting the measured signal $v_i(t)$ from the detectors (measured in *volts*) into a physical particle displacement $q_i(t)$ measured in *meters*, where $i = x, y, z$ indicates the three different oscillation modes. Conventional methods assume a linear proportionality between the particle's position and the detector signal, such that the calibration factor is $c_{\text{cal}}^{(i)} = v_i(t)/q_i(t)$. A second assumption made in the typical calibration procedures is to consider the motion of the particle as that o a perfect harmonic oscillator, therefore neglecting possible nonlinear contributions in its dynamics. This allows to relate the measured signal (and more precisely its variance) to the known bath temperature through the *equipartition principle*. Note that in order to apply this calibration method, the mass of the particle needs to be known. This again a motivation for § 4.3 with the objective of lowering the inaccuracy on the particle's mass.

Linear calibration of particle detection

The state-of-the-art method used in the levitation community to calibrate the detectors signals (also extensively used in throughout the experiment hereby described), is to assume the particle's dynamics at high pressure $P \sim 10$ mBar

to be that of a perfect harmonic oscillator in thermal equilibrium with the environment. With this assumptions, we can relate the experimentally measured power spectral density S_v, measured in units of V^2/Hz to the expected resonator power spectral density, measured in m^2/Hz, given as a function of the damping Γ, the bath temperature T, the oscillator's mass m and the oscillation eigenfrequency Ω_0.

In practice, we derive S_v as follows:

(i) record a number n_{PSD} of discretized time signals $v(t), t \in [0, T]$ at a sampling rate $f_s = 625$ kHz (note that this sampling is limited by the speed of the FPGA's digital-to-analog-conver). n_{PSD} and T can vary depending on the specific needs, however typical values are $n_{PSD} = 100$, $T = 80$ ms.

(ii) apply to $v(t)$ a *Hanning* window function $w = \{w_j, j = 1 \dots N\}$ defined as:

$$w_j = \frac{1}{2}\left[1 - \cos\left(\frac{2\pi j}{N}\right)\right] , \tag{A.1}$$

being $N = T \cdot f_s$ the number of elements in the vector $v(t)$, and defining the quantity $S_2 = \sum_{j=1}^{N} w_j^2$.

(iii) compute the *Fast Fourier Transform* $\mathcal{F}_{DFT}[w \cdot v(t)]$

(iv) Finally obtain the experimental power spectral density as the average over the n_{PSD} PSDs:

$$S_v(f) = \frac{\left|\mathcal{F}_{DFT}[w \cdot v(t)]\right|^2}{f_s S_2} \cdot \begin{cases} 2, & f > 0 \\ 1, & f = 0 \\ 0, & f < 0 \end{cases} \tag{A.2}$$

Note that the expression given in (A.2) is defined in the the natural frequency f domain. To convert it into the angular frequency domain we substitute $\omega = 2\pi f$, and energy conservation is ensured by the 2π factor included in the Parseval's theorem identity (2.58).

We then fit the experimental PSD S_v with a typical lorentzian function of the form

$$S(\omega) = a_4 + \frac{a_1}{(\omega^2 - a_2^2)^2 + a_3^2\omega^2} , \tag{A.3}$$

$a_1, \cdots, a_4$ being free fitting parameters, and compare with the analytical expected form, preiviously derived in (2.65),

$$S_x(\omega) = \frac{2k_B T\Gamma}{m\left[\left(\omega^2 - \Omega_0^2\right)^2 + \Gamma^2\omega^2\right]} . \tag{A.4}$$

Note that the additive factor a_4 allows to take into account the measurement noise in the system: a contribution of optical and electrical noise that, assumed to be white, introduces a constant offset in the power spectral density. Recalling that $S_x(\Omega) = S_v(\Omega)/C_{cal}^2$, we obtain the following correspondence:

$$a_1 = C_{cal}^2 \frac{2k_B T\Gamma}{m} \tag{A.5}$$

$$a_2 = \Omega_0 \tag{A.6}$$

$$a_3 = \Gamma \tag{A.7}$$

Finally, the the calibration factor is calculated as:

$$C_{cal} = \sqrt{\frac{a_1}{a_2}\frac{m}{k_B T}}\,. \tag{A.8}$$

Calibration with equipartition of potential energy

An equivalent calibration method to that above described, is to make use of the equipartition theorem of the potential energy, which reads:

$$\left\langle E_{pot}\right\rangle = \frac{1}{2}m\Omega_0^2\left\langle x^2\right\rangle = \frac{1}{2}m\Omega_0^2\frac{\left\langle v^2\right\rangle}{C_{cal}^2} = \frac{1}{2}k_B T \tag{A.9}$$

Using the variance $\left\langle v^2\right\rangle$ of the detected signal time trace $v(t)$, the eigenfrequency Ω_0 from a fit to the power spectral density $S_v(\Omega)$ and $T \simeq 300K$, one obtains:

$$C_{cal} = \sqrt{\frac{m\Omega_0^2\left\langle v^2\right\rangle}{k_B T}} \tag{A.10}$$

Calibration with equipartition of kinetic energy

One of the main problems of the two equivalent calibration methods above described, is the assumption of harmonicity of the potential. In fact, eq. (A.9) holds only for a strictly harmonic oscillator, while nonlinear correction terms have to be included in the case of a anharmonic resonator. We know that in our system such nonlinearities affect the dynamics of the particle [36]. This is mostly true at higher vacuum levels, but may introduce non-negligible errors even at higher pressures of $P \sim 1$ mBar, where we perform the displacement calibration.

On the other hand, the equipartition of the kinetic energy holds true independently of the harmonicity of the dynamics. As a result we could use the

following equation to extract the calibration factor:

$$\langle E_{kin} \rangle = \frac{1}{2} m \langle \dot{x}^2 \rangle = \frac{1}{2} m \frac{\langle \dot{v}^2 \rangle}{C_{cal}^2} = \frac{1}{2} k_B T \tag{A.11}$$

Here, $\dot{x} = \dot{v}/C_{cal}$ is the velocity of the particle. Experimentally this could be calculated with a fast sampling of the position, and a time time derivative of the recorded signal. However, this method is computationally demanding, and can be replaced by a mathematical trick. It can be demonstrated that the power spectral density of the variable x and of its derivative $\dot{x}$ are linked by the following relation:

$$S_{\dot{x}}(\Omega) = \Omega^2 S_x(\Omega) \tag{A.12}$$

Therefore, the variance $\langle \dot{v}^2 \rangle$ can be calculated integrating $S_{\dot{v}}(\Omega) = \Omega^2 S_v(\Omega)$ and inverting eq. (A.11) to obtain:

$$C_{cal} = \sqrt{\frac{m \langle \dot{v}^2 \rangle}{k_B T}} \tag{A.13}$$

B

Electrically driven peak estimation

A crucial step in several protocols presented throughout this work is the experimental observation of an ultra-narrow peak in the power spectral density of the harmonically driven resonator (see for instance Fig. 4.3). In this section we treat a delicate analysis issue related to the time span of the measured signal $v(t)$, and the associated frequency resolution in $S_v(\omega)$.

The finite measurement time τ of a continuous signal $v(t)$ leads to the *sinc* function in (2.74), appearing as the fourier transform of the square function:

$$H(t;\tau) = \begin{cases} 1\ , & 0 < t < \tau \\ 0\ , & \text{elsewhere.} \end{cases}$$

The width of such $\text{sinc}^2[(\omega - \omega_{\text{dr}})\tau]$ function is inversely proportional to the length of the signal τ in the time domain [1], and can result in a very narrow peak in the PSD. For typical sampling parameters used in our experiments, the time signal recorded has a time span of $\tau = 80$ ms, corresponding to a total number of samples $N = \tau \cdot f_s = 50$ kS, being f_s the sampling rate of our acquisition.

When detecting very narrow-band signals in the computed PSD, one has to be careful with the resolution of the frequency domain. In fact, if no special

[1] A first approximation for the width can be obtained solving $\text{sinc}(\omega_- \tau) = 0$, which would give a width $\Delta\omega = 2\pi/\tau$. However, a more rigorous approach is to calculate the $FWHM[\text{sinc}(\omega_- \tau)]$ solving $\text{sinc}(\omega_- \tau) = 0$. This more complicate case give the approximated solution $\Delta\omega \simeq 3.79/\tau$.

measures are taken, one could in principle detect the signal as a single (or very few) bin(s) peak without resolving the whole *sinc* function. This partial resolution introduces a spurious detection of the peak's height, which in turns affects the corresponding estimation of $S_v(\omega_{\mathrm{dr}})$.

To tackle this issues, let us remind that the maximum detectable frequency, according to the *Nyquist* limit is $f_{max} = f_s/2$, and that standard Fast-Fourier-Transform (FFT) algorithms give a frequency resolution $\Delta f = \frac{f_s/2}{N/2+1} \sim \frac{f_s}{N} = \frac{1}{\tau}$ [2]. As a result, both the *sinc*-shaped peak and the frequency bin $\Delta\omega$ have a width that scales inversely proportional to τ. In other words increasing the measurement time τ, improves our frequency resolution Δf, but does not improve our peak resolution.

The solution is to use the so-called *padding* of the input signal. This practice consists in extending the array in the time domain adding zeroes at its sides, therefore creating a longer signal of length T (made of $2 \times n_{\mathrm{FFT}}$ points) that still contains the harmonic function exclusively inside of $H(t;\tau)$. By doing so, we can maintain a fixed width of the *sinc* function, and simultaneously increase at will our frequency resolution. This effect is visually described in figure B.1a. Figure B.1b, shows when the peak's height starts to be properly sampled for the specific case of $\tau = 80$ ms (typically used in our experiments), while in Fig. B.1c, this is generalized for different integration times τ.

[2] This is because they preserve the length N of the time signal also in the frequency domain

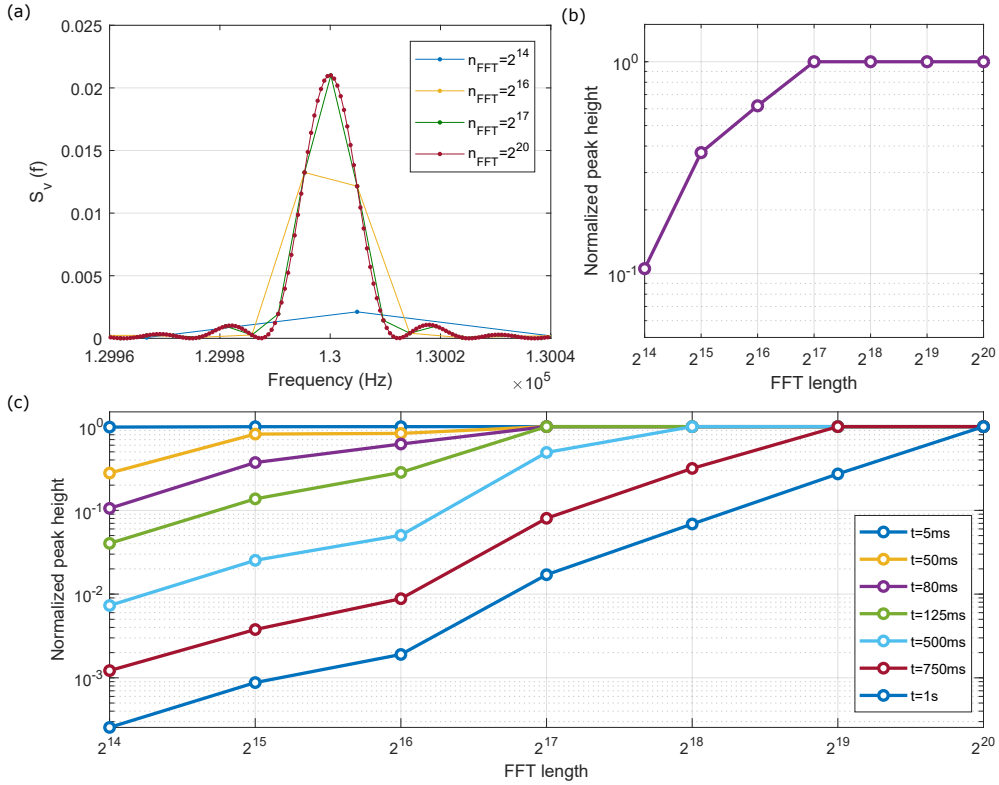

Figure B.1: **Exact detection of driven peak height**

Bibliography

[1] Coherent ®. *Mephisto Lasers Datasheet*, 2018. , cit. on p. ↑37

[2] S. Aldana, C. Bruder, and A. Nunnenkamp. Detection of weak forces based on noise-activated switching in bistable optomechanical systems. *Physical Review A*, **90**(6):1–8, 2014. , cit. on p. ↑88, ↑112

[3] J. S. Aldridge and A. N. Cleland. Noise-enabled precision measurements of a duffing nanomechanical resonator. *Physical Review Letters*, **94**(15):5–8, 2005. , cit. on p. ↑100, ↑104, ↑106

[4] R. Almog, S. Zaitsev, O. Shtempluck, and E. Buks. Signal amplification in a nanomechanical Duffing resonator via stochastic resonance. *Applied Physics Letters*, **90**(1):1–4, 2007. , cit. on p. ↑88, ↑112

[5] D. Angeli, J. E. Ferrell, and E. D. Sontag. Detection of multistability, bifurcations, and hysteresis in a large class of biological positive-feedback systems. *Proceedings of the National Academy of Sciences*, **101**(7):1822–1827, 2004. , cit. on p. ↑88, ↑113

[6] P. Asenbaum, S. Kuhn, S. Nimmrichter, U. Sezer, and M. Arndt. Cavity cooling of free silicon nanoparticles in high vacuum. *Nature Communications*, **4**:2743, 2013. , cit. on p. ↑4

[7] A. Ashkin. Acceleration and Trapping of Particles by Radiation Pressure. *Physical Review Letters*, **24**(4):156–159, 1970. , cit. on p. ↑3

[8] A. Ashkin and J. M. Dziedzic. Optical levitation in high vacuum. *Applied Physics Letters*, **28**(6):333–335, 1976. , cit. on p. ↑3

[9] R. L. Badzey and P. Mohanty. Coherent signal amplification in bistable nanomechanical oscillators by stochastic resonance. *Nature*, **437**:995–998, 10 2005. , cit. on p. ↑88, ↑106, ↑112

[10] S. A. Beresnev, V. G. Chernyak, and G. A. Fomyagin. Motion of a spherical particle in a rarefied gas. part 2. drag and thermal polarization. *Journal of Fluid Mechanics*, **219**:405–421, 1990. , cit. on p. ↑54

[11] A. Bérut, A. Arakelyan, A. Petrosyan, S. Ciliberto, R. Dillenschneider, and E. Lutz. Experimental verification of Landauer's principle linking information and thermodynamics. *Nature*, **483**:187–189, 2012. , cit. on p. ↑113

[12] M. J. Biercuk, U. Hermann, J. W. Britton, A. P. VanDevender, and J. J. Bollinger. Ultrasensitive detection of force and displacement using trapped ions. *Nature Nanotechnology*, **5**:646–650, 2010. , cit. on p. ↑115

[13] G. Binnig, C. F. Quate, and Ch. Gerber. Atomic force microscope. *Physical Review Letters*, **56**:930–933, Mar 1986. , cit. on p. ↑1

[14] G. Binnig and H. Rohrer. Scanning tunneling microscopy. *Surface science*, **126**(1-3):236–244, 1983. ↑1

[15] M. Brownnutt, M. Kumph, P. Rabl, and R. Blatt. Ion-trap measurements of electric-field noise near surfaces. *Reviews of modern Physics*, **87**(4):1419, 2015. , cit. on p. ↑4

[16] D. E. Chang, C. A. Regal, S. B. Papp, D. J. Wilson, J. Ye, O. Painter, H. J. Kimble, and P. Zoller. Cavity opto-mechanics using an optically levitated nanosphere. *Proceedings of the National Academy of Sciences*, **107**(3):1005–1010, 2010. , cit. on p. ↑82

[17] J. Chaste, A. Eichler, J. Moser, G. Ceballos, R. Rurali, and A. Bachtold. A nanomechanical mass sensor with yoctogram resolution. *Nature Nanotechnology*, **7**:301–304, Apr 2012. , cit. on p. ↑2, ↑51

[18] Gerard P. Conangla, Andreas W. Schell, Raúl A. Rica, and Romain Quidant. Motion control and optical interrogation of a levitating single nitrogen vacancy in vacuum. *Nano Letters*, **18**(6):3956–3961, Jun 2018. , cit. on p. ↑4

[19] S. L. De Bonis, C. Urgell, W. Yang, C. Samanta, A. Noury, J. Vergara-Cruz, Q. Dong, Y. Jin, and A. Bachtold. Ultrasensitive displacement noise measurement of carbon nanotube mechanical resonators. *Nano letters*, **18**(8):5324–5328, 2018. , cit. on p. ↑2

[20] T. Delord, L. Nicolas, M. Bodini, and G. HÃl'tet. Diamonds levitating in a paul trap under vacuum: Measurements of laser-induced heating via nv center thermometry. *Applied Physics Letters*, **11**(1):013101, 2017. , cit. on p. ↑4

[21] J. P Dowling and G. J. Milburn. Quantum technology: the second quantum revolution. *Philosophical Transactions of the Royal Society of London A: Mathematical, Physical and Engineering Sciences*, **361**(1809):1655–1674, 2003. , cit. on p. ↑2

[22] M. I. Dykman and P. V. E. McClintock. What can stochastic resonance do? *Nature*, **391**(6665):344, 1998. , cit. on p. ↑107, ↑113

[23] V. M. Eguíluz, M. Ospeck, Y. Choe, A. J. Hudspeth, and M. O. Magnasco. Essential nonlinearities in hearing. *Physical Review Letters*, **84**(22):5232–5235, 2000. , cit. on p. ↑113

[24] A. Eichler, T. L. Heugel, A. Leuch, C. L. Degen, R. Chitra, and O. Zilberberg. A parametric symmetry breaking transducer. *Applied Physics Letters*, **112**(23):233105, 2018. , cit. on p. ↑115

[25] A. Eichler, J. Moser, J. Chaste, M. Zdrojek, I. Wilson-Rae, and A. Bachtold. Nonlinear damping in mechanical resonators made from carbon nanotubes and graphene. *Nature Nanotechnology*, **6**(6):339, 2011. , cit. on p. ↑25

[26] A. Einstein. Investigation on the theory of the brownian movement. *Annalen der Physik*, 1905. , cit. on p. ↑3

[27] R. Feynmann. There's Plenty of Room at the Bottom. *Caltech Engineering and Science*, **23**(5):22–36, 1960. , cit. on p. ↑1

[28] A. Fridman and L. A. Kennedy. *Plasma physics and engineering*. CRC press, 2004. , cit. on p. ↑47

[29] M. Frimmer, K. Luszcz, S. Ferreiro, V. Jain, E. Hebestreit, and L. Novotny. Controlling the net charge on a nanoparticle optically levitated in vacuum. *Physical Review A*, **95**:061801, Jun 2017. , cit. on p. ↑5, ↑47, ↑56, ↑110

[30] L. Gammaitoni, P. Hänggi, and P. Jung. Stochastic resonance. *Reviews of Modern Physics*, **70**(1):223–287, 1998. , cit. on p. ↑88, ↑103, ↑104

[31] F. García-Santamaría, H. Míguez, M. Ibisate, F. Meseguer, and C. López. Refractive index properties of calcined silica submicrometer spheres. *Langmuir*, **18**(5):1942–1944, 03 2002. , cit. on p. ↑53, ↑74, ↑81, ↑85, ↑116

[32] E. Gavartin, P. Verlot, and T. J. Kippenberg. Stabilization of a linear nanomechanical oscillator to its thermodynamic limit. *Nature Communications*, 2013. , cit. on p. ↑115

[33] A. A. Geraci, S. B. Papp, and J. Kitching. Short-range force detection using optically cooled levitated microspheres. *Physical Review Letters*, **105**(10):101101, aug 2010. , cit. on p. ↑115

[34] J. Gieseler. *Dynamics of optically levitated nanoparticles in high vacuum*. Ph.d. thesis, 2014. , cit. on p. ↑6, ↑35, ↑38, ↑54, ↑95

[35] J. Gieseler, B. Deutsch, R. Quidant, and L. Novotny. Subkelvin parametric feedback cooling of a laser-trapped nanoparticle. *Physical Review Letters*, **109**(10):1–5, 2012. , cit. on p. ↑3, ↑25, ↑39, ↑54, ↑115

[36] J. Gieseler, L. Novotny, and R. Quidant. Thermal nonlinearities in a nanomechanical oscillator. *Nature Physics*, **9**(12):806–810, 2013. , cit. on p. ↑5, ↑57, ↑64, ↑88, ↑109, ↑112, ↑121

[37] J. Gieseler, R. Quidant, C. Dellago, and L. Novotny. Dynamic relaxation of a levitated nanoparticle from a non-equilibrium steady state. *Nature Nanotechnology*, **9**(5):358–64, 2014. , cit. on p. ↑5, ↑95, ↑96

[38] J. Gieseler, M. Spasenović, L. Novotny, and R. Quidant. Nonlinear mode coupling and synchronization of a vacuum-trapped nanoparticle. *Physical Review Letters*, **112**(10):1–5, 2014. , cit. on p. ↑65, ↑95, ↑109, ↑112

[39] M. S. Hanay, S. Kelber, A. K. Naik, D. Chi, S. Hentz, E. C. Bullard, E. Colinet, L. Duraffourg, and M. L. Roukes. Single-protein nanomechanical mass spectrometry in real time. *Nature Nanotechnology*, **7**(9):602, 2012. , cit. on p. ↑2

[40] P. Hänggi, P. Talkner, and M. Borkovec. Reaction-rate theory: Fifty years after Kramers. *Reviews of Modern Physics*, **62**(2):251–341, 1990. , cit. on p. ↑5, ↑88

[41] K. Hayashi, S. de Lorenzo, M. Manosas, J. M. Huguet, and F. Ritort. Single-molecule stochastic resonance. *Physical Review X*, **2**:031012, Aug 2012. , cit. on p. ↑88, ↑113

[42] W. M. Haynes, D. R. Lide, and T. J. Bruno. *CRC Handbookof Chemistry and Physics*. 97th ed. CRC Press, 2016. , cit. on p. ↑54

[43] E. Hebestreit. *Thermal Properties of Levitated Nanoparticles*. Doctoral thesis, 2017. , cit. on p. ↑36, ↑55, ↑83, ↑115

[44] E. Hebestreit, M. Frimmer, R. Reimann, C. Dellago, F. Ricci, and L. Novotny. Calibration and temperature measurement of levitated optomechanical sensors. *Review of Scientific Instruments*, **89**(3):033111, 2018. , cit. on p. ↑63, ↑110

[45] E. Hebestreit, M. Frimmer, R. Reimann, and L. Novotny. Sensing static forces with free-falling nanoparticles. *Physical Review Letters*, **121**:063602, Aug 2018. , cit. on p. ↑4

[46] E. Hebestreit, R. Reimann, M. Frimmer, and L. Novotny. Measuring the internal temperature of a levitated nanoparticle in high vacuum. *Physical Review A*, **97**:043803, Apr 2018. , cit. on p. ↑66, ↑82, ↑112

[47] D. Hempston, J. Vovrosh, M. ToroÅą, G. Winstone, M. Rashid, and H. Ulbricht. Force sensing with an optically levitated charged nanoparticle. *Applied Physics Letters*, **111**(13):133111, 2017. , cit. on p. ↑4, ↑5

[48] J. F. Hsu, P. Ji, C. W. Lewandowski, and B. D'Urso. Cooling the motion of diamond nanocrystals in a magneto-gravitational trap in high vacuum. *Scientific Reports*, 2016. , cit. on p. ↑4

[49] V. Jain. *Levitated optomechanics at the photon recoil limit*. PhD thesis, 2017. , cit. on p. ↑13, ↑36

[50] V. Jain, J. Gieseler, C. Moritz, C. Dellago, R. Quidant, and L. Novotny. Direct measurement of photon recoil from a levitated nanoparticle. *Physical Review Letters*, **116**:243601, Jun 2016. , cit. on p. ↑3, ↑4, ↑114, ↑115

[51] P. H. Jones, O. M. MaragÃš, and G. Volpe. *Optical Tweezers: Principles and Applications*. Cambridge University Press, 2015. , cit. on p. ↑12

[52] R. Kaltenbaek, M. Aspelmeyer, P. F. Barker, A. Bassi, J.ames Bateman, K. Bongs, S.O Bose, C. Braxmaier, Č. Brukner, B. Christophe, M. Chwalla, P. Cohadon, A. M. Cruise, C. Curceanu, K. Dholakia, L. Diósi, K. Döringshoff, W. Ertmer, J.an Gieseler, N. Gürlebeck, G. Hechenblaikner, A. Heidmann, S. Herrmann, S. Hossenfelder, U. Johann, N. Kiesel, M. Kim, C. Lämmerzahl, A. Lambrecht, M. Mazilu, G. J. Milburn, H. Müller, L. Novotny, M. Paternostro, A. Peters, I. Pikovski, André PilanÂăZ., E. M. Rasel, S. Reynaud, C. J. Riedel, M. L. Rodrigues, A. Roura, W. P. Schleich, Jörg Schmiedmayer, T. Schuldt, K. C. Schwab, M. Tajmar, G. M. Tino, H. Ulbricht, R. Ursin, and V. Vedral. Macroscopic quantum resonators (maqro): 2015 update. *EPJ Quantum Technology*, **3**(1):5, Mar 2016. , cit. on p. ↑4

[53] R. B. Karabalin, R. Lifshitz, M. C. Cross, M. H. Matheny, S. C. Masmanidis, and M. L. Roukes. Signal amplification by sensitive control of bifurcation topology. *Physical Review Letters*, **106**(9):1–4, 2011. , cit. on p. ↑88

[54] N. Kiesel, F. Blaser, U. Delić, D. Grass, R. Kaltenbaek, and M. Aspelmeyer. Cavity cooling of an optically levitated submicron particle. *Proceedings of the National Academy of Sciences*, **110**(35):14180–14185, 2013. , cit. on p. ↑4

[55] S. Knünz, M. Herrmann, V. Batteiger, G. Saathoff, T. W. Hänsch, K. Vahala, and Th. Udem. Injection locking of a trapped-ion phonon laser. *Physical Review Letters*, **105**:013004, Jul 2010. , cit. on p. ↑92

[56] I. Kovacic and M. J. Brennan. *The Duffing equation: nonlinear oscillators and their behaviour*. John Wiley & Sons, 2011. , cit. on p. ↑25

[57] H. A. Kramers. Brownian motion in a field of force and the diffusion model of chemical reactions. *Physica*, 1940. , cit. on p. ↑5

[58] H.H. Ku. Notes on the use of propagation of error formulas. *Journal of Research of the National Bureau of Standards. Sec. C: Eng. Inst.*, 1966. , cit. on p. ↑67

[59] S. Li, Q. Wan, Z. Qin, Y. Fu, and Y. Gu. Unraveling the mystery of stöber silica's microporosity. *Langmuir*, **32**(36):9180–9187, 09 2016. , cit. on p. ↑53, ↑74

[60] T. Li, S. Kheifets, D. Medellin, and M. G. Raizen. Measurement of the instantaneous velocity of a brownian particle. *Science*, **328**(5986):1673–1675, 2010. , cit. on p. ↑3

[61] T. Li, S. Kheifets, and M. G. Raizen. Millikelvin cooling of an optically trapped microsphere in vacuum. *Nature Physics*, **7**(7):527–530, mar 2011. , cit. on p. ↑3

[62] R. Lifshitz and M. C. Cross. Nonlinear Dynamics of Nanomechanical and Micromechanical Resonators. *Review of Nonlinear Dynamics and Complexity*, pages 1–215, 2008. , cit. on p. ↑25, ↑26, ↑93

[63] Justin E. M. and Miles J. P. Lights, action: Optical tweezers. *Contemporary Physics*, **43**(4):241–258, 2002. , cit. on p. ↑3

[64] S. Martignoli, F. Gomez, and R. Stoop. Pitch sensation involves stochastic resonance. *Scientific Reports*, **3**:2676 EP –, Sep 2013. , cit. on p. ↑113

[65] I. A. Martínez, É. Roldán, J. M. R. Parrondo, and D. Petrov. Effective heating to several thousand kelvins of an optically trapped sphere in a liquid. *Physical Review E*, **87**:032159, Mar 2013. , cit. on p. ↑96

[66] M. D. McDonnell and D. Abbott. What is stochastic resonance? Definitions, misconceptions, debates, and its relevance to biology. *PLoS Computational Biology*, **5**(5), 2009. , cit. on p. ↑107

[67] M. D. McDonnell and L. M. Ward. The benefits of noise in neural systems: bridging theory and experiment. *Nature Reviews Neuroscience*, **12**(7):415–426, Jul 2011. , cit. on p. ↑113

[68] P. Mestres, I. A. Martinez, A. Ortiz-Ambriz, R. A. Rica, and E. Roldan. Realization of nonequilibrium thermodynamic processes using external colored noise. *Physical Review E*, **90**:032116, Sep 2014. , cit. on p. ↑94, ↑96

[69] J. Millen, T. Deesuwan, P. F. Barker, and J. Anders. Nanoscale temperature measurements using non-equilibrium Brownian dynamics of a levitated nanosphere. *Nature Nanotechnology*, **9**(6):425–9, 2014. , cit. on p. ↑66

[70] J. Millen, P. Z. G. Fonseca, T. Mavrogordatos, T. S. Monteiro, and P. F. Barker. Cavity cooling a single charged levitated nanosphere. *Physical Review Letters*, **114**(12):1–5, 2015. , cit. on p. ↑4

[71] J. R. Moffitt, Y. R. Chemla, S. B. Smith, and C. Bustamante. Recent Advances in Optical Tweezers. *Annual Review of Biochemistry*, 2008. , cit. on p. ↑3

[72] F. Monteiro, S. Ghosh, A. G. Fine, and D. C. Moore. Optical levitation of 10-ng spheres with nano- g acceleration sensitivity. *Physical Review A*, 2017. , cit. on p. ↑5

[73] D. C. Moore, A. D. Rider, and G. Gratta. Search for millicharged particles using optically levitated microspheres. *Physical Review Letters*, **113**(25):1–5, 2014. , cit. on p. ↑5

[74] J. Moser, A. Eichler, J. Güttinger, M. I. Dykman, and A. Bachtold. Nanotube mechanical resonators with quality factors of up to 5 million. *Nature Nanotechnology*, **9**(12):1007, 2014. , cit. on p. ↑1

[75] J. Moser, J. Güttinger, A. Eichler, M. J. Esplandiu, D. E. Liu, M. I. Dykman, and A. Bachtold. Ultrasensitive force detection with a nanotube mechanical resonator. *Nature Nanotechnology*, **8**:493 EP –, Jun 2013. , cit. on p. ↑52

[76] C. J. Myers, M. Celebrano, and M. Krishnan. Information storage and retrieval in a single levitating colloidal particle. *Nature Nanotechnology*, **10**(10):886–891, 2015. , cit. on p. ↑88

[77] R. A. Norte, J. P. Moura, and S. Gröblacher. Mechanical resonators for quantum optomechanics experiments at room temperature. *Physical Review Letters*, **116**:147202, Apr 2016. , cit. on p. ↑2, ↑3

[78] L. Novotny and B. Hecht. *Principles of Nano-Optics*. Cambridge University Press, 2006. , cit. on p. ↑11, ↑14, ↑16

[79] A. D. O'Connell, M. Ansmann, R. C. Bialczak, M. Lenander, E. Lucero, M. Neeley, D. Sank, H. Wang, M. Weides, J. Wenner, J. M. Martinis, A. N. Cleland, and M. Hofheinz. Quantum ground state and single-phonon control of a mechanical resonator. *Nature*, **464**(7289):697–703, Apr 2010. , cit. on p. ↑2

[80] L. Papariello, O. Zilberberg, A. Eichler, and R. Chitra. Ultrasensitive hysteretic force sensing with parametric nonlinear oscillators. *Physical Review E*, **94**(2):022201, 2016. , cit. on p. ↑88, ↑115

[81] S. R. Parnell, A. L. Washington, A. J. Parnell, A. Walsh, R. M. Dalgliesh, F. Li, W. A. Hamilton, S. Prevost, J. P. A. Fairclough, and R. Pynn. Porosity of silica stöber particles determined by spin-echo small angle neutron scattering. *Soft Matter*, **12**(21):4709–4714, 2016. , cit. on p. ↑53, ↑74, ↑80, ↑81

[82] D. Petracchi. What is the role of stochastic resonance? *Chaos, Solitons and Fractals*, **11**:1827–1834, 2000. , cit. on p. ↑107, ↑113

[83] M. Poot and H. S. J. van der Zant. Mechanical systems in the quantum regime. *Physics Reports*, **511**(5):273–335, 2012. , cit. on p. ↑1, ↑2

[84] J. Prat-Camps, C. Teo, C. C. Rusconi, W. Wieczorek, and O. Romero-Isart. Ultrasensitive Inertial and Force Sensors with Diamagnetically Levitated Magnets. *Physical Review Applied*, 2017. , cit. on p. ↑4

[85] G. Ranjit, D. P. Atherton, J. H. Stutz, M. Cunningham, and A. A. Geraci. Attonewton force detection using microspheres in a dual-beam optical trap in high vacuum. *Physical Review A*, 2015. , cit. on p. ↑4, ↑5, ↑110

[86] G. Ranjit, M. Cunningham, K. Casey, and A. A. Geraci. Zeptonewton force sensing with nanospheres in an optical lattice. *Physical Review A*, **93**:053801, May 2016. , cit. on p. ↑5

[87] C. Reinhardt, T. Müller, A. Bourassa, and J. C Sankey. Ultralow-noise sin trampoline resonators for sensing and optomechanics. *Physical Review X*, **6**(2):021001, 2016. , cit. on p. ↑1, ↑3

[88] F. Ricci, R. A. Rica, M. Spasenovic, J. Gieseler, L. Rondin, L. Novotny, and R. Quidant. Optically levitated nanoparticle as a model system for stochastic bistable dynamics. *Nature Communications*, **8**:15141 EP –, May 2017. , cit. on p. ↑65

[89] B. Richards and E. Wolf. Electromagnetic diffraction in optical systems, ii. structure of the image field in an aplanatic system. *Proceedings of the Royal Society of London. Series A. Mathematical and Physical Sciences*, **253**(1274):358, 12 1959. , cit. on p. ↑14

[90] R. Riedinger, S. Hong, R. A. Norte, J. A. Slater, J. Shang, A. G. Krause, V. Anant, M. Aspelmeyer, and S. Gröblacher. Non-classical correlations between single photons and phonons from a mechanical oscillator. *Nature*, **530**:313 EP –, 01 2016. , cit. on p. ↑2

[91] Oriol Romero-Isart. Quantum superposition of massive objects and collapse models. *Physical Review A*, **84**:052121, Nov 2011. , cit. on p. ↑114

[92] Oriol Romero-Isart, Mathieu L Juan, Romain Quidant, and J Ignacio Cirac. Toward quantum superposition of living organisms. *New Journal of Physics*, **12**(3):033015, 2010. , cit. on p. ↑114

[93] L. Rondin, J. Gieseler, F. Ricci, R. Quidant, C. Dellago, and L. Novotny. Direct measurement of kramers turnover with a levitated nanoparticle. *Nature Nanotechnology*, **12**:1130 EP –, Oct 2017. , cit. on p. ↑5, ↑99

[94] D. Rugar, R. Budakian, H. J. Mamin, and B. W. Chui. Single spin detection by magnetic resonance force microscopy. *Nature*, **430**:329–332, 2004. , cit. on p. ↑2

[95] M. Sansa, E. Sage, E. C. Bullard, M. Gély, T. Alava, E. Colinet, A. K. Naik, L. G. Villanueva, L. Duraffourg, M. L. Roukes, G. Jourdan, and S. Hentz. Frequency fluctuations in silicon nanoresonators. *Nature Nanotechnology*, **11**(6):552–558, 2016. , cit. on p. ↑114

[96] E. Schrödinger. Die gegenwärtige situation in der quantenmechanik. *Naturwissenschaften*, **23**(49):823–828, 1935. , cit. on p. ↑2

[97] U. Seifert. Stochastic thermodynamics, fluctuation theorems and molecular machines. *Reports on progress in physics*, **75**(12):126001, 2012. , cit. on p. ↑5

[98] I. Siddiqi, R. Vijay, F. Pierre, C. M. Wilson, M. Metcalfe, C. Rigetti, L. Frunzio, and M. H. Devoret. RF-Driven Josephson Bifurcation Amplifier for Quantum Measurement. *Physical Review Letters*, **93**(November):207002, 2004. , cit. on p. ↑88

[99] D. S. A. Simakov and J. Pérez-Mercader. Noise induced oscillations and coherence resonance in a generic model of the nonisothermal chemical oscillator. *Scientific Reports*, **3**:2404 EP –, Aug 2013. , cit. on p. ↑88

[100] V. Singh, O. Shevchuk, Ya. M. Blanter, and G. A. Steele. Negative nonlinear damping of a multilayer graphene mechanical resonator. *Physical Review B*, **93**:245407, Jun 2016. , cit. on p. ↑25

[101] O. Sneh, M. A. Cameron, and S. M George. Adsorption and desorption kinetics of h2o on a fully hydroxylated sio2 surface. *Surface Science*, **364**(1):61–78, 1996. , cit. on p. ↑82, ↑84

[102] G. A. Somorjai and Y. Li. *Introduction to surface chemistry and catalysis*. Number , cit. on p. John Wiley & Sons, 2010. ↑84

[103] K. Stannigel, P. Komar, S. J. M. Habraken, S. D. Bennett, M. D. Lukin, P. Zoller, and P. Rabl. Optomechanical quantum information processing with photons and phonons. *Physical Review Letters*, **109**:013603, Jul 2012. , cit. on p. ↑2

[104] W. StÃűber, A. Fink, and E. Bohn. Controlled growth of monodisperse silica spheres in the micron size range. *Journal of Colloid and Interface Science*, **26**(1):62 – 69, 1968. , cit. on p. ↑74

[105] K Svoboda and S M Block. Biological applications of optical forces. *Annual Review of Biophysics and Biomolecular Structure*, **23**(1):247–285, 1994. , cit. on p. ↑3

[106] J. D. Teufel, T. Donner, Dale Li, J. W. Harlow, M. S. Allman, K. Cicak, A. J. Sirois, J. D. Whittaker, K. W. Lehnert, and R. W. Simmonds. Sideband cooling of micromechanical motion to the quantum ground state. *Nature*, **475**:359 EP –, 07 2011. , cit. on p. ↑2

[107] J. Tougaard. Signal detection theory, detectability and stochastic resonance effects. *Biological Cybernetics*, **87**(2):79–90, 2002. , cit. on p. ↑106

[108] W. J. Venstra, H. J. R. Westra, and H. S. J. Van der Zant. Stochastic switching of cantilever motion. *Nature Communications*, **4**:2624, 2013. , cit. on p. ↑88, ↑100, ↑102, ↑104, ↑112, ↑113

[109] L. G. Villanueva, E. Kenig, R. B. Karabalin, M. H. Matheny, Ron Lifshitz, M. C. Cross, and M. L. Roukes. Surpassing fundamental limits of oscillators using nonlinear resonators. *Physical Review Letters*, **110**(17):1–5, 2013. , cit. on p. ↑88

[110] G. Volpe and J. Wehr. Effective drifts in dynamical systems with multiplicative noise: a review of recent progress. *Reports on Progress in Physics*, **79**(5):053901, 2016. , cit. on p. ↑96

[111] J. Vovrosh, M. Rashid, D. Hempston, J. Bateman, M. Paternostro, and H. Ulbricht. Parametric feedback cooling of levitated optomechanics in a parabolic mirror trap. *Journal of the Optical Society of America B*, **34**(7):1421–1428, Jul 2017. , cit. on p. ↑4

[112] Y. Wang, Q. Zhao, N. Han, L. Bai, J. Li, J. Liu, E. Che, L. Hu, Q. Zhang, T. Jiang, and S. Wang. Mesoporous silica nanoparticles in drug delivery and biomedical applications. *Nanomedicine: Nanotechnology, Biology and Medicine*, **11**(2):313–327, 2015. , cit. on p. ↑81

[113] P. Weber, J. Güttinger, A. Noury, J. Vergara-Cruz, and A. Bachtold. Force sensitivity of multilayer graphene optomechanical devices. *Nature Communications*, **7**:12496, 2016. , cit. on p. ↑1

[114] L. T. Zhuravlev. The surface chemistry of amorphous silica. zhuravlev model. *Colloids and Surfaces A: Physicochemical and Engineering Aspects*, **173**(1):1 – 38, 2000. , cit. on p. ↑53, ↑74, ↑81, ↑82, ↑83